



HAL
open science

Multi-scale modeling and simulation on buckling and wrinkling phenomena

Qun Huang

► **To cite this version:**

Qun Huang. Multi-scale modeling and simulation on buckling and wrinkling phenomena. Materials. Université de Lorraine, 2018. English. NNT : 2018LORR0033 . tel-01810728

HAL Id: tel-01810728

<https://theses.hal.science/tel-01810728>

Submitted on 8 Jun 2018

HAL is a multi-disciplinary open access archive for the deposit and dissemination of scientific research documents, whether they are published or not. The documents may come from teaching and research institutions in France or abroad, or from public or private research centers.

L'archive ouverte pluridisciplinaire **HAL**, est destinée au dépôt et à la diffusion de documents scientifiques de niveau recherche, publiés ou non, émanant des établissements d'enseignement et de recherche français ou étrangers, des laboratoires publics ou privés.



AVERTISSEMENT

Ce document est le fruit d'un long travail approuvé par le jury de soutenance et mis à disposition de l'ensemble de la communauté universitaire élargie.

Il est soumis à la propriété intellectuelle de l'auteur. Ceci implique une obligation de citation et de référencement lors de l'utilisation de ce document.

D'autre part, toute contrefaçon, plagiat, reproduction illicite encourt une poursuite pénale.

Contact : ddoc-theses-contact@univ-lorraine.fr

LIENS

Code de la Propriété Intellectuelle. articles L 122. 4

Code de la Propriété Intellectuelle. articles L 335.2- L 335.10

http://www.cfcopies.com/V2/leg/leg_droi.php

<http://www.culture.gouv.fr/culture/infos-pratiques/droits/protection.htm>



Ecole Doctorale EMMA (Mécanique et énergétique)

Thèse

Présentée et soutenue publiquement pour l'obtention du titre de

DOCTEUR DE L'UNIVERSITE DE LORRAINE

par **Qun HUANG**

Multi-scale modeling and simulation on buckling and wrinkling phenomena

Soutenue le 18 janvier 2018

Membres du jury:

Rapporteurs:	Prof. Corrado Maurini	Université Pierre et Marie Curie, France
	Prof. Philippe Le Grogneq	ENSTA Bretagne, France
Examineurs:	Prof. Marion Martiny	Université de Lorraine, France
	Prof. Farid Abed-Meraim	Arts et Métiers Paris Tech, France
	Dr. Martin Michael Müller	Université de Lorraine, France
	Dr. Gaetano Giunta	Luxembourg Institute of Science and Technology
	Prof. Michel Potier-Ferry	Université de Lorraine, France
	Prof. Heng Hu	Wuhan University, China

Laboratoire d'Étude des Microstructures et de Mécanique des Matériaux
LEM3 UMR CNRS 7239 - Université de Lorraine
7 rue Félix Savart - 57073 Metz Cedex 03 - France

Acknowledgment

This thesis has been written during my position as a joint-supervised doctoral candidate at University of Lorraine and at Wuhan University.

I would like to express my deeply-felt gratitude to my PhD advisors, Prof. Michel POTIER-FERRY and Prof. Heng HU, for their expertise, invaluable advice and continuous support throughout my studies. Their solid theoretical foundation and tireless academic enthusiasm deeply affect me, and I am honored to acknowledge their mentoring along the way. I deeply look forward to continue our collaboration in both research and life.

An appreciation goes to all my colleagues and friends from University of Lorraine, Wuhan University and Luxembourg Institute of Science and Technology, especially Prof. Hamid Zahrouni, Prof. Salim Belouettar, Prof. Ahmed Makradi, Dr. Mohamed EI Hachemi, Dr. Qian Shao, Dr. Yin Liu, Dr. Kun Yu, Dr. Jie Yang, Siyu Cheng, Yanchuan Hui, Wei Huang, Rui Xu, Jian Liu, Shenyang Liang and Zhengze Cui.

I sincerely thank my family! Thanks for your constant support and encouragement that backs me to complete my PhD!

Abstract

The main aim of this thesis is to develop advanced and efficient multi-scale modeling and simulation techniques to study instability phenomena in three common engineering structures, i.e., membrane, film/substrate and sandwich structures, by combining the Technique of Slowly Variable Fourier Coefficients (TSVFC) and the Asymptotic Numerical Method (ANM). Towards this end, based on the Von Karman plate equations, the TSVFC has been firstly used to develop a two-dimensional (2D) Fourier double-scale model for membrane, which has also been implemented into ABAQUS via its subroutine UEL. Then a 2D Fourier model is constructed for film/substrate. Further, making use of deformation features of the film/substrate, a 1D Fourier model is developed by using both the TSVFC and the Carreras Unified Formulation (CUF). Subsequently, based on high-order kinematics belonging to Zig-Zag theory, a 2D Fourier model is deduced for sandwich plates. The governing equations for the above models are discretized by the Finite Element Method, and the resulting nonlinear systems are solved by the efficient and robust nonlinear solver ANM. These models are then adopted to study instabilities in these structures. Results show that the established models could accurately and efficiently simulate various instability phenomena. Besides, it is found that the membrane instability is very sensitive to boundary conditions, and there exists a dimensionless parameter that is almost constant near bifurcation point for various loading cases and geometric parameters, which may be helpful for fast predicting the occurrence of wrinkles.

Keywords: Membrane, Film/substrate, Sandwich, Instability, Buckling, Wrinkling, Fourier series, Asymptotic Numerical Method

Résumé

L'objectif de cette thèse est de développer des techniques de modélisation et de simulation multi-échelle avancées et efficaces pour étudier les phénomènes d'instabilité dans trois structures d'ingénierie courantes: membrane, film/substrat et structures sandwich, en combinant la technique des coefficients de Fourier lentement variables (TSVFC) et la méthode numérique asymptotique (ANM). À cette fin, basée sur les équations de la plaque de Von Karman, la TSVFC a été utilisée pour développer un modèle de Fourier à bidimensionnel (2D) qui a également été implémenté dans ABAQUS via sa sous-routine UEL. Ensuite, un 2D modèle de Fourier est construit pour le film/substrat. En outre, en utilisant leurs caractéristiques de déformation, un 1D modèle de Fourier est développé en utilisant à la fois le TSVFC et le CUF. Par la suite, sur la base d'une cinématique Zig-Zag d'ordre supérieur, un 2D modèle de Fourier est déduit pour une plaque sandwich. Les équations directrices pour les modèles ci-dessus sont discrétisées par la méthode des éléments finis, et les systèmes non linéaires résultants sont résolus par le solveur non linéaire efficace et robuste ANM. Ces modèles sont ensuite adoptés pour étudier les instabilités dans ces structures. Les résultats montrent que les modèles établis peuvent simuler avec précision et efficacité divers phénomènes d'instabilité. En outre, on constate que l'instabilité membranaire est sensible aux conditions aux limites et qu'il existe un paramètre sans dimension presque constant près du point de bifurcation pour différents cas de charge et paramètres géométriques, ce qui peut être utile pour prédire rapidement l'apparition des rides.

Mots clés: Membrane, Film/substrat, Sandwich, Instabilité, Flambage, Rides, Série de Fourier, Méthode numérique asymptotique, Méthode de pontage de domaine

Contents

1	Introduction	1
2	Fourier model for membrane instability	7
2.1	Introduction	8
2.2	Starting plate model	10
2.3	Macroscopic membrane model	11
2.3.1	Membrane strain energy	12
2.3.2	Bending energy	14
2.3.3	Weak form of the macroscopic membrane model	15
2.3.4	Discretization	16
2.3.5	Implementation of the ANM	17
2.4	Numerical results and discussions	20
2.4.1	Rectangular membrane under biaxial load	20
2.4.2	Rectangular membrane under uniaxial load	22
2.5	A dimensionless parameter to govern wrinkling initiation	28
2.6	Implementation of new reduced model in ABAQUS	32
2.7	Conclusions	33
3	2D Fourier model for film/substrate instability	35
3.1	Introduction	36
3.2	Microscopic model	39
3.2.1	Kinematics	39
3.2.2	Geometric equations and constitutive law	40
3.3	Macroscopic model	42
3.3.1	Internal virtual work of the film	44
3.3.2	Internal virtual work of the substrate	46
3.3.3	External work and weak form of the governing equation	48
3.3.4	Finite element discretisation	48
3.4	Numerical results and discussions	50
3.4.1	Validation	51
3.4.2	Convergence and computation cost	52
3.4.3	Discussions on Fourier-based approach and oscillation locking	56
3.5	Conclusion	60

4	1D Fourier model for film/substrate instability	61
4.1	Introduction	62
4.2	Microscopic model	64
4.2.1	Kinematics	64
4.2.2	Geometric equation and constitutive law	67
4.3	Macroscopic model	68
4.3.1	General macroscopic formulation	68
4.3.2	Discretization	79
4.4	Numerical results	81
4.4.1	Validation	81
4.4.2	Mesh convergence	83
4.4.3	Fourier coefficient study	84
4.5	Conclusion	89
5	Fourier model for sandwich instability	95
5.1	Introduction	96
5.2	The microscopical model	99
5.2.1	Kinematics	99
5.2.2	Strain-displacement relation and constitutive laws	102
5.2.3	Weak form of the microscopical model	103
5.2.4	Governing equations of microscopical model	108
5.3	The macroscopical model	108
5.3.1	The general methodology	108
5.3.2	Internal work of the core	110
5.3.3	Internal work of the skins	113
5.3.4	Governing equations of macroscopical model	115
5.4	Discretization	115
5.5	Numerical results	117
5.5.1	Validation and mesh convergence study	118
5.5.2	Antisymmetrical wrinkling	120
5.5.3	Symmetrical wrinkling	123
5.6	Conclusion	128
6	Conclusion and future perspectives	130
	Bibliography	133

Introduction

Instability phenomena are widely observed in engineering (such as aerospace, automotive, smart materials, biomedical, etc.). The occurrence of wrinkles may pose a limit on the performance of materials or structures and is often thought to be avoided. For example, in the rolling process of thin metal sheet (Jacques et al. (2007); Damil and Potier-Ferry (2010)) (as shown in Fig. (1.1)), the compressive stress induced by the strong tensile stress causes the central fold near the bite, while the residual stress produced by the non-uniform plastic strain causes wrinkles in the edge of the thin metal sheet. If the amplitude of the wrinkles is too large, tens of meters of the sheet should be cut and thrown out, which may lead to at least one day off for the production line. When stretching the metal film (see Fig. (1.2)), compressive stresses perpendicular to the stretching direction, caused by the Poisson effect, may also lead to local wrinkles in the film. Similar instability phenomena can also be found in the following structures: the overall buckling and local wrinkling of the sandwich structures (Hu et al. (2009a); Liu et al. (2012)), long-fibre microbuckling phenomena of composite structures (Drapier et al. (2001)), etc.. In recent years, the wrinkles with the periodic nature have found some applications such as functional morphology (Mei et al. (2007)), the measurement of mechanical properties of materials (Stafford et al. (2004); Chung et al. (2011)) and flexible electronic devices design (Kim and Rogers (2008)). For example, the film/substrate system can be obtained by heating the soft substrate, then depositing the nano-film, and cooling the system (Bowden et al. (1998), see Fig. (1.3)). Due to the mismatch in thermal expansion coefficient between the soft substrate and the nano-film, the residual stress produced during the cooling process will cause the micro-bending of the nano-film. By measuring the wavelength of the wrinkles, the elastic modulus of the nano-film can be predicted easily (Stafford et al. (2004)).

No matter hundreds of nanometers for graphene sheet or tens of meters for metal sheet, the wrinkling phenomena have two common characters: 1) the instability pattern is spatially nearly periodic, and 2) often the modal wavelength is very small compared to the membrane size.

Compared to experiments (Wong and Pellegrino (2006a); Wang et al. (2009); Lecieux and Bouzidi (2010); Nayyar et al. (2014)), numerical simulation may be

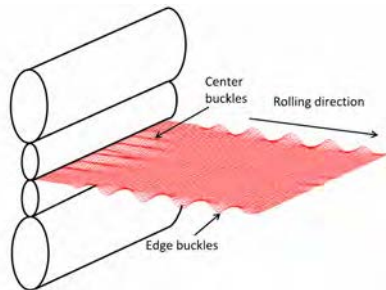


Figure 1.1: Instability in thin metal sheet during cold rolling (Damil and Potier-Ferry (2010))



Figure 1.2: Instability in metal film under uni-axial tension

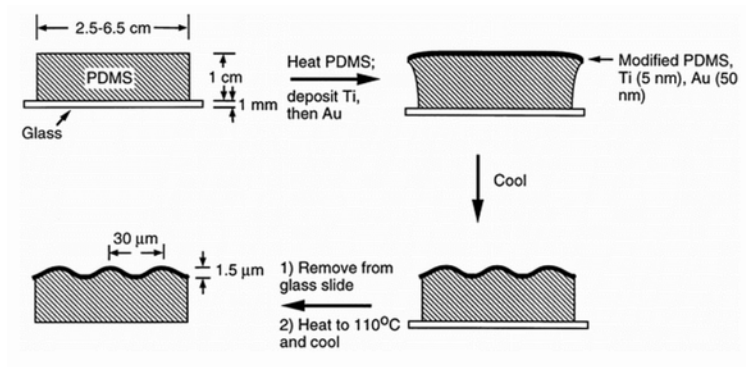


Figure 1.3: Instability in nano-film/substrate system (Bowden et al. (1998))

the best option to predict these instabilities in the view of time and economic cost. For example, to find out and avoid the main causes that lead to wrinkles during the rolling process of thin metal, the nonlinear shell theory (see Wang et al. (2009); Wong and Pellegrino (2006b); Lecieux and Bouzidi (2012); Healey et al. (2013)) could be used, which could accurately describe the details of the thin metal response: size, wavelength, orientation of the wrinkles, instability threshold, etc.. Then by parameter study and analyses that nowadays could be realized with the aid of powerful and stable commercial software, it could be more easier, faster and cheaper than experiments.

However, the traditional numerical strategies have two difficulties: 1) it is difficult to take into account both the computational efficiency and accuracy, and 2) it is difficult to control the nonlinear calculation in cases with a large number of wrinkles and therefore with a large number of equilibrium solutions. Thus, there is a need to develop advanced multi-scale modelling and simulation techniques to accurately predict the wrinkling phenomena in a computationally efficient way. The developed methodology will be extended to the following structures that are widely used in the engineering: (i) wrinkling of thin metal membranes; (ii) buckling and post-buckling phenomena of nano-film/substrate systems; (iii) buckling and wrinkling of sandwiches.

The instability phenomena can be modeled by bifurcation analysis according to the Landau-Ginzburg theory (Wesfreid and Zaleski (1984)). This famous Landau-Ginzburg equation follows from an asymptotic double scale analysis. At the local level one accounts for the periodic nature of the wrinkles, while the slow variations of the envelope are described at the macroscopic scale. Few elements are required to simulate the slow variation of the envelope at the macroscopical scale. However, it has several drawbacks: 1) the solution is not valid far away from the bifurcation, 2) it could not capture the coupling between a global buckling and local wrinkling and 3) the boundary effects are neglected.

A slightly different approach has been proposed recently, where the nearly periodic fields are represented by Fourier series with slowly varying coefficients. This leads to macroscopic models, that are generalized continua, the macroscopic field being defined by Fourier coefficients of the microscopic field (Damil and Potier-Ferry (2006, 2008)). In this sense, the technique is similar to homogenization theory, where a double scale analysis permits to deduce macroscopic generalized continua from microscopic classical ones (Forest and Sab (1998); Kouznetsova et al. (2004)). For example, in order to describe the response of the system which is the sum of a slowly varying mean field and a fluctuation that is nearly periodic in one spatial

direction, at least two slowly varying functions (mean and amplitude) are needed to model the phenomenon.

These above double scale methods are generic and could be applied in all cases of instabilities with spatially periodic pattern. For instance, the asymptotic approach has been used for Rayleigh-Benard convection (Newell and Whitehead (1969); Segel (1969)) and for many fluid instabilities (Wesfreid and Zaleski (1984); Cross and Hohenberg (1993)), for the buckling of a beam on foundation (Amazigo et al. (1970); Pomeau and Zaleski (1981); Potier-Ferry (1983)), for plate buckling (Damil and Potier-Ferry (1986)) and cylindrical shell buckling (Amazigo and Fraser (1971); Abdelmoula et al. (1992)). In the same way, such cellular instabilities appear in the buckling of thin elastic film bound to compliant substrate (Chen and Hutchinson (2004); Wang et al. (2008); Audoly and Boudaoud (2008) which will be studied in this thesis.

The second approach, based on the Fourier series, is also able to account for the coupling between local and global buckling, as in the buckling of stiffened plate (Sridharan and Zeggane (2001)) or of sandwich structures (Hu et al. (2009a); Léo-toing et al. (2002a)) or to account for the influence of wrinkles on the behaviour of membranes (Wang et al. (2009); Nayyar et al. (2014); Wong and Pellegrino (2006c)).

In this thesis, the technique of slowly varying Fourier coefficients will be applied to obtain the so called "macroscopic model" or "reduced model", with the aim to represent the influence of local buckling on the thin walled structures, e.g., thin metal sheet, film/substrate systems and sandwich structures behaviour in a computationally efficient way. Moreover, the macroscopic model allows one to select the wavelength of wrinkles that makes it easier to pilot the nonlinear simulation.

The established nonlinear systems in this thesis will be solved by the Asymptotic Numerical Method (ANM), see Damil and Potier-Ferry (1990). The ANM is an alternative method which falls into the category of numerical perturbation techniques. By introducing the power series expansions into the equilibrium equation, the nonlinear problem is transformed into a sequence of linear problems and solved by the standard finite element method. Many studies (Zahrouni et al. (1999); Cadou et al. (2001); Cochelin et al. (2007)) presented in the literature show that the ANM is more reliable and less time consuming than the iterative classical methods, for instance the modified Newton method and the Newton-Raphson method.

This thesis will be structured as follows, each chapter corresponding to a published research work with a self-consistent notation:

- in Chapter 2: [Int J Solids Struct, 64-65: 246-258 (2015)], the technique of

slowly varying Fourier coefficient is introduced in detail to deduce a macroscopic model for membrane. The model is first implemented in a home-made code, the nonlinear system being solved by the Asymptotic Numerical Method (ANM), which has advantages of efficiency and reliability for stability analyses. It is also implemented as a user element in a commercial software to evaluate the effectiveness of the reduction technique. Various loading cases are considered and the numerical tests show that the macroscopic model can accurately and fast predict the wrinkling patterns. The numerical results highlight the strong influence of a dimensionless parameter for wrinkling

- in Chapter 3: [Thin Wall Struct, 114: 144-153 (2017)], the technique of slowly varying Fourier coefficient is extended for the study of local wrinkling phenomena in thin film/substrate system. The established model, in which the film is modelled by Euler-Bernoulli beam and the substrate by continuum solid model, is demonstrated to be efficient and accurate in predicting the critical load and wrinkling pattern with several numerical examples. Besides, the importance of using the first harmonic of Fourier series in approximating the axial displacement in substrate is, in particular, discussed, and a spurious stiffening effect is pointed out. To overcome this phenomenon, modifications on either the Fourier series or the constitutive equation of the substrate are proposed.
- in Chapter 4: [Compos Struct, 160: 613-624 (2017)], a novel one-dimensional Fourier finite element is proposed for the thin film/substrate structure, in which the substrate is modelled by the Carrera's Unified Formulation (CUF) and the film still by the Euler-Bernoulli beam as in Chapter 3. The numerical results show that the new Fourier model yields accurate results with lower computational cost. Besides, several harmonics of Fourier series are taken into account in this new model, which proves to efficiently trace the wrinkling pattern corresponding to the lowest critical load. The established nonlinear system is solved by the Asymptotic Numerical Method (ANM).
- in Chapter 5: [Comput Method Appl M, 318: 270-295 (2017)], based on the layer-wise kinematic proposed by Yu et al. (2015), a Fourier-based double scale model is developed for the local wrinkling of sandwich plate. Both antisymmetrical and symmetrical wrinkling for sandwich plates under different kinds of loads are investigated and the obtained results demonstrate that the Fourier-based finite element model can accurately yet efficiently predict

wrinkling patterns and critical loads, especially when dealing with wrinkling phenomena with extremely large wavenumbers.

Finally, some conclusions are made by summarizing main outcomes of the proposed theoretical and numerical approaches, and possible future works are also given.

Fourier model for membrane instability

Contents

2.1	Introduction	8
2.2	Starting plate model	10
2.3	Macroscopic membrane model	11
2.3.1	Membrane strain energy	12
2.3.2	Bending energy	14
2.3.3	Weak form of the macroscopic membrane model	15
2.3.4	Discretization	16
2.3.5	Implementation of the ANM	17
2.4	Numerical results and discussions	20
2.4.1	Rectangular membrane under biaxial load	20
2.4.2	Rectangular membrane under uniaxial load	22
2.5	A dimensionless parameter to govern wrinkling initiation	28
2.6	Implementation of new reduced model in ABAQUS	32
2.7	Conclusions	33

Abstract

In this Chapter, the membrane instability phenomena are investigated by a Fourier-related double scale approach that was introduced recently. This leads to a reduced-order model that is able to capture the main features of the wrinkles with few degrees of freedom. This Chapter focuses on the corresponding finite element procedure, its implementation and evaluation and applications to various cases of loading and boundary condition. The finite element model has first been implemented in a home-made code, the nonlinear system being solved by the Asymptotic Numerical Method (ANM), which has advantages of efficiency and reliability for stability analyses. It has also been implemented as a user element in a commercial software to evaluate the effectiveness of the reduction technique. Various loading cases were considered and the numerical tests establish that the reduced model can predict

the wrinkling patterns, even when there are few wrinkles. The numerical results highlight the strong influence of a dimensionless parameter for wrinkling initiation.

Present Chapter corresponds to the published research paper (Huang et al., 2015) [International Journal of Solids and Structures, 64-65: 246-258, 2015.]. A self-consistent notation is adopted.

Keywords: Fourier series, Membrane, Instability, Wrinkling, Asymptotic Numerical Method

2.1 Introduction

Membranes have recently seen a surge of interest in spacecraft structures (sunshields, solar sails, solar panels, reflector antennas and inflatable membranes), civil structures (pneumatic structures for roofs), biomedical materials. Due to the almost negligible bending stiffness and the associated inability to withstand compressive loading, wrinkles arise in very thin membranes, which has an adverse effect on the static and dynamic characteristics and longevity of membrane structures. Hence, to predict and avoid wrinkles, modeling and numerical analysis of membrane wrinkling has been a subject of interest.

The pioneer work on membrane wrinkling belongs to Wagner (1929) who developed a tension field theory, which assumes that out-of-plane flexural and in-plane compressive stress are negligible and bending stiffness is neglected. On the basis of tension field theory, many approaches have been put forward to address issues in membrane wrinkling. In most of them, see Stein and Hedgepeth (1961); Liu et al. (2001); Rossi et al. (2005); Jarasjarungkiat et al. (2008), the stress-strain relationship is modified to eliminate compressive stresses and a wrinkling criterion is established by distinguishing three membrane states: taut, wrinkled and slack. Another method by Roddeman et al. (1987a,b) splits the deformation tensor into two parts, the membrane part and wrinkling part. It has also attracted many researchers, see for instance Miyazaki (2006); Akita et al. (2007); Shaw and Roy (2007); Pimprikar et al. (2010). As the partial differential equations deduced from these membrane models are not elliptic (or hyperbolic in the dynamical case), the presence of slack regions may result in near singular stiffness matrices leading to difficulties in numerical solution. This problem can become well posed if an internal length is included, for instance within Cosserat theory (Pimprikar et al., 2010; Banerjee et al., 2009), but perhaps this regularization is not necessary when us-

ing an explicit dynamic computation. However, all these membrane models just characterize the stress distribution and the wrinkled region, but cannot identify the details of wrinkles such as the amplitude of the wrinkles, their wavelength, the sensitivity to boundary conditions and the instability critical load.

In general, shell elements accounting for very small bending stiffness are preferred to qualitatively characterize the details of membrane wrinkles. In recent papers, Wong and Pellegrino (2006b) presented a general procedure for simulating the onset and growth of wrinkles with shell element using the commercial finite element package ABAQUS and obtained consistent results with experiments in Wong and Pellegrino (2006a,c). Wang et al. (2009) proposed a new Modified Displacement Component (MDC) method to eliminate the singularity of stiffness matrix and apply it to a finite element code ANSYS. Flores and Oñate (2011) used a rotation-free linear strain shell triangle element within explicit time integration strategy that avoids introducing geometric imperfection and initial stress. Lecieux and Bouzidi (2012) adopted the same shell element as Flores to analyze the wrinkling of membranes by direct energy minimization. In all these models, a large number of degrees of freedom are needed to capture the details of wrinkles that results in heavy computational cost and convergence is difficult to achieve. This kind of shell models will be referred as full shell model.

In this Chapter, we present a new finite element based on a reduced-order model established recently from a multiple scale analysis (Damil et al., 2013, 2014). It couples a non-linear 2D membrane model with an envelope equation governing the evolution of wrinkles. This membrane theory is an extension of the Landau-Ginzburg bifurcation equation and it has been deduced by using the method of Fourier series with slowly variable coefficients (Damil and Potier-Ferry, 2010). The origin of the reduction lies in the double scale approach so that the needed spatial meshes can be considered as macroscopic and are not related with the wrinkling wavelength. The finite element technology is described in details and this has been implemented in a home-made code and also in the commercial package ABAQUS as a user element. In the first code, the governing equations are solved by the Asymptotic Numerical Method that is an efficient and robust path following technique in the presence of bifurcations. Several numerical simulations will be discussed in order to evaluate the range of validity of the reduced model, to establish the efficiency of the reduction and to analyze the case of a uniaxially stretched plate (Friedl et al., 2000; Jacques and Potier-Ferry, 2005) that is very sensitive to boundary conditions.

This Chapter is structured as follows. Section 2.2 recalls the famous Föppl-Von Karman equations for isotropic plates that will be considered as the reference

model. In Section 2.3, the finite element procedure will be described. It includes the reduced-order model of Damil et al. (2013, 2014), a 2D finite element discretization and the resolution technique by ANM. In Section 2.4, two numerical examples are investigated to evaluate the range of validity and to bring out the strong influence of boundary conditions on wrinkling. In Section 2.5, a dimensionless parameter K is introduced that is important to predict the appearance of membrane instability. Finally, in Section 2.6, we describe the implementation into ABAQUS as user element (UEL), especially to obtain a reliable evaluation in terms of computation time.

2.2 Starting plate model

In this section, the well known Föppl-Von Karman equations for elastic isotropic plates will be considered as the reference model. Sometimes we also use a commercial code, where the shell finite element model remains valid for large rotations, but the difference between these two models is weak in the cases considered in this Chapter. The Föppl-Von Karman equations can be written as:

$$\left\{ \begin{array}{l} \text{div } \mathbf{N} = 0, \quad (a) \\ \mathbf{N} = \mathbf{L}^m \cdot \boldsymbol{\gamma}, \quad (b) \\ 2\boldsymbol{\gamma} = \nabla \mathbf{u} + {}^t \nabla \mathbf{u} + \nabla w \otimes \nabla w, \quad (c) \\ D\Delta^2 w - \text{div}(\mathbf{N} \cdot \nabla w) = 0. \quad (d) \end{array} \right. \quad (2.1)$$

where $\mathbf{u} = (u, v)$ is the in-plane displacement and w is the out-plane displacement, \mathbf{N} and $\boldsymbol{\gamma}$ are the membrane stress and strain. With the vectorial notations ($\mathbf{N} \rightarrow {}^t \langle N_x \ N_y \ N_{xy} \rangle$, $\boldsymbol{\gamma} \rightarrow {}^t \langle \gamma_x \ \gamma_y \ 2\gamma_{xy} \rangle$), the membrane elasticity tensor is represented by the matrix

$$[\mathbf{L}^m] = \frac{Eh}{1-\nu^2} \begin{bmatrix} 1 & \nu & 0 \\ \nu & 1 & 0 \\ 0 & 0 & \frac{1-\nu}{2} \end{bmatrix}. \quad (2.2)$$

The corresponding internal work \mathcal{W}_{int} can be split into a membrane part \mathcal{W}_m and a bending part \mathcal{W}_b as follows:

$$\begin{cases} \mathcal{W}_{int}(\mathbf{u}, w) = \mathcal{W}_b(w) + \mathcal{W}_m(\mathbf{u}, w), \\ 2\mathcal{W}_b(w) = D \iint_{\omega} \left((\Delta w)^2 - 2(1-\nu) \left(\frac{\partial^2 w}{\partial x^2} \frac{\partial^2 w}{\partial y^2} - \left(\frac{\partial^2 w}{\partial x \partial y} \right)^2 \right) \right) d\omega, \\ 2\mathcal{W}_m(\mathbf{u}, w) = \iint_{\omega} \langle \boldsymbol{\gamma} \rangle [\mathbf{L}^m] \{ \boldsymbol{\gamma} \} d\omega = \frac{Eh}{1-\nu^2} \iint_{\omega} (\gamma_x^2 + \gamma_y^2 + 2(1-\nu)\gamma_{xy}^2 + 2\nu\gamma_x\gamma_y) d\omega. \end{cases} \quad (2.3)$$

2.3 Macroscopic membrane model

In this part, a macroscopic finite element model will be presented that is based on a reduced-order modelling introduced in Damil et al. (2013, 2014). The mathematical model has been deduced from the full shell model by the method of Fourier series with slowly variable coefficients (Damil and Potier-Ferry, 2010). The principle of this Fourier-related approach is to write the unknown field in the following form:

$$\mathbf{U}(x, y) = \sum_{m=-\infty}^{+\infty} \mathbf{U}_m(x, y) e^{miQx}. \quad (2.4)$$

where the wavenumber Q is given and the macroscopic unknown field $\mathbf{U}_m(x, y)$ slowly varies on a period $\left[x, x + \frac{2\pi}{Q} \right]$ of the oscillation. In the case of Föppl-Von Karman equations (2.1), the unknown field is $\mathbf{U}(x, y) = (\mathbf{u}(x, y), w(x, y), \mathbf{N}(x, y), \boldsymbol{\gamma}(x, y))$. Of course, in practice only a finite number of Fourier coefficients will be considered. As pictured in Fig. (2.1), at least two functions $\mathbf{U}_0(x, y)$ and $\mathbf{U}_1(x, y)$ are necessary to describe nearly periodic patterns: $\mathbf{U}_0(x, y)$ can be identified to the mean value while $\mathbf{U}_1(x, y)$ represents the envelope or the amplitude of the spatial oscillations.

In this work, the unknown fields $\mathbf{U}(x, y)$ are expressed only in terms of two harmonics: the mean field $\mathbf{U}_0(x, y)$ and the first order harmonics $\mathbf{U}_1(x, y) e^{iQx}$ and $\overline{\mathbf{U}}_1(x, y) e^{-iQx}$. The mean value $\mathbf{U}_0(x, y)$ is real-valued, while the other envelopes can be complex-valued. So the envelope of the first harmonic $\mathbf{U}_1(x, y)$ can be written as $\mathbf{U}_1(x, y) = \mathbf{r}(x, y) e^{i\varphi(x)}$, where $\mathbf{r}(x, y)$ represents the amplitude modulation and $\varphi(x)$ the phase modulation. If the phase linearly varies ($\varphi(x) = qx + \varphi_0$), this type of approach is able to describe quasi-periodic responses whose wavenumber $Q + q$ slightly differs from the a priori chosen Q . Hence, the method could account

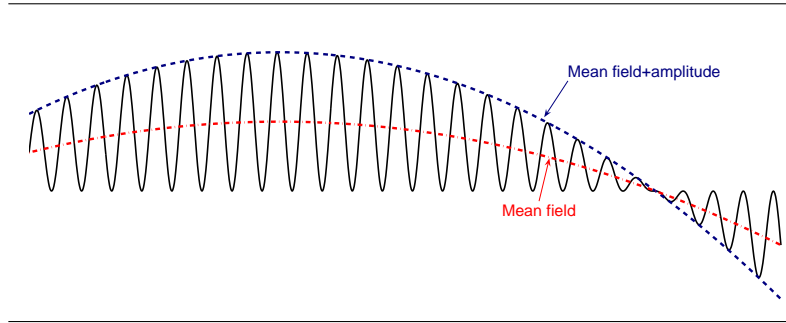


Figure 2.1: At least two macroscopic fields are necessary to describe a nearly periodic response: the mean field and the amplitude of the fluctuation.

for a change of wavenumber.

Here we want to use the simplest consistent model that is able to couple a membrane stress with the variable amplitude of wrinkling pattern. Hence we limit ourselves to real values of the envelope $\mathbf{U}_1(x, y)$. As shown in Mhada et al. (2012), this phase locking can lead to perturbations near the boundary, but an alternative reduced model would be much more expensive. Moreover as in Damil and Potier-Ferry (2010) and Damil et al. (2014), the displacement field is reduced to a wrinkling amplitude, i.e. $u_1 = 0$, $w_0 = 0$. Therefore the macroscopic displacement is reduced to three components $\mathbf{u}_0 = (u_0, v_0)$ and w_1 that can be rewritten for simplicity as $(u, v) \stackrel{def}{=} (u_0, v_0)$, $w \stackrel{def}{=} w_1$. It would be not difficult to keep the mean deflection w_0 as in Liu et al. (2012), what will be necessary to couple local and global buckling.

2.3.1 Membrane strain energy

The derivation rules in Damil and Potier-Ferry (2010) have been extended in this bi-dimensional framework, see Damil et al. (2014). This leads to the following useful formulae (the indices 1 and 0 refer to the number m of the harmonics as in Eq. (2.4)):

$$\{(\nabla w)_1\} = \left\{ \begin{array}{c} \frac{\partial w_1}{\partial x} + iQw_1 \\ \frac{\partial w_1}{\partial y} \end{array} \right\} = \left\{ \begin{array}{c} \frac{\partial w}{\partial x} + iQw \\ \frac{\partial w}{\partial y} \end{array} \right\}, \quad (2.5)$$

and

$$\{\gamma\} \stackrel{def}{=} \{\gamma_0\} = \left\{ \begin{array}{l} \frac{\partial u}{\partial x} + \left(\frac{\partial w}{\partial x}\right)^2 + Q^2 w^2 \\ \frac{\partial v}{\partial y} + \left(\frac{\partial w}{\partial y}\right)^2 \\ \frac{\partial u}{\partial y} + \frac{\partial v}{\partial x} + 2 \frac{\partial w}{\partial x} \frac{\partial w}{\partial y} \end{array} \right\}. \quad (2.6)$$

The membrane strain formula Eq. (2.6) is quite similar to the strain of the initial Von Karman model. It can be split, first into a linear part $\boldsymbol{\varepsilon}(\mathbf{u})$ that is the symmetric part of the displacement gradient and corresponds to the pure membrane strain, second into a nonlinear part $\boldsymbol{\gamma}^{nl}(w)$ that is more or less equivalent to wrinkling deformation in Roddeman et al. (1987a) and is given by

$$\{\boldsymbol{\gamma}^{wr}(w)\} = \left\{ \begin{array}{l} \left(\frac{\partial w}{\partial x}\right)^2 + Q^2 w^2 \\ \left(\frac{\partial w}{\partial y}\right)^2 \\ 2 \frac{\partial w}{\partial x} \frac{\partial w}{\partial y} \end{array} \right\}. \quad (2.7)$$

The main difference with the classical Von Karman strain (2.1-c) is the extension $Q^2 w^2$ in the direction of the wrinkles. If the linear strain is compressive, as wrinkling strain $Q^2 w^2$ is always positive, the wrinkling leads to a decrease of the membrane strain.

One may wonder why derivatives are kept in Eqs. (2.5),(2.6),(2.7). Indeed, the assumption of slowly varying envelopes leads to $\partial/\partial x \ll Q$, $\partial/\partial y \ll Q$. This would lead to pure membrane theory with a nonlinear relation between deflection w and membrane stress \mathbf{N} , but it has been established (Damil et al., 2014) that this could not permit to define the wrinkling wavelength and the wrinkling stress.

By substituting Eq. (2.6) into the third formula of Eq. (2.3), the membrane

strain energy is obtained:

$$2\mathcal{W}_m(\mathbf{u}, w) = \frac{Eh}{1-\nu^2} \iint_{\omega} \left(\begin{aligned} & \left(\frac{\partial u}{\partial x} + \left(\frac{\partial w}{\partial x} \right)^2 + Q^2 w^2 \right)^2 + \left(\frac{\partial v}{\partial y} + \left(\frac{\partial w}{\partial y} \right)^2 \right)^2 \\ & + 2(1-\nu) \left(\frac{1}{2} \left(\frac{\partial u}{\partial y} + \frac{\partial v}{\partial x} \right) + \frac{\partial w}{\partial x} \frac{\partial w}{\partial y} \right)^2 \\ & + 2\nu \left(\frac{\partial u}{\partial x} + \left(\frac{\partial w}{\partial x} \right)^2 + Q^2 w^2 \right) \left(\frac{\partial v}{\partial y} + \left(\frac{\partial w}{\partial y} \right)^2 \right) \end{aligned} \right) d\omega. \quad (2.8)$$

The variation of the membrane energy (2.8) can be written in a concise form:

$$\delta\mathcal{W}_m = \iint_{\omega} \langle \delta\boldsymbol{\gamma} \rangle \{ \mathbf{N} \} d\omega, \quad (2.9)$$

in which,

$$\{ \mathbf{N} \} \stackrel{def}{=} \{ \mathbf{N}_0 \} = [\mathbf{L}^m] \{ \boldsymbol{\gamma} \}. \quad (2.10)$$

2.3.2 Bending energy

The bending energy is calculated in the same framework: $\mathbf{u}_1 = (u_1, v_1) = (0, 0)$, $w_0=0$ and w_1 is real. The computation of the energy can be simplified by keeping only the 0th order in bending energy. Here the derivation process of bending energy is not further described here, more details could be seen in Damil et al. (2014). So the bending energy could be expressed as:

$$\mathcal{W}_b(w) = D \iint_{\omega} \left\{ Q^4 w^2 - 2Q^2 w \Delta w + 4Q^2 \left(\frac{\partial w}{\partial x} \right)^2 + 2(1-\nu)Q^2 \left[w \frac{\partial^2 w}{\partial y^2} + \left(\frac{\partial w}{\partial y} \right)^2 \right] \right\} d\omega. \quad (2.11)$$

Hence,

$$\delta\mathcal{W}_b = \iint_{\omega} \langle \delta\boldsymbol{\beta} \rangle \{ \mathbf{M} \} d\omega, \quad (2.12)$$

in which

$$\{ \boldsymbol{\beta} \} = {}^t \langle w \frac{\partial w}{\partial x} \frac{\partial w}{\partial y} \rangle, \quad (2.13)$$

$$\{ \mathbf{M} \} = [\mathbf{L}^f] \{ \boldsymbol{\beta} \}, \quad [\mathbf{L}^f] = 2D \begin{bmatrix} Q^4 & 0 & 0 \\ 0 & 6Q^2 & 0 \\ 0 & 0 & 2Q^2 \end{bmatrix}. \quad (2.14)$$

Partial differential equations are easily deduced from the reduced elastic energies

(2.8),(2.11) and few analytical solutions are available (Damil et al., 2014). In this Chapter, we focus on the numerical aspects.

2.3.3 Weak form of the macroscopic membrane model

The macroscopic membrane model is deduced from the principle of virtual work

$$\delta \mathcal{W}_{int} = \delta \mathcal{W}_{ext}, \quad (2.15)$$

where $\delta \mathcal{W}_{int}$ and $\delta \mathcal{W}_{ext}$ are the internal and external virtual work. In this Chapter, as the body forces are neglected, $\delta \mathcal{W}_{ext}$ could be expressed in the following form:

$$\delta \mathcal{W}_{ext} = \lambda \int_{S_\sigma} \{ \langle \delta \mathbf{u} \rangle \{ \mathbf{F}_m \} + \delta w F_b \} dS, \quad (2.16)$$

where $\delta \mathbf{u}$ and δw are virtual in-plane and out-plane displacements, $\{ \mathbf{F}_m \}$ and F_b denote respectively the in-plane and out-plane external forces, and λ is a "load parameter". Hence, Eq. (2.15) is transformed into

$$\iint_{\omega} \{ \langle \delta \gamma \rangle [\mathbf{L}^m] \{ \gamma \} + \langle \delta \beta \rangle [\mathbf{L}^f] \{ \beta \} \} d\omega = \lambda \int_{S_\sigma} \{ \langle \delta \mathbf{u} \rangle \{ \mathbf{F}_m \} + \delta w F_b \} dS. \quad (2.17)$$

The unknowns in Eq. (2.17) can be noted by the following vector:

$$\{ \boldsymbol{\theta} \} = {}^t \left\langle \frac{\partial u}{\partial x} \frac{\partial u}{\partial y} \frac{\partial v}{\partial x} \frac{\partial v}{\partial y} w \frac{\partial w}{\partial x} \frac{\partial w}{\partial y} \right\rangle. \quad (2.18)$$

By using this definition, the strain vector $\{ \gamma \}$ could be written in the following form:

$$\{ \gamma \} = \left([\mathbf{H}] + \frac{1}{2} [\mathbf{A}(\boldsymbol{\theta})] \right) \{ \boldsymbol{\theta} \}, \quad (2.19)$$

where

$$[\mathbf{H}] = \begin{bmatrix} 1 & 0 & 0 & 0 & 0 & 0 & 0 \\ 0 & 0 & 0 & 1 & 0 & 0 & 0 \\ 0 & 1 & 1 & 0 & 0 & 0 & 0 \end{bmatrix}, \quad (2.20)$$

$$[\mathbf{A}(\boldsymbol{\theta})] = 2 \begin{bmatrix} 0 & 0 & 0 & 0 & Q^2 w & \frac{\partial w}{\partial x} & 0 \\ 0 & 0 & 0 & 0 & 0 & 0 & \frac{\partial w}{\partial y} \\ 0 & 0 & 0 & 0 & 0 & \frac{\partial w}{\partial y} & \frac{\partial w}{\partial x} \end{bmatrix}. \quad (2.21)$$

Hence, the stress vector $\{\mathbf{N}\}$ reads:

$$\{\mathbf{N}\} = [\mathbf{L}^m] \left([\mathbf{H}] + \frac{1}{2}[\mathbf{A}(\boldsymbol{\theta})] \right) \{\boldsymbol{\theta}\}. \quad (2.22)$$

To unify the unknowns, we define a transform matrix $[\mathbf{T}_\beta]$ that establishes the relation between $\{\boldsymbol{\theta}\}$ and $\{\boldsymbol{\beta}\}$:

$$\{\boldsymbol{\beta}\} = [\mathbf{T}_\beta]\{\boldsymbol{\theta}\}, \quad (2.23)$$

where

$$[\mathbf{T}_\beta] = \begin{bmatrix} 0 & 0 & 0 & 0 & 1 & 0 & 0 \\ 0 & 0 & 0 & 0 & 0 & 1 & 0 \\ 0 & 0 & 0 & 0 & 0 & 0 & 1 \end{bmatrix}. \quad (2.24)$$

Finally, the governing equation of the macroscopic membrane model Eq. (2.17) is in the following form:

$$\iint_{\omega} \langle \delta \boldsymbol{\theta} \rangle \left\{ ({}^t[\mathbf{H}] + {}^t[\mathbf{A}(\boldsymbol{\theta})]) \{\mathbf{N}\} + {}^t[\mathbf{T}_\beta][\mathbf{L}^f][\mathbf{T}_\beta] \{\boldsymbol{\theta}\} \right\} d\omega = \lambda \int_{S_\sigma} \{ \langle \delta \mathbf{u} \rangle \{\mathbf{F}_m\} + \delta w \mathbf{F}_b \} dS. \quad (2.25)$$

In this Section, this macroscopic membrane model would be referenced as "new reduced model".

2.3.4 Discretization

The 2D-Q8 plate finite element, defined by eight nodes and three degrees of freedom per node (u , v and w), is used. The nodal displacement of this 2D element is described by using the classical serendipity shape functions:

$$\begin{cases} u = \langle \mathbf{N}_u \rangle \{\mathbf{q}\}^e = \langle N_1 \ 0 \ 0 \ \dots \ N_8 \ 0 \ 0 \rangle \{\mathbf{q}\}^e, \\ v = \langle \mathbf{N}_v \rangle \{\mathbf{q}\}^e = \langle 0 \ N_1 \ 0 \ \dots \ 0 \ N_8 \ 0 \rangle \{\mathbf{q}\}^e, \\ w = \langle \mathbf{N}_w \rangle \{\mathbf{q}\}^e = \langle 0 \ 0 \ N_1 \ \dots \ 0 \ 0 \ N_8 \rangle \{\mathbf{q}\}^e, \end{cases} \quad (2.26)$$

where $\{\mathbf{q}\}^e$ are the nodal unknowns per element and N_i are the shape functions. Therefore the elementary unknown vector $\{\boldsymbol{\theta}\}^e$ is in the following form:

$$\{\boldsymbol{\theta}\}^e = [\mathbf{G}]\{\mathbf{q}\}^e, \quad (2.27)$$

where

$$[\mathbf{G}] = \begin{bmatrix} \mathbf{N}_{\mathbf{u},x} & 0 & 0 \\ \mathbf{N}_{\mathbf{u},y} & 0 & 0 \\ 0 & \mathbf{N}_{\mathbf{v},x} & 0 \\ 0 & \mathbf{N}_{\mathbf{v},y} & 0 \\ 0 & 0 & \mathbf{N}_{\mathbf{w}} \\ 0 & 0 & \mathbf{N}_{\mathbf{w},x} \\ 0 & 0 & \mathbf{N}_{\mathbf{w},y} \end{bmatrix}. \quad (2.28)$$

Using this discretization, the elementary virtual internal work could be expressed in the following semi-discretized form:

$$\delta \mathcal{W}_{int}^e = \langle \delta \mathbf{q} \rangle^e \iint_{\omega_e} {}^t[\mathbf{G}] ({}^t[\mathbf{H}] + {}^t[\mathbf{A}(\boldsymbol{\theta}(\mathbf{q}))]) \{\mathbf{N}\} + {}^t[\mathbf{G}] {}^t[\mathbf{T}_\beta][\mathbf{L}^f][\mathbf{T}_\beta][\mathbf{G}] \{\mathbf{q}\}^e d\omega. \quad (2.29)$$

We define

$$[\mathbf{B}(\mathbf{q})] = [\mathbf{H} + \mathbf{A}(\boldsymbol{\theta}(\mathbf{q}))][\mathbf{G}], \quad (2.30)$$

$$[\mathbf{B}_l] = [\mathbf{H}][\mathbf{G}], \quad [\mathbf{B}_{nl}(\mathbf{q})] = [\mathbf{A}(\boldsymbol{\theta}(\mathbf{q}))][\mathbf{G}]. \quad (2.31)$$

and

$$\delta \mathcal{W}_{ext}^e = \lambda \sum_e \langle \delta \mathbf{q} \rangle^e \{\mathbf{f}\}^e, \quad (2.32)$$

$$\{\mathbf{f}\}^e = \int_{S_\sigma} {}^t[\mathbf{N}]\{\mathbf{F}\} dS. \quad (2.33)$$

where $[\mathbf{N}]$ is the shape function matrix, $\{\mathbf{F}\}$ is the applied external force.

Finally, the discretization form of the governing equation for macroscopic model is expressed by

$$\sum_e \langle \delta \mathbf{q} \rangle^e \iint_{\omega_e} \left\{ {}^t[\mathbf{B}(\mathbf{q})] \{\mathbf{N}\} + {}^t[\mathbf{G}] {}^t[\mathbf{T}_\beta][\mathbf{L}^f][\mathbf{T}_\beta][\mathbf{G}] \{\mathbf{q}\}^e \right\} d\omega = \lambda \sum_e \langle \delta \mathbf{q} \rangle^e \{\mathbf{f}\}^e, \quad (2.34)$$

and

$$\{\mathbf{N}\} = [\mathbf{L}^m] \left([\mathbf{B}_l] + \frac{1}{2}[\mathbf{B}_{nl}(\mathbf{q})] \right) \{\mathbf{q}\}^e. \quad (2.35)$$

2.3.5 Implementation of the ANM

The above non-linear equations are solved by Asymptotic Numerical Method (ANM) (see Cochelin et al. (2007, 1994)). The solution at the end of j^{th} step, $(\mathbf{q}^j, \mathbf{N}^j, \lambda^j)$ is assumed to be known so as to determine the solution at the end of $(j+1)^{th}$ step, $(\mathbf{q}^{j+1}, \mathbf{N}^{j+1}, \lambda^{j+1})$. Following the perturbation technique, an approached solution

path, in the step $j + 1$, is represented by truncated power series at order N_{order} :

$$\mathbf{N}^{j+1} = \mathbf{N}^j + \sum_{k=1}^{N_{order}} a^k \mathbf{N}_k = \mathbf{N}^j + a\mathbf{N}_1 + a^2\mathbf{N}_2 + \dots, \quad (2.36)$$

$$\mathbf{q}^{j+1} = \mathbf{q}^j + \sum_{k=1}^{N_{order}} a^k \mathbf{q}_k = \mathbf{q}^j + a\mathbf{q}_1 + a^2\mathbf{q}_2 + \dots, \quad (2.37)$$

$$\lambda^{j+1} = \lambda^j + \sum_{k=1}^{N_{order}} a^k \lambda_k = \lambda^j + a\lambda_1 + a^2\lambda_2 + \dots, \quad (2.38)$$

where a is a path parameter defined as

$$a = \langle \mathbf{Q}_1 \rangle (\{\mathbf{Q}^{j+1}\} - \{\mathbf{Q}^j\}) + \lambda_1 (\lambda^{j+1} - \lambda^j). \quad (2.39)$$

Substituting the approached solution Eqs. (2.36)-(2.39) in the equations Eqs. (2.34), (2.35), results in a linear system of equations at each order k . The algebraic equations for the order 1 and the order k are described as following:

Order 1

$$\left\{ \begin{array}{l} \sum_e \langle \delta \mathbf{q} \rangle^e \iint_{\omega_e} ({}^t[\mathbf{B}(\mathbf{q}^j)]) \{\mathbf{N}_1\} + {}^t[\mathbf{B}_{nl}(\mathbf{q}_1)]\{\mathbf{N}^j\} + {}^t[\mathbf{G}]^t[\mathbf{T}_\beta][\mathbf{L}^f][\mathbf{T}_\beta][\mathbf{G}]\{\mathbf{q}_1\}^e d\omega \\ = \sum_e \langle \delta \mathbf{q} \rangle^e \lambda_1 \{\mathbf{f}\}^e, \\ \{\mathbf{N}_1\} = [\mathbf{L}^m] [\mathbf{B}(\mathbf{q}^j)] \{\mathbf{q}_1\}^e, \\ \langle \mathbf{Q}_1 \rangle \{\mathbf{Q}_1\} + \lambda_1^2 = 1. \end{array} \right. \quad (2.40)$$

The third formula in Eq. (2.40) represents a complementary condition resulting from the definition of the path parameter. The term ${}^t[\mathbf{B}_{nl}(\mathbf{q}_1)]\{\mathbf{N}^j\}$ can be expressed as:

$${}^t[\mathbf{B}_{nl}(\mathbf{q}_1)]\{\mathbf{N}^j\} = {}^t[\mathbf{G}][\hat{\mathbf{N}}^j][\mathbf{G}]\{\mathbf{q}_1\}^e, \quad (2.41)$$

where

$$[\hat{\mathbf{N}}^j] = 2 \begin{bmatrix} 0 & 0 & 0 & 0 & 0 & 0 & 0 \\ 0 & 0 & 0 & 0 & 0 & 0 & 0 \\ 0 & 0 & 0 & 0 & 0 & 0 & 0 \\ 0 & 0 & 0 & 0 & 0 & 0 & 0 \\ 0 & 0 & 0 & 0 & Q^2 N_x^j & 0 & 0 \\ 0 & 0 & 0 & 0 & 0 & N_x^j & N_{xy}^j \\ 0 & 0 & 0 & 0 & 0 & N_{xy}^j & N_y^j \end{bmatrix}. \quad (2.42)$$

The use of the matrix $[\hat{\mathbf{N}}]$ permits to transform the internal work into a bilinear form, and this makes it easy to apply the ANM.

Substituting Eq. (2.41) into Eq. (2.40), we get:

$$\sum_e \langle \delta \mathbf{q} \rangle^e [\mathbf{k}(\mathbf{q}^j)] \{\mathbf{q}_1\}^e = \lambda_1 \sum_e \langle \delta \mathbf{q} \rangle^e \{\mathbf{f}\}^e, \quad (2.43)$$

where $[\mathbf{k}(\mathbf{q}^j)]$ is the elementary stiffness matrix given below:

$$[\mathbf{k}(\mathbf{q}^j)] = \iint_{\omega_e} {}^t[\mathbf{B}(\mathbf{q}^j)][\mathbf{L}^m][\mathbf{B}(\mathbf{q}^j)] + {}^t[\mathbf{G}][\hat{\mathbf{N}}^j][\mathbf{G}] + {}^t[\mathbf{G}]^t[\mathbf{T}_\beta][\mathbf{L}^f][\mathbf{T}_\beta][\mathbf{G}] \, d\omega. \quad (2.44)$$

Suppose that the vectors $\{\mathbf{Q}\}$, $\{\mathbf{F}\}$ are the assembly of $\{\mathbf{q}\}^e$, $\{\mathbf{f}\}^e$. After assembling the elementary stiffness matrix, a linear equation for the global system at order 1 is given below:

$$[\mathbf{K}(\mathbf{Q}^j)]\{\mathbf{Q}_1\} = \lambda_1\{\mathbf{F}\}. \quad (2.45)$$

Order k

$$\left\{ \begin{array}{l} \sum_e \langle \delta \mathbf{q} \rangle^e \iint_{\omega_e} ({}^t[\mathbf{B}(\mathbf{q}^j)]) \{\mathbf{N}_k\} + {}^t[\mathbf{B}_{nl}(\mathbf{q}_k)]\{\mathbf{N}^j\} + {}^t[\mathbf{G}]^t[\mathbf{T}_\beta][\mathbf{L}^f][\mathbf{T}_\beta][\mathbf{G}] \{\mathbf{q}\}^e \, d\omega \\ = \sum_e \langle \delta \mathbf{q} \rangle^e (\lambda_k \{\mathbf{f}\}^e + \{\mathbf{f}_{intk}^{nl}\}^e), \\ \{\mathbf{N}_k\} = [\mathbf{L}^m] [\mathbf{B}(\mathbf{q}^j)] \{\mathbf{q}_k\}^e + \{\mathbf{N}_k^{nl}\}, \\ \langle \mathbf{Q}_1 \rangle \{\mathbf{Q}_k\} + \lambda_1 \lambda_k = 0. \end{array} \right. \quad (2.46)$$

In contrast to first order, there are two right-hand sides at each order $k > 1$ caused by nonlinear terms: the first one, $\{\mathbf{f}_{intk}^{nl}\}^e$ and the second one, $\{\mathbf{N}_k^{nl}\}$. They depend on the displacements and stresses at orders anterior to the order k :

$$\{\mathbf{f}_{intk}^{nl}\}^e = - \sum_{m=1}^{k-1} \iint_{\omega_e} {}^t[\mathbf{B}_{nl}(\mathbf{q}_{k-m})]\{\mathbf{N}_m\} \, d\omega, \quad (2.47)$$

$$\{\mathbf{N}_k^{nl}\} = [\mathbf{L}^m] \sum_{m=1}^{k-1} \frac{1}{2} [\mathbf{B}_{nl}(\mathbf{q}_{k-m})]\{\mathbf{q}_m\}^e. \quad (2.48)$$

Taking into account Eq. (2.41), and applying Eqs. (2.47), (2.48) in Eq. (2.46), we get:

$$\sum_e \langle \delta \mathbf{q} \rangle^e [\mathbf{k}(\mathbf{q}^j)] \{\mathbf{q}_k\}^e = \sum_e \langle \delta \mathbf{q} \rangle^e (\lambda_k \{\mathbf{f}\}^e + \{\mathbf{f}_k^{nl}\}^e), \quad (2.49)$$

where

$$\{\mathbf{f}_k^{nl}\}^e = \{\mathbf{f}_{intk}^{nl}\}^e - \iint_{\omega_e} {}^t [\mathbf{B}(\mathbf{q}^j)] \{\mathbf{N}_k^{nl}\} d\omega. \quad (2.50)$$

After assembling the elementary stiffness matrix, the linear equation for each order k is:

$$[\mathbf{K}(\mathbf{Q}^j)]\{\mathbf{Q}_k\} = \lambda_k \{\mathbf{F}\} + \{\mathbf{F}_k^{nl}\}. \quad (2.51)$$

Here $\{\mathbf{F}_k^{nl}\}$ is the assembly of $\{\mathbf{f}_k^{nl}\}^e$.

Eqs. (2.45) and (2.51) mean that all orders in one step have the same stiffness matrix, that is to say, only one stiffness matrix will be inverted in one step. After the values of $\{\mathbf{Q}_k\}$ are calculated, then the solutions at step $(j+1)$ th can be obtained by:

$$\{\mathbf{Q}^{j+1}\} = \{\mathbf{Q}^j\} + a\{\mathbf{Q}_1\} + a^2\{\mathbf{Q}_2\} + a^3\{\mathbf{Q}_3\} + \dots \quad (2.52)$$

The maximum value of path parameter a is adopted with the same principle as in Cochelin et al. (2007),

$$a = \left(\epsilon \frac{\|\mathbf{Q}_1\|}{\|\mathbf{Q}_k\|} \right) \frac{1}{Norder - 1}, \quad (2.53)$$

where ϵ is a precision parameter, which is determined by the user.

2.4 Numerical results and discussions

The new reduced model will be investigated through two numerical examples: 1) rectangular membrane under biaxial compression-tension load, 2) rectangular membrane under uniaxial tension load. In the first example, there are many wrinkles and this will be an opportunity to check that a macroscopic mesh can describe wrinkles even if the mesh size is larger than the wrinkling wavelength. The second example is a classical case of membrane wrinkling under tensile load (Friedl et al., 2000; Jacques and Potier-Ferry, 2005). In this case, the number of waves is much smaller and the onset of instability is very sensitive to loading and boundary conditions. The results are compared with commercial software ABAQUS to assess advantages and disadvantages of the new reduced model; the shell element S8R5 with reduced integration is adopted in ABAQUS and referred as 'full shell model'.

2.4.1 Rectangular membrane under biaxial load

Fig. (2.2) presents a clamped rectangular membrane under biaxial tension-compression load. A uniform tensile load $N_y = 10 \text{ N/mm}$ is firstly preloaded, then an increas-

ing compressive load λN_x follows. The side lengths L_x and L_y are respectively 1000 mm and 200 mm , the thickness h is 0.05 mm . The material behavior is assumed to be linear isotropic elastic with $E = 70\,000 \text{ MPa}$ and $\nu = 0.3$. The mesh details of each model are as in Table 2.1. The wavenumber Q is chosen with the formula $Q = \sqrt[4]{12\pi^2(1-\nu^2)} \frac{1}{hL_x} \sqrt[4]{\frac{\sigma_y}{E}}$, see Cerda and Mahadevan (2003).

Table 2.1: Mesh details for the rectangular membrane under biaxial load.

	X	Y	Total element	DOF
Full shell model (ABAQUS)	200	20	4000	98646
New reduced model	10	16	160	1599

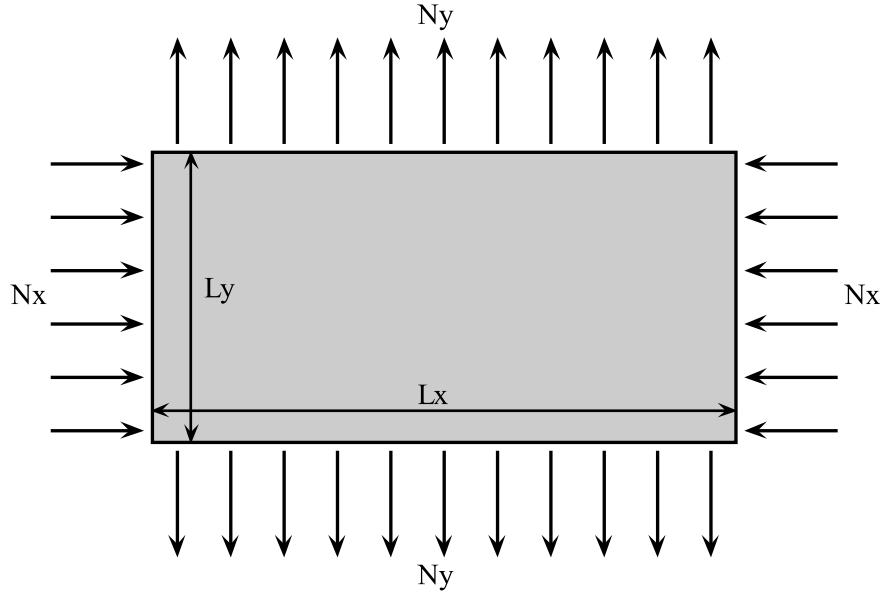


Figure 2.2: Rectangular membrane under biaxial load.

Local wrinkles occur in the membrane when the applied compressive stress increases. Fig. (2.3) presents the wrinkling patterns just after the bifurcation. It appears that the new reduced model can correctly predict the same shape and number of wrinkles as the full shell model does.

A more quantitative analysis is shown in Fig. (2.4). One can obviously conclude that the new reduced model agrees very well with the full shell model near the bifurcation point where the average compressive load is $N_x \approx -0.0900 \text{ N/mm}$. Remember that there are 10 finite elements in the length for about 30 wrinkles. This illustrates that the macroscopic mesh is not related to the size of the wrinkles. The wrinkling amplitude and shape are further studied by plotting the central cross section ($Y = 100 \text{ mm}$). Fig. (2.5) shows that the new reduced model

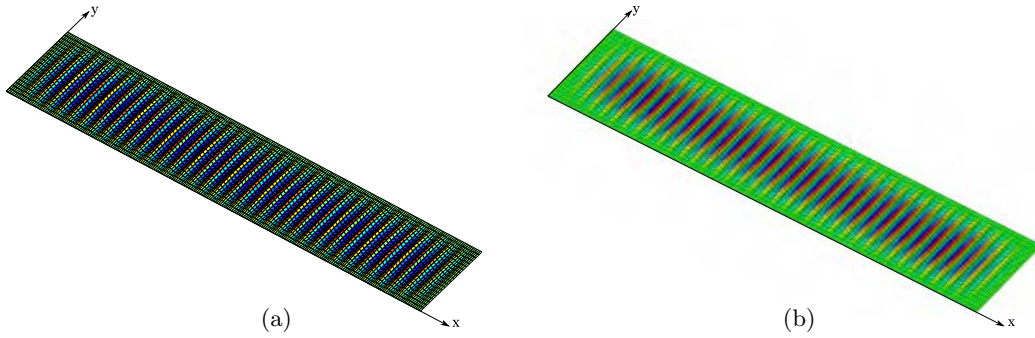


Figure 2.3: Wrinkling patterns near the bifurcation of a rectangular membrane under biaxial load for new reduced model (a), full shell model (b).

could correctly describe the spatial distribution of instability patterns near bifurcation. The envelope of wrinkling in x direction is nearly constant in the bulk of the membrane. With the increasing in compressive load, the amplitude of wrinkling increases rapidly and the envelope turns into a hyperbolic tangent shape as seen in Fig. (2.5). Next the shape of the pattern changes when the load increases as shown in Fig. (2.6). Firstly, the envelop in the center is no longer constant and becomes slightly wavy, secondly the wrinkles localize near the boundary. At this loading level $w/h \approx 0.7$, the reduced model remains qualitatively exact by predicting localization and wavy amplitude, but these predictions are not quantitatively exact, especially the localization that is underestimated. This means that the validity range of the model has been reached, at least in the boundary zone, see Fig. (2.7). There are several ways to improve the reduced model. A simple idea would be to increase the number of harmonics. Another possibility is to go back to a complex envelope w_1 , indeed it has been proved (Mhada et al., 2012) that this improves the prediction of the boundary behavior by taking phase shift into account. A best possible improvement is a bridging technique as in Hu et al. (2011) that permits to go back to the full model in a small region near the boundaries.

2.4.2 Rectangular membrane under uniaxial load

The clamped rectangular membrane is stretched on short edges as shown in Fig. (2.8), the two long edges are completely free. Geometric and material parameters are as following: $L_x = 200 \text{ mm}$, $L_y = 1400 \text{ mm}$, $h = 0.05 \text{ mm}$, $E = 70\,000 \text{ MPa}$, $\nu = 0.3$. The mesh details of each model are as in Table 2.2. The wavenumber Q is chosen from a full shell computation in ABAQUS.

The membrane would be stretched by two kinds of loading approaches: displacement load and stress load. Let us specify the boundary conditions along the

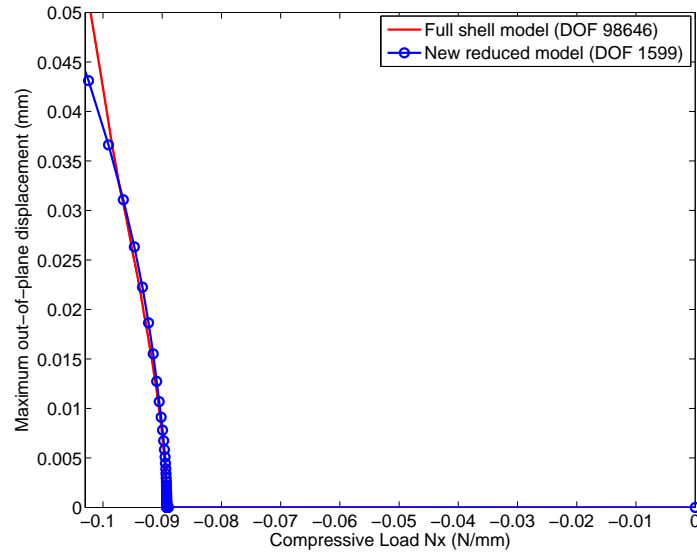


Figure 2.4: Bifurcation path of a rectangular membrane under biaxial load with tensile load $N_y = 10 \text{ N/mm}$.

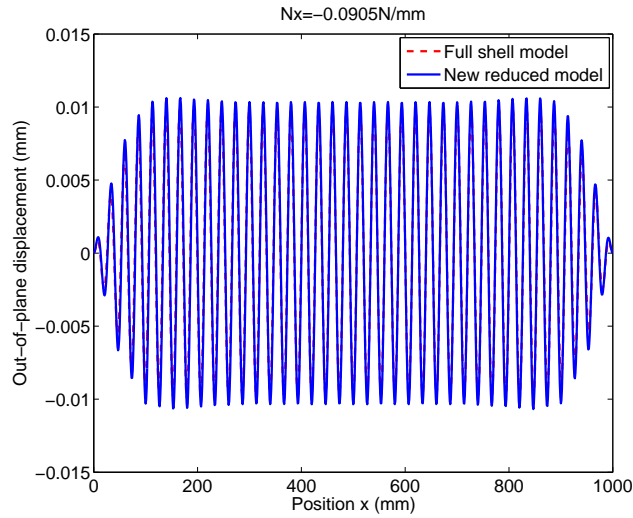


Figure 2.5: Central cross section ($Y=100 \text{ mm}$) of a rectangular membrane under biaxial load near bifurcation point, $N_y = 10 \text{ N/mm}$, $N_x = -0.0905 \text{ N/mm}$.

Table 2.2: Mesh details for rectangular membrane under uniaxial load.

	X	Y	Total element	DOF
Full shell model(ABAQUS)	20	50	1000	24846
New reduced model	8	30	240	2391

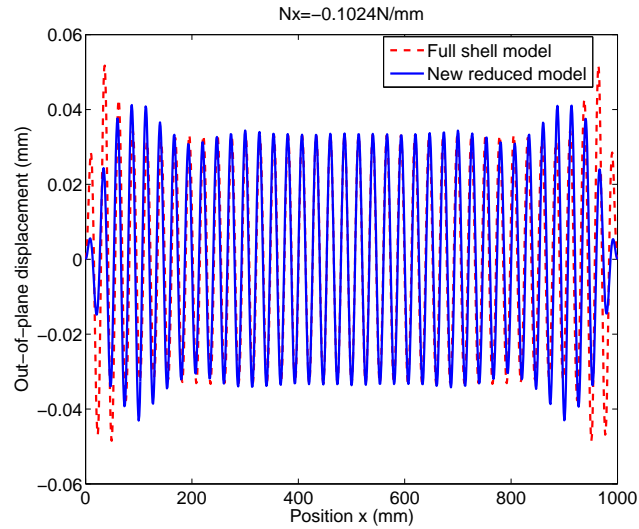


Figure 2.6: Central cross section ($Y=100 \text{ mm}$) of a rectangular membrane under biaxial load further after bifurcation point, $N_y = 10 \text{ N/mm}$, $N_x = -0.1024 \text{ N/mm}$.

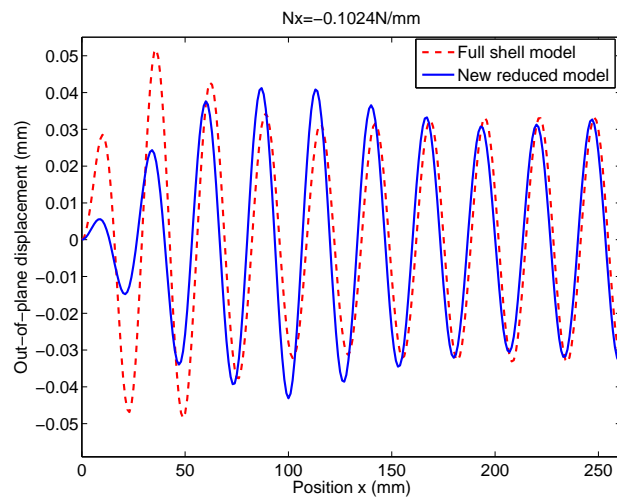


Figure 2.7: Details of the out-of-plane displacement near the boundary in Fig. 2.6.

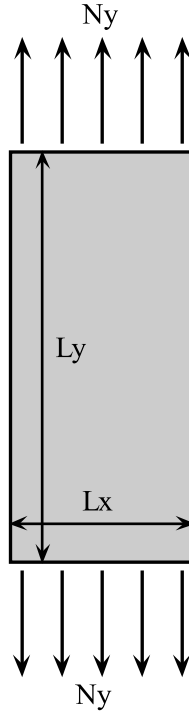


Figure 2.8: Rectangular membrane under uniaxial load.

short sides: the components u , w and $\partial w/\partial x$ are zero in the two cases, a uniform displacement v is prescribed on the side $y = L_y$ in the so-called displacement load while a uniform membrane stress N_y is prescribed in the case of stress load. The origin of wrinkling is a secondary compression N_x located in an area around the line $y = L_x$.

The wrinkling patterns for both loading cases are presented in Fig. (2.9), (2.10), which leads to the same morphology. However, the bifurcation paths of two cases are quite different, see Fig. (2.11). The critical tensile load in displacement load case is about 6 times bigger than that in the stress load case. It can be easily concluded that the membrane instability depends strongly on boundary conditions.

In fact, the instability phenomena of such a membrane are due to Poisson's effects that are localized near the boundary, see Fig. (2.12). These effects strongly depend on the distribution of the main stress. A small difference on the distribution of the main stress along the short edges can cause a big difference on the distribution of the compressive stress, see Fig. (2.12). Let us recall the critical role of the stress ratio $C = \frac{|\sigma_x^{max}|}{\sigma_y}$. As shown in Friedl et al. (2000) and Jacques and Potier-Ferry (2005), the buckling level depends on this dimensionless parameter and the buckling stress decrease when the ratio C increase. Because the ratio C in displacement load

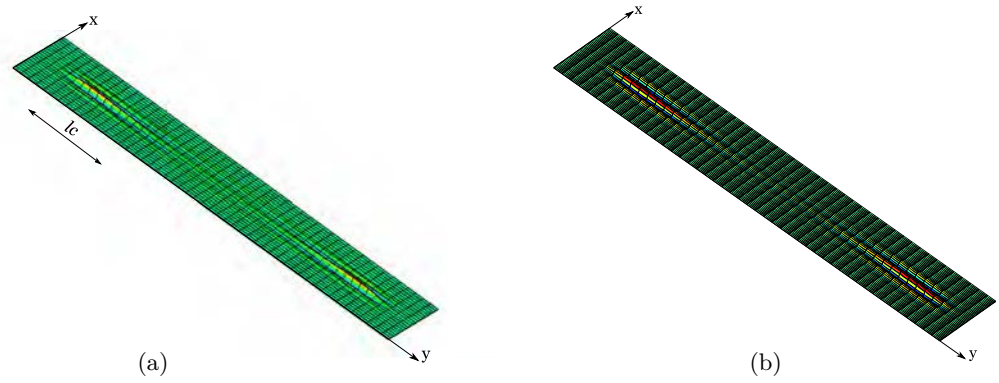


Figure 2.9: Wrinkling patterns near the bifurcation of a rectangular membrane under uniaxial displacement load for full shell model (a) and new reduced model (b), $N_y = 39.2 \text{ N/mm}$.

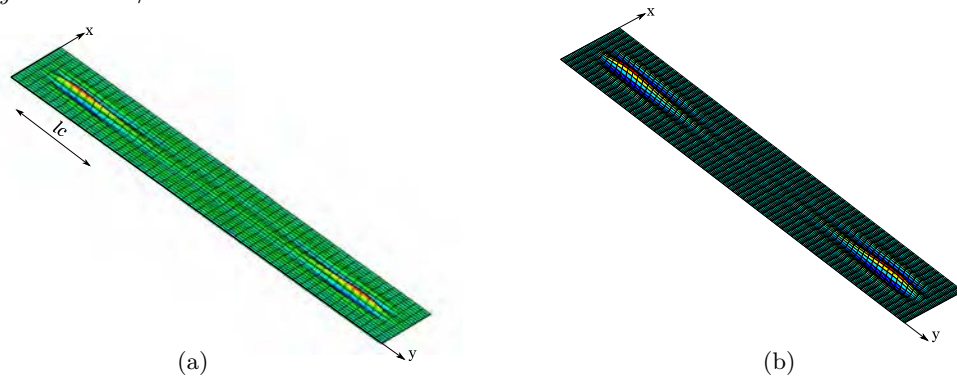


Figure 2.10: Wrinkling patterns near the bifurcation of a rectangular membrane under uniaxial stress load for full shell model (a) and new reduced model (b), $N_y = 6.6 \text{ N/mm}$.

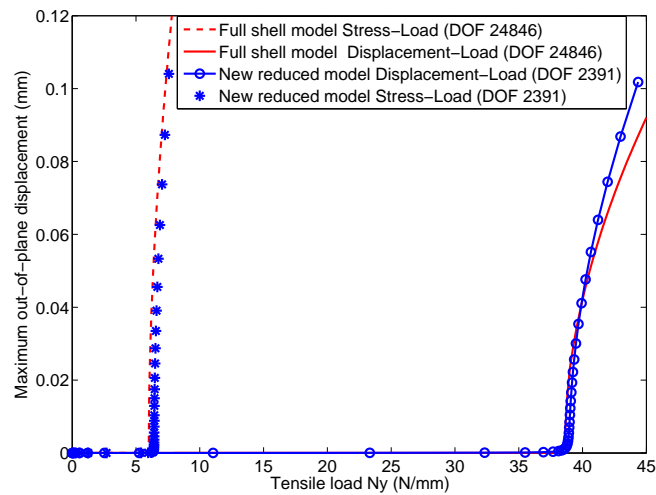


Figure 2.11: Bifurcation path for rectangular membrane under uniaxial load with two different loading cases: uniform displacement load and stress load.

case is smaller than in stress load, see Table. 2.3, the displacement load case turns out to give a bigger critical load. Besides, the stress ratio C has been observed in the whole process of loading. During pre-buckling period, C remains a constant, $|\sigma_x|$ is proportional to σ_y , while after membrane buckling, $|\sigma_x|$ increases rapidly, so C raises rapidly too. Thus membrane instability could be observed through the change of the value of C .

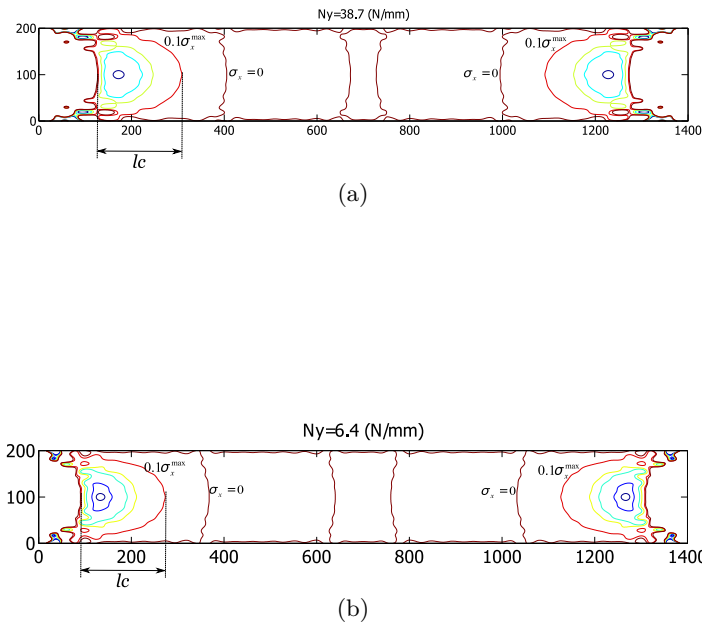


Figure 2.12: Compressive stress distribution near bifurcation with new reduced model for two load cases: (a) displacement load; (b) stress load.

Fig. (2.13) plots the out-of-plane displacement along the cross section in $Y = 168$ mm farther away from bifurcation point. As in previous numerical tests, they are quite similar except slight differences in the wrinkling amplitude and distribution. In fact, one can notice a discrepancy in wavelength and phase as compared with full shell model. As mentioned before, the envelope w_1 is assumed to be real, what provides a constant wavenumber Q through the procedure. Therefore these changes can not be described by the new reduced model.

In conclusion, despite slight differences in boundary conditions, the new reduced model is able to predict accurately and fast the bifurcation point with much less degrees of freedom than full shell model, and correctly describe the post-buckling process.

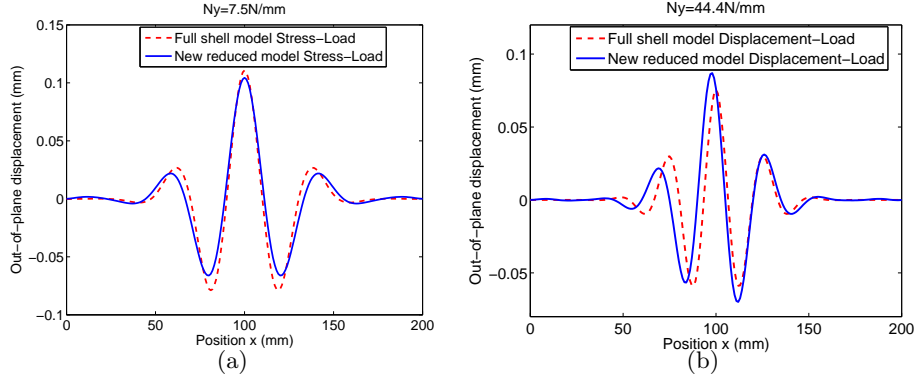


Figure 2.13: Central cross section ($Y=168$ mm) of rectangular membrane under uniaxial stress load (a), displacement load (b).

2.5 A dimensionless parameter to govern wrinkling initiation

Wrinkling is characterised by an instability with a short wavelength in a direction, x in this Chapter, in such a way that the Laplacian Δ can be approximated by $\frac{\partial^2}{\partial x^2}$. Let us come back to the bending equation (2.1-d) of the Föppl-Von Karman model, with a biaxial prestress $\mathbf{N} = h\sigma_x(y)\mathbf{e}_x \otimes \mathbf{e}_x + h\sigma_y\mathbf{e}_y \otimes \mathbf{e}_y$ that is not necessarily constant in the direction of the wrinkles. Thus the Eq. (2.1-d) becomes:

$$D \frac{\partial^4 w}{\partial x^4} + h|\sigma_x(y)| \frac{\partial^2 w}{\partial x^2} - h\sigma_y \frac{\partial^2 w}{\partial y^2} = 0. \quad (2.54)$$

The stress ratio C is a first dimensionless parameter that influences the wrinkling process and that is constant in the pre-buckling phase. Here we shall define another dimensionless parameter from a characteristic length l_c defined as in Jacques and Potier-Ferry (2005) that is related to the size of the compressed area. Thus one can define non-dimensional variables $\bar{x} = xQ$, $\bar{y} = y/l_c$, where the wrinkling wavenumber Q is unknown. This leads to the following eigenvalue problem:

$$DQ^4 \frac{\partial^4 w}{\partial \bar{x}^4} + h|\sigma_x(y)|Q^2 \frac{\partial^2 w}{\partial \bar{x}^2} - \frac{h\sigma_y}{l_c^2} \frac{\partial^2 w}{\partial \bar{y}^2} = 0. \quad (2.55)$$

Classically (Cerda and Mahadevan, 2003) the wrinkling wavelength is obtained by requiring that the first and the third term are of the same order:

$$DQ^4 \sim \frac{h\sigma_y}{l_c^2} \Rightarrow Q^2 \sim \sqrt{\frac{\sigma_y}{E}} \frac{1}{hl_c}, \quad (2.56)$$

so that the critical stress $|\sigma_x^{crit}| \approx 2DQ^2$ can be related to the quantities E , σ_y , h , l_c :

$$|\sigma_x^{crit}| \sim \sqrt{E\sigma_y} \frac{h}{l_c}. \quad (2.57)$$

That is why we discuss here the influence of the non-dimensional loading parameter

$$K = \frac{|\sigma_x|}{\sqrt{E\sigma_y}} \frac{l_c}{h}. \quad (2.58)$$

The definition of the characteristic length l_c can be questionable in the same way as the characteristic length defining the Reynolds number in fluid mechanics. This is quite clear for the clamped membrane under uniform biaxial load studied in Section 2.4.1, in which case there is an analytical solution (Damil et al., 2013) in a double sine shape so that the characteristic length can coincide with the plate width: $l_c = L_y$. Nevertheless even in this simple case, this definition depends on boundary conditions. In the uniaxial tensile cases of Section 2.4.2, the compression σ_x is not uniform and the wrinkling is due to one or two previously mentioned compressive zones, but the most relevant characteristic length is not the size of these compressive zones. Indeed there is a large region where the compressive stress is very small and therefore has little influence on wrinkling. That is why we propose to define l_c by the size of the region where $|\sigma_x|$ is greater than $|\sigma_x^{max}|/10$, see Fig. 2.12. For very short plates, there is only one compressive zone, the characteristic length l_c is also defined as before (Fig. 2.14a). For short plates where the two compressive zones overlap (Fig. 2.14b), we propose to define the characteristic length as the half of this area where $|\sigma_x|$ is greater than $|\sigma_x^{max}|/10$. In fact, this characteristic length can be understood as a longitudinal wrinkling wave length and it is generally unknown. For instance in Jacques and Potier-Ferry (2005), such a length has been defined from a semi-analytical minimization of the bifurcation load. We tried to define it a priori from the shape of the initial stress field, but of course it is difficult to establish a universal rule.

To check the relevance of the new non-dimensional loading parameter K , several full nonlinear shell computations have been performed, for various geometries and for four loading cases: a clamped plate with biaxial load as in Fig. (2.2) and three clamped-free membranes as in Fig. (2.8). These clamped-free membranes correspond to three types of loading: thermal load where a uniform temperature is applied, stress load where a uniform force is applied on the sides $y = 0$, $y = L_y$ as pictured in Fig. (2.8) and a displacement load where a uniform displacement v is applied on the same side. In these three cases, the displacement u is locked along

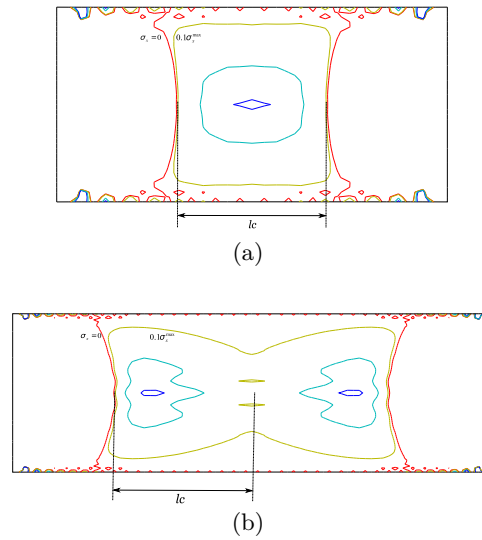


Figure 2.14: Compressive stress distribution near bifurcation with full shell model for rectangular membrane under uniaxial displacement load: (a) 200×400 ; (b) 200×600 .

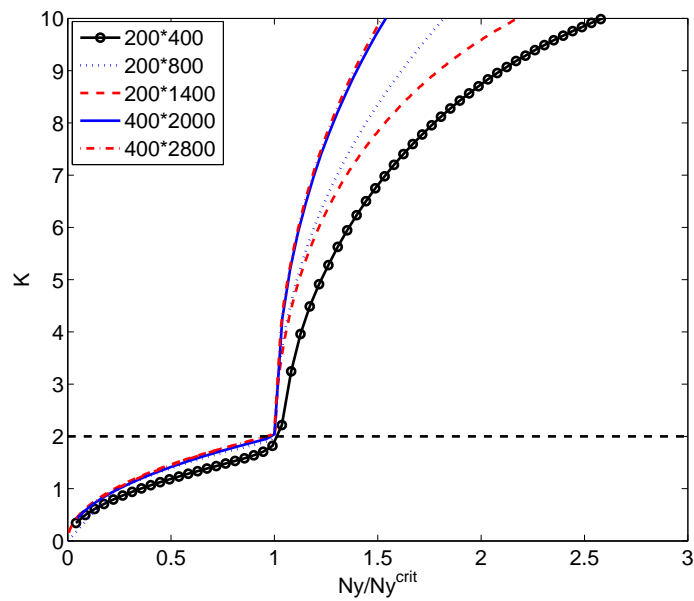


Figure 2.15: The evolution of K in a rectangular membrane under uniaxial displacement load with full shell model.

the sides $y = 0$, $y = L_y$. Note that in these clamped-free cases, the stress $\sigma_x(y)$ is not uniform. The parameter K in Eq. (2.58) is defined by accounting the maximum of this stress.

Full shell finite element results are presented in Table 2.3. In these numerical tests, various critical stresses and various wrinkling wavelenghtes were obtained for various values of the stress ratio C , but the non-dimensional stress K remains about constant near bifurcation, see also Fig. 2.15. This establishes the relevance of this non-dimensional parameter to define the critical wrinkling stress in many loading cases. Thus the following estimate for the wrinkling load $|\sigma_x^{crit}| \approx 2\sqrt{E\sigma_y} \frac{h}{l_c}$ seems valid for a large class of geometries and boundary conditions. It should be noticed that the non-dimensional stress K has about 20% difference in the case of two compressive zones overlapping (Fig. 2.14b), because the definition of the characteristic length is not very clear in this case. Beyond the bifurcation threshold, the applied stress σ_y and the resulting compressive stress $\sigma_x(y)$ increase, which means that the post-wrinkling behavior is stable, but this response does not depend only on K .

Table 2.3: The critical load σ^{crit} , wrinkle wavelength l_x , stress ratio $C = \frac{|\sigma_x^{crit}|}{\sigma_y}$, characteristic length l_c and dimensionless loading parameter $K^{crit} = \frac{|\sigma_x^{crit}| l_c}{\sqrt{E\sigma_y} h}$ for different geometry sizes in rectangular membrane with full shell model. Four cases: thermal-load, stress-load, displacement-load for uniaxial load case, tensile-compressive biaxial load. The results are obtained near the bifurcation.

	$Lx \times Ly$ (mm)	σ^{crit} (N/mm)	l_x (mm)	C (10^{-2})	l_c (mm)	K^{crit}
Thermal-load	200×800	1.65	54.97	2.56	184	2.04
	200×1400	1.91	49.96	2.52	180	2.13
Stress-load	200×800	5.45	44.98	1.41	184	2.05
	200×1400	5.98	39.97	1.44	180	2.14
Displacement-load	200×400	11.48	29.97	1.08	154	1.91
	200×600	20.65	29.95	0.62	172	1.65
	200×800	32.85	29.91	0.57	184	2.02
	200×1400	38.40	29.94	0.54	181	2.03
	400×2000	8.59	49.96	0.57	360	2.05
	400×2800	8.70	49.96	0.56	364	2.03
Biaxial-load	200×200	-0.0903	26.25	0.91	200	1.93
	400×200	-0.0899	26.37	0.91	200	1.93
	600×200	-0.0896	26.97	0.90	200	1.92

2.6 Implementation of new reduced model in ABAQUS

To simplify the simulation procedure and use it for more complicate membrane structures, the new reduced model was implemented in the commercial finite element code ABAQUS as a user element (UEL) subroutine.

In general procedures, ABAQUS uses Newton-Raphson's method as a numerical technique for solving nonlinear equilibrium equations. Path following calculations in the presence of bifurcation require the application of an arc-length technique. We used the so-called 'modified Riks analysis'.

In this algorithm, three quantities have to be defined: the stiffness matrix $[\mathbf{K}]$, the residual force vector $\mathbf{RHS}(1)$ that depends on the right-hand-side force vector $\{\mathbf{F}\}$ and the increment of external load $\mathbf{RHS}(2)$. In the case of mechanical equilibrium of a finite element subject to surface tractions $\{\mathbf{t}\}$ and body forces $\{\mathbf{f}\}$ with stress $[\boldsymbol{\sigma}]$, the \mathbf{RHS} force vector is defined as

$$\{\mathbf{F}\} = \int_S [\mathbf{N}] \cdot \{\mathbf{t}\} dS + \int_V [\mathbf{N}] \cdot \{\mathbf{f}\} dV - \int_V \{\boldsymbol{\beta}\} : [\boldsymbol{\sigma}] dV, \quad (2.59)$$

where $[\mathbf{N}]$ and $\{\boldsymbol{\beta}\}$ are interpolation matrices.

In modified Riks static analysis, the implemented UEL updates the right-hand-side vectors $\mathbf{RHS}(1) = \{\mathbf{F}\}$ (residual force vector) and $\mathbf{RHS}(2) = \Delta\boldsymbol{\lambda}(\partial\{\mathbf{F}\}/\partial\{\boldsymbol{\lambda}\})$ (increments of external loads on the element) of the overall system of equations. In this Chapter, as the body force is neglected, the residual force vector $\{\mathbf{F}\}$ could be updated as

$$\{\mathbf{F}\} = \{\mathbf{f}\}^e - \iint_{\omega_e} {}^t[\mathbf{B}(\mathbf{q})] \{\mathbf{N}\} + {}^t[\mathbf{G}]^t[\mathbf{T}_\beta][\mathbf{L}^f][\mathbf{T}_\beta][\mathbf{G}] \{\mathbf{q}\}^e d\omega, \quad (2.60)$$

in which $\{\mathbf{f}\}^e$ represents the total applied loads that must be passed into UEL as the distributed loads by array ADLMAG. The residual increment $\mathbf{RHS}(2)$ could be passed in by array DDLMAG that contains the increments of the distributed loads that are currently active.

Last elementary stiffness matrix $[\mathbf{K}]$ could be derived on the basis of previous work and expressed as

$$[\mathbf{K}] = \iint_{\omega_e} {}^t[\mathbf{B}(\mathbf{q})][\mathbf{L}^m][\mathbf{B}(\mathbf{q})] + {}^t[\mathbf{G}][\hat{\mathbf{N}}][\mathbf{G}] + {}^t[\mathbf{G}]^t[\mathbf{T}_\beta][\mathbf{L}^f][\mathbf{T}_\beta][\mathbf{G}] d\omega, \quad (2.61)$$

which is the same with Eq. (2.44) in Section 2.3.5 and passed into UEL by array AMATRX.

To verify the user element subroutine code, the clamped rectangular membrane under biaxial load of Section 2.4.1 is tested, the parameters remaining the same. Fig. (2.16) proves that the new reduced model implemented into UEL gives the same bifurcation point as the full shell model. Besides, in the same computational condition, the CPU cost time is 422.9 seconds with implemented elements, much less than 40508 seconds needed by the full shell model. This means that the new macroscopic model yields very strong time reductions, especially when there are many wrinkles.

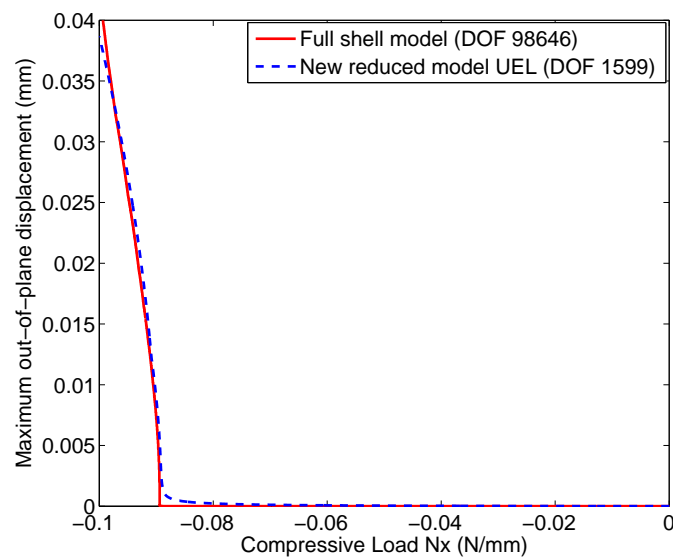


Figure 2.16: Bifurcation path of a rectangular membrane under tension-compression biaxial load for full shell model and new reduced model implemented in UEL subroutine. $L_x = 1000 \text{ mm}$, $L_y = 200 \text{ mm}$, $E = 70\,000 \text{ MPa}$, $h = 0.05 \text{ mm}$, $N_y = 10 \text{ N/mm}$.

2.7 Conclusions

A new reduced-order finite element model has been introduced and implemented in a home-made code and in the commercial package ABAQUS via the user element subroutine UEL. The evolution of the wrinkles is defined in a macroscopic way, by a finite element discretization of some envelopes of the wrinkling patterns. Thus one can use coarse meshes, the size of the elements being related to the variations of the envelope and not to the details of wrinkles. This is confirmed by our numerical experiments and the reduced model needs much less degrees of freedom and computation time than the full shell model. Two numerical examples have been analyzed

and the new reduced model is able to describe correctly and quickly the details of membrane wrinkling, even if the number of wrinkles is small. Especially the classical problem of a rectangular membrane under uniaxial load has been studied in various loading cases and the boundary conditions have a tremendous effect on the stability of the structure. The numerical results show the strong influence of a dimensionless loading parameter on the bifurcation and post-bifurcation behavior.

The present reduced-order model is based on the method of Fourier series with variable coefficients that has been widely used for several structural models: beam on foundation (Damil and Potier-Ferry, 2010; Mhada et al., 2012; Hu et al., 2011), sandwich models (Liu et al., 2012; Yu et al., 2013) or 2D hyperelasticity. Sometimes the behavior near the boundary is not perfectly accounted by the reduced model, but it is possible to re-introduce locally the full model, for instance by using the Arlequin coupling method (Hu et al., 2011; Yu et al., 2013; Ben Dhia, 1998, 2006; Hu et al., 2010). Another possible variant is to introduce more harmonics, for instance as in Mhada et al. (2012) where a complex envelope model has been applied, but compromises between speed and accuracy have to be found.

2D Fourier model for film/substrate instability

Contents

3.1 Introduction	36
3.2 Microscopic model	39
3.2.1 Kinematics	39
3.2.2 Geometric equations and constitutive law	40
3.3 Macroscopic model	42
3.3.1 Internal virtual work of the film	44
3.3.2 Internal virtual work of the substrate	46
3.3.3 External work and weak form of the governing equation . . .	48
3.3.4 Finite element discretisation	48
3.4 Numerical results and discussions	50
3.4.1 Validation	51
3.4.2 Convergence and computation cost	52
3.4.3 Discussions on Fourier-based approach and oscillation locking	56
3.5 Conclusion	60

Abstract

In this Chapter, the technique of the slowly varying Fourier coefficient introduced in Chapter 2 is extended for the study of local wrinkling in two-dimensional film/substrate system, in which, the displacement field is transformed into the slowly variable Fourier coefficient, i.e., the macroscopic displacement field that permits to capture the wrinkling evolution in the system with much less degrees of freedom than the full finite element model. The derived macroscopic non-linear system is solved by the Asymptotic Numerical Method that is very efficient and reliable to capture the bifurcation point and the post-buckling path in wrinkling analyses. In particular, the importance of using the first harmonic of Fourier series

in approximating the axial displacement in substrate is discussed and a spurious phenomenon related to the hypothesis of the used approximation functions within the Fourier-series approach, i.e., oscillation locking, is pointed out. To overcome this phenomenon, modifications on either the Fourier series or the constitutive equations of the substrate are proposed. The efficiency and accuracy of the proposed macroscopic model are demonstrated by the wrinkling simulations for several kinds of film/substrate systems.

Present Chapter corresponds to the published research paper (Huang et al., 2017) [Thin-Walled Structures, 114: 144-153, 2017.]. A self-consistent notation is adopted.

Keywords: Fourier series, Film/substrate system, Wrinkling, Asymptotic Numerical Method.

3.1 Introduction

Compressed stiff films bonded to a compliant substrate can buckle into a pattern presenting sinusoidal wrinkles with constant wavelength (Chen and Hutchinson (2004); Huang et al. (2005)) when compression reaches a critical value. The wrinkles may have an undesirable effect on the system and should be often avoided. However, the periodic nature of the wrinkles in film/substrate systems has nowadays found some applications such as buckling-based metrology method (Stafford et al. (2004)), optical gratings (Harrison et al. (2004)) and stretchable electronics (Rogers et al. (2010)). Since the critical compressive load and details of the instability pattern are often of interest, an accurate yet efficient characterisation of wrinkling of film/substrate system is necessary.

Wrinkling in film/substrates system is very similar to the symmetrical wrinkling in sandwich panel, in which wrinkling stresses for three modes (single sided face wrinkling, in-phase wrinkling and out-of-phase wrinkling) are expressed by a unified, single expression through approximate structural analysis (Allen (1969); Niu and Talreja (1999)). Recently, some non-linear analyses have been developed to comprehend and characterise the wrinkle morphologies. The stiff thin films are usually modelled as a non-linear elastic beam or plate in the works (Bowden et al. (1998); Chen and Hutchinson (2004); Huang et al. (2005); Song et al. (2008)). Differences in these works mainly arise from the used kinematics for the substrate and whether the shear deformation at the film/substrate interface is considered or not. Chen and Hutchinson (2004) modelled the substrate as an elastic foundation of

springs where the in-plane displacements are ignored. Results show that the heringbone mode constitutes a minimum energy configuration. Huang et al. (2005) adopted the three-dimensional elastic field for the substrate and investigated the influence of the Young's modulus, the Poisson's ratio and the thickness of the substrate on the critical strain, amplitude and wavelength of the sinusoidal wrinkles. In their works, the shear deformation in the film/substrate interface was neglected. Mei et al. (2011) assumed a continuous shear strain across the film/substrate interface. This showed that a significant error of the critical strain and the wrinkling wavelength emerges in Huang et al. (2005) when the Poisson's ratio of the substrate decreases. In the above mentioned works, linear elastic constitutive law was assumed in the substrate. Song et al. (2008) considered finite strains and a non-linear constitutive law in the substrate and showed that the wrinkling wavelength decreases with the increase of the pre-strain rather than remaining constant as in Huang et al. (2005). Furthermore, Brau et al. (2011) pointed out that a quadratic non-linearity of the substrate can trigger the period-doubling instability that cannot be captured by a linear substrate. Hutchinson (2013) also studied the influence of the quadratic non-linearity of a neo-Hookean substrate on the mode evolution of the wrinkles in film/substrate systems. Shariyat and Asemi (2016) recently investigated the instability of rectangular FGM plate on elastic foundation under shear loading and found that the stiffness of the elastic foundation greatly affects the angles of deformation waves. Taking into account both accuracy and computational efficiency, higher order functions can be used to approximate kinematics of the substrate and thus to reduce the number of unknowns, see Reddy (1984); Vidal and Polit (2008); Ferreira et al. (2014); Tornabene et al. (2013, 2016). Yang et al. (2015) proposed a higher-order kinematics to model substrate based on the Carrera's Unified Formulation (CUF) (Carrera (2003a); He et al. (2011); Cinefra et al. (2012)). The finite element method was used to solve the higher-order model and accurate results were obtained with low computational cost.

In this Chapter, stemming from an efficient multi-scale approach established by Damil and Potier-Ferry (2010, 2008) that exploits the periodic nature of the wrinkles, an effective two-dimensional Fourier-based model is developed to study the sinusoidal wrinkling in thin stiff films on compliant substrates. The problem unknowns arising from the assumed kinematics (here addressed as "microscopic model" where Euler-Bernoulli's beam theory is used for the film and a two-dimensional plane-strain solid for the substrate) are expanded by Fourier series, which leads to a new problem with the Fourier coefficients as new unknowns exhibiting much slower variation than the original unknowns. This latter problem is

called “macroscopic model”. The derived macroscopic model has the advantage to require very few degrees of freedom to accurately describe the problem under study. Compared to the Landau-Ginzburg technique, the Fourier-based method has two advantages: 1) not only the bifurcation point but also the post-buckling path can be captured and 2) the coupled global and local instability patterns can be incorporated and characterised, see Liu et al. (2012). The established nonlinear system shows strong nonlinearity near and after bifurcation point, and it is a difficult task to solve this kind of nonlinear problem. In this Chapter, the Asymptotic Numerical Method (ANM), known as an effective and robust nonlinear solver in tracing bifurcation path in instability problems proposed by Damil and Potier-Ferry (1990); Cochelin et al. (2007, 1994), is used to solve the established nonlinear equations. So far, the approach based on Fourier series has been successfully used for the wrinkling analysis of non-linear beams resting on Winkler’s foundation (Damil and Potier-Ferry (2010); Mhada et al. (2012)), sandwich beams (Yu et al. (2013); Mhada et al. (2013)) and thin metal films (Damil et al. (2013, 2014); Huang et al. (2015); Attipou et al. (2015)). For the above Fourier-related models, the neutral axial displacement is always assumed not fluctuating and the first order harmonics are ignored, which matches the practical kinematics in these beam or plate elements. However, in the current film/substrate model, the substrate is discretized by continuum elements and shows oscillation at the film/substrate interface. Therefore, the first harmonic of the axial displacement should be introduced to characterise such oscillation. Otherwise, a spurious stiffening effect (named as “oscillation locking”) would occur if only the zero order of Fourier series for the axial displacement is used as introduced in previous works. To overcome this difficulty, two manners are proposed: 1) the first one is to enrich the Fourier-series expansion and 2) the second one is to modify the elastic coefficient of the substrate.

This Chapter is structured as follows. The two-dimensional microscopic model for film/substrate systems is introduced in Section 3.2. In Section 3.3, the Fourier-related macroscopic model and the corresponding finite element are derived. In Section 3.4, numerical tests are performed to assess the established macroscopic model, and discussion on the importance of the first harmonic in continuum element and the oscillation locking is made.

3.2 Microscopic model

3.2.1 Kinematics

A two-dimensional elastic stiff film bound to an elastic soft compliant substrate is considered as depicted in Fig. 3.1: x and z are the axial and through-the-thickness coordinates, h_f and h_s are the thickness of the top film and the substrate, respectively, h_t is the total thickness of the structure. The length and the width are denoted respectively by L and b . The thin film is modelled as an elastic Euler-

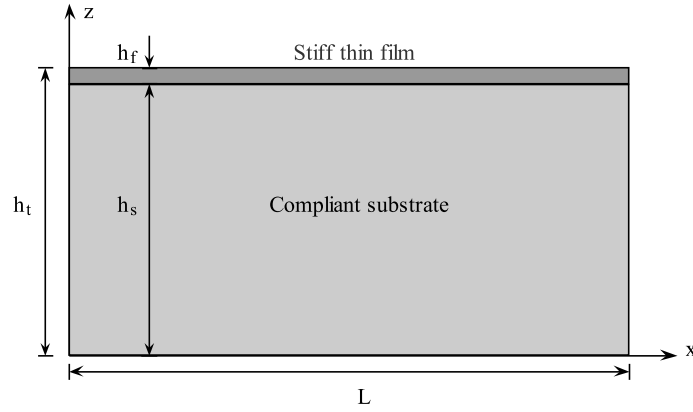


Figure 3.1: Sketch of an elastic thin stiff film on a compliant substrate.

Bernoulli's beam:

$$\begin{aligned}\mathcal{U}^f(x, z) &= u^f(x) - \left(z - \frac{h_f + 2h_s}{2}\right) w_{,x}^f(x) \quad z \in [h_s, h_t] \\ \mathcal{W}^f(x, z) &= w^f(x)\end{aligned}\quad (3.1)$$

where superscript “ f ” stands for the film, $\mathcal{U}(x, z)$ and $\mathcal{W}(x, z)$ are the axial and through-the-thickness components of the displacement field $\mathbf{U}(x, z)$ and u^f and w^f the two unknown displacement functions. A coordinate subscript preceded by comm “ $,x$ ” stands for a partial derivative. The substrate, denoted by “ s ”, is modelled as a plane-strain elastic solid:

$$\begin{aligned}\mathcal{U}^s(x, z) &= u^s(x, z) \\ \mathcal{W}^s(x, z) &= w^s(x, z) \quad z \in [0, h_s]\end{aligned}\quad (3.2)$$

The displacement field at interface of the film and substrate should satisfy the following compatibility conditions:

$$\begin{aligned}\mathcal{U}^f(x, h_s) &= \mathcal{U}^s(x, h_s) \\ \mathcal{W}^f(x, h_s) &= \mathcal{W}^s(x, h_s)\end{aligned}\quad (3.3)$$

The Constrained Variational Principle (CVP) is used to ensure the congruency of the displacement field at the interface:

$$\Gamma = \{(x, y, z) : x \in [0, L], y \in [-b/2, b/2], z = h_s\} \quad (3.4)$$

The following constrain term $\mathcal{L}(\boldsymbol{\mu}, \mathbf{u})$ is obtained by introducing the Lagrange multipliers $\boldsymbol{\mu} = \{\mu_1, \mu_2\}$ as fictitious gluing forces:

$$\mathcal{L}(\boldsymbol{\mu}, \mathbf{u}) = \int_{\Gamma} \left\{ \mu_1 \left[\mathcal{U}^f(x, h_s) - \mathcal{U}^s(x, h_s) \right] + \mu_2 \left[\mathcal{W}^f(x, h_s) - \mathcal{W}^s(x, h_s) \right] \right\} d\Gamma \quad (3.5)$$

3.2.2 Geometric equations and constitutive law

The geometric equations and constitute law are supposed to meet the following hypotheses:

1. the material behaviour is linear elastic and described by the Hooke's law,
2. the geometrical non-linearity is considered in the film only and the strain-displacement relationship is described by the Green-Lagrange strain,
3. the substrate undergoes small displacements.

The above assumptions are translated into the following equations:

$$\begin{aligned}\sigma_{xx}^f &= E_f \epsilon_{xx}^f = E_f \left[\mathcal{U}_{,x}^f + \frac{1}{2} \left(\mathcal{W}_{,x}^f \right)^2 \right] \\ \sigma_{xx}^s &= C_{11}^s \epsilon_{xx}^s + C_{13}^s \epsilon_{zz}^s = C_{11}^s \mathcal{U}_{,x}^s + C_{13}^s \mathcal{W}_{,z}^s \\ \sigma_{zz}^s &= C_{13}^s \epsilon_{xx}^s + C_{33}^s \epsilon_{zz}^s = C_{13}^s \mathcal{U}_{,x}^s + C_{33}^s \mathcal{W}_{,z}^s \\ \sigma_{xz}^s &= 2C_{55}^s \epsilon_{xz}^s = C_{55}^s \left(\mathcal{U}_{,z}^s + \mathcal{W}_{,x}^s \right)\end{aligned}\quad (3.6)$$

with ϵ_{ij} and σ_{ij} being the strain and stress components, C_{ij} the material stiffness coefficients

$$\begin{aligned} C_{11}^s = C_{33}^s &= \frac{1 - \nu_s}{(1 + \nu_s)(1 - 2\nu_s)} E_s \\ C_{13}^s &= \frac{\nu_s}{(1 + \nu_s)(1 - 2\nu_s)} E_s \\ C_{55}^s &= \frac{E_s}{2(1 + \nu_s)} \end{aligned} \quad (3.7)$$

E the Young's modulus and ν the Poisson's ratio.

The weak form of the governing equations is obtained by the Principle of Virtual Displacement accounting for the constraint in Eq. (3.5):

$$\delta \mathcal{P}_{\text{int}} + \delta \mathcal{L} = \delta \mathcal{P}_{\text{ext}} \quad (3.8)$$

where δ stands for a virtual variation, \mathcal{P}_{int} is the internal work and \mathcal{P}_{ext} the external work. The internal virtual work is expressed as:

$$\delta \mathcal{P}_{\text{int}} = \int_{V^f} \sigma_{xx}^f \delta \epsilon_{xx}^f dV + \int_{V^s} (\sigma_{xx}^s \delta \epsilon_{xx}^s + \sigma_{zz}^s \delta \epsilon_{zz}^s + 2\sigma_{xz}^s \delta \epsilon_{xz}^s) dV \quad (3.9)$$

where the V stands for volume. By using Eqs. (3.1) to (3.7) and integrating through the thickness of the film, the virtual internal work in Eq. (3.9) rewrites:

$$\delta \mathcal{P}_{\text{int}} = \int_0^L \delta \gamma^{fT} \mathbf{S}^f dx + b \int_{\omega^s} \delta \gamma^{sT} \mathbf{S}^s d\omega \quad (3.10)$$

where the superscript "T" stands for transposition and $\omega^s = L \times h_s \in \mathbb{R}^2$ is the substrate integration domain on the plane xz . \mathbf{S}^f and \mathbf{S}^s are the film and substrate stress vectors:

$$\begin{aligned} \mathbf{S}^f &= \mathbf{D}^f \left[\mathbf{H}^f + \frac{1}{2} \mathbf{A}(\boldsymbol{\theta}^f) \right] \boldsymbol{\theta}^f \\ \mathbf{S}^s &= \mathbf{D}^s \mathbf{H}^s \boldsymbol{\theta}^s \end{aligned} \quad (3.11)$$

in which

$$\begin{aligned} \mathbf{D}^f &= \begin{bmatrix} E_f h_f b & 0 \\ 0 & \frac{1}{12} E_f b h_f^3 \end{bmatrix} \\ \mathbf{H}^f &= \begin{bmatrix} 1 & 0 & 0 \\ 0 & 0 & 1 \end{bmatrix} \\ \mathbf{A}(\boldsymbol{\theta}^f) &= \begin{bmatrix} 0 & w_{,x}^f & 0 \\ 0 & 0 & 0 \end{bmatrix} \end{aligned} \quad (3.12)$$

and

$$\begin{aligned} \mathbf{D}^s &= \begin{bmatrix} C_{11}^s & C_{13}^s & 0 \\ C_{13}^s & C_{33}^s & 0 \\ 0 & 0 & C_{55}^s \end{bmatrix} \\ \mathbf{H}^s &= \begin{bmatrix} 1 & 0 & 0 & 0 \\ 0 & 0 & 0 & 1 \\ 0 & 1 & 1 & 0 \end{bmatrix} \end{aligned} \quad (3.13)$$

$\boldsymbol{\theta}$ is the displacement gradient

$$\begin{aligned} \boldsymbol{\theta}^{fT} &= \left\{ u_{0,x}^f \quad w_{,x}^f \quad w_{,xx}^f \right\} \\ \boldsymbol{\theta}^{sT} &= \left\{ u_{,x}^s \quad u_{,z}^s \quad w_{,x}^s \quad w_{,z}^s \right\} \end{aligned} \quad (3.14)$$

and $\boldsymbol{\gamma}$ the generalised strain vector.

3.3 Macroscopic model

The double-scale approach based on Fourier series with slowly varying coefficients is applied to derive the film/substrate macroscopic model. The characteristic direction and period are described by a wave-number q that is assumed to be given. The unknown displacement field $\mathbf{U}(x, z)$ is written in the following form:

$$\mathbf{U}(x, z) = \sum_{j=-\infty}^{+\infty} \mathbf{U}_j(x, z) e^{ijqx} \quad (3.15)$$

where i is the imaginary unit and the Fourier coefficient $\mathbf{U}_j(x, z)$ denotes the envelope of the j th order harmonic that is conjugated with $\mathbf{U}_{-j}(x, z)$. \mathbf{U}_j varies slowly in the axial direction over a period $\left[x, x + \frac{2\pi}{q} \right]$ of the oscillation. The wave-number q is defined as

$$q = \frac{\pi}{L} q_0 \quad (3.16)$$

in which q_0 is a chosen integer wave-parameter: $q_0 \in \mathbb{N}$ and $q_0 \geq 2$. Here a macroscopic model with three envelopes $\mathbf{U}_0(x, z)$, $\mathbf{U}_1(x, z)$ and $\mathbf{U}_{-1}(x, z)$, as pictured in Fig. 3.2, is considered. \mathbf{U}_0 can be identified as the mean value while $\mathbf{U}_{\pm 1}$ represent the envelope or the amplitude of the spatial oscillations.

Furthermore, some other simplified assumptions are made. The in-plane displacement of the neutral plane of the film $u^f(x)$ and the applied external force F do not fluctuate according to Damil and Potier-Ferry (2010). This means that their

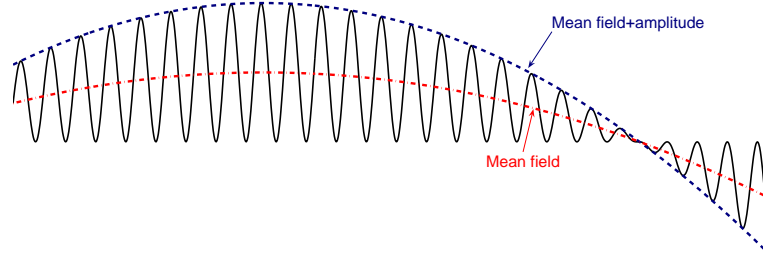


Figure 3.2: At least two macroscopic envelopes are necessary to describe a nearly periodic response: the mean field and the amplitude of the fluctuation.

Fourier series expansion reduces to a single term

$$\begin{aligned} u^f &= u_0^f \\ F &= F_0 \end{aligned} \quad (3.17)$$

In this Chapter, we focus on the local instability of film/substrate system, so the mean field of transverse displacement is nearly unchanged along the x direction and it leads to

$$\mathcal{W}_0(x, z) = 0 \quad (3.18)$$

According to the above assumptions, the transverse displacement \mathcal{W} can be explicitly expressed as

$$\mathcal{W}(x, z) = 2\hat{\mathcal{W}}(x, z) \cos(qx + \phi) \quad (3.19)$$

where the envelop $\hat{\mathcal{W}} \in \mathbb{R}$ and the phase angle ϕ are used in place of the complex conjugate $\mathcal{W}_{\pm 1}$. The phase angle ϕ could be variant to describe the phase modulation in the evolution of instability Mhada et al. (2012). For the sake of simplicity, ϕ is assumed to be constant and equal to $\pm\frac{\pi}{2}$ (see Liu et al. (2012) and Yu et al. (2013) for more details) and the previous equation becomes

$$\mathcal{W}(x, z) = 2\hat{\mathcal{W}}(x, z) \sin(qx) \quad (3.20)$$

By substituting Eqs. (3.17) and (3.20) into Eq. (3.1), the displacement fields of the film can be rewritten as

$$\begin{aligned} \mathcal{U}^f(x, z) &= u_0^f(x) - \left(z - \frac{h_f + 2h_s}{2} \right) \left(2qw_1^f \cos(qx) + 2w_{1,x}^f \sin(qx) \right) \quad z \in [h_s, h_t] \\ \mathcal{W}^f(x, z) &= 2w_1^f(x) \sin(qx) \end{aligned} \quad (3.21)$$

Finally, some properties are introduced to obtain the macroscopic governing

equations. Given two functions $a(x)$ and $b(x)$ expanded by Fourier series with slowly varying coefficients, the following identities hold, see Damil and Potier-Ferry (2010):

$$\int_0^L a(x) b(x) dx = \int_0^L \sum_{j=-\infty}^{\infty} a_j(x) b_{-j}(x) dx \quad (3.22)$$

$$\left(\frac{da}{dx}\right)_j = (a')_j = \left(\frac{d}{dx} + ij q\right) a_j = (a_j)' + ij q a_j \quad (3.23)$$

$$\left(\frac{d^2 a}{dx^2}\right)_j = (a'')_j = \left(\frac{d}{dx} + ij q\right)^2 a_j = (a_j)'' + 2ij q (a_j)' - j^2 q^2 a_j \quad (3.24)$$

$$(ab)_j = \sum_{j_1=-\infty}^{+\infty} a_{j_1} b_{j-j_1} \quad (3.25)$$

3.3.1 Internal virtual work of the film

By applying Eq. (3.15) and by virtue of the properties in Eqs. (3.22)-(3.25), the virtual internal work of the film becomes:

$$\delta \mathcal{P}_{\text{int}}^f = \int_0^L \sum_{j=-1}^{+1} \delta \gamma_{-j}^{fT} \mathbf{S}_j^f dx = \int_0^L \left(\delta \gamma_0^{fT} \mathbf{S}_0^f + 2\delta \gamma_{1R}^{fT} \mathbf{S}_{1R}^f + 2\delta \gamma_{1I}^{fT} \mathbf{S}_{1I}^f \right) dx \quad (3.26)$$

The constitutive law of the film reads

$$\begin{aligned} \mathbf{S}_0^f &= \mathbf{D}^f \boldsymbol{\gamma}_0^f \\ \mathbf{S}_{1R}^f &= \mathbf{D}^f \boldsymbol{\gamma}_{1R}^f \\ \mathbf{S}_{1I}^f &= \mathbf{D}^f \boldsymbol{\gamma}_{1I}^f \end{aligned} \quad (3.27)$$

and the strains are written as

$$\begin{aligned} \boldsymbol{\gamma}_0^f &= \mathbf{H}^f \boldsymbol{\theta}_0^f + \frac{1}{2} \mathbf{A} \left(\boldsymbol{\theta}_0^f \right) \boldsymbol{\theta}_0^f + \mathbf{A} \left(\boldsymbol{\theta}_{1R}^f \right) \boldsymbol{\theta}_{1R}^f + \mathbf{A} \left(\boldsymbol{\theta}_{1I}^f \right) \boldsymbol{\theta}_{1I}^f \\ \boldsymbol{\gamma}_{1R}^f &= \mathbf{H}^f \boldsymbol{\theta}_{1R}^f + \mathbf{A} \left(\boldsymbol{\theta}_0^f \right) \boldsymbol{\theta}_{1R}^f \\ \boldsymbol{\gamma}_{1I}^f &= \mathbf{H}^f \boldsymbol{\theta}_{1I}^f + \mathbf{A} \left(\boldsymbol{\theta}_0^f \right) \boldsymbol{\theta}_{1I}^f \end{aligned} \quad (3.28)$$

The vectors \mathbf{S}^f , $\boldsymbol{\gamma}^f$ and $\boldsymbol{\theta}^f$ are the Fourier series expansion of the unknowns and the subscripts “0”, “1R” and “1I” stand for the zero- (real value), first-order harmonic ($j = \pm 1$, real-value part “R” and complex-value part “I”).

For instance, the Fourier series expansion of $\boldsymbol{\theta}^f$ can be written as

$$\boldsymbol{\theta}^f = \sum_{j=-1}^{+1} \boldsymbol{\theta}_j^f e^{ijqx} \quad (3.29)$$

where, according to the hypotheses given in the previous paragraph

$$\begin{aligned} \boldsymbol{\theta}_0^{fT} &= \left\{ u_{0,x}^f \quad 0 \quad 0 \right\} \\ \boldsymbol{\theta}_1^{fT} &= \left\{ 0 \quad w_{1,x}^f + iqw_1^f \quad w_{1,xx}^f - q^2w_1^f + i2qw_{1,x}^f \right\} \end{aligned} \quad (3.30)$$

$\boldsymbol{\theta}_1^f$ can be also written as

$$\boldsymbol{\theta}_1^f = \Re\left(\boldsymbol{\theta}_1^f\right) + i\Im\left(\boldsymbol{\theta}_1^f\right) = \boldsymbol{\theta}_{1R}^f + i\boldsymbol{\theta}_{1I}^f \quad (3.31)$$

To avoid spurious oscillations (see details in Damil and Potier-Ferry (2010)), the second derivative of the envelope w_1^f in Eq. (3.30) is eliminated. After integration by part, the second term in Eq. (3.30) reads

$$\boldsymbol{\theta}_1^{fT} = \left\{ 0 \quad w_{1,x}^f + iqw_1^f \quad -q^2w_1^f + i\sqrt{6}qw_{1,x}^f \right\} \quad (3.32)$$

By introducing the following generalised stress $\mathbf{S}_{\text{gen}}^f$, strain $\boldsymbol{\Gamma}_{\text{gen}}^f$ and displacement gradient $\boldsymbol{\theta}_{\text{gen}}^f$ vectors:

$$\begin{aligned} \mathbf{S}_{\text{gen}}^{fT} &= \left\{ \mathbf{S}_0^{fT} \quad \mathbf{S}_{1R}^{fT} \quad \mathbf{S}_{1I}^{fT} \right\} \\ \boldsymbol{\Gamma}_{\text{gen}}^{fT} &= \left\{ \gamma_0^{fT} \quad 2\gamma_{1R}^{fT} \quad 2\gamma_{1I}^{fT} \right\} \\ \boldsymbol{\theta}_{\text{gen}}^{fT} &= \left\{ \boldsymbol{\theta}_0^{fT} \quad \boldsymbol{\theta}_{1R}^{fT} \quad \boldsymbol{\theta}_{1I}^{fT} \right\} \end{aligned} \quad (3.33)$$

The generalized macroscopic stress-strain relation can be consequently written as:

$$\begin{aligned} \mathbf{S}_{\text{gen}}^f &= \mathbf{D}_{\text{gen}}^f \boldsymbol{\Gamma}_{\text{gen}}^f \\ \boldsymbol{\Gamma}_{\text{gen}}^f &= \mathbf{H}_{\text{gen}}^f \boldsymbol{\theta}_{\text{gen}}^f + \frac{1}{2} \mathbf{A} \left(\boldsymbol{\theta}_{\text{gen}}^f \right) \boldsymbol{\theta}_{\text{gen}}^f \end{aligned} \quad (3.34)$$

where

$$\begin{aligned}
 \mathbf{D}_{\text{gen}}^f &= \begin{bmatrix} \mathbf{D}^f & \mathbf{0} & \mathbf{0} \\ \mathbf{0} & \frac{1}{2}\mathbf{D}^f & \mathbf{0} \\ \mathbf{0} & \mathbf{0} & \frac{1}{2}\mathbf{D}^f \end{bmatrix} \\
 \mathbf{H}_{\text{gen}}^f &= \begin{bmatrix} \mathbf{H}^f & \mathbf{0} & \mathbf{0} \\ \mathbf{0} & 2\mathbf{H}^f & \mathbf{0} \\ \mathbf{0} & \mathbf{0} & 2\mathbf{H}^f \end{bmatrix} \\
 \mathbf{A}(\boldsymbol{\theta}_{\text{gen}}^f) &= 2 \begin{bmatrix} \frac{1}{2}\mathbf{A}(\boldsymbol{\theta}_0^f) & \mathbf{A}(\boldsymbol{\theta}_{1R}^f) & \mathbf{A}(\boldsymbol{\theta}_{1I}^f) \\ \mathbf{A}(\boldsymbol{\theta}_{1R}^f) & \mathbf{A}(\boldsymbol{\theta}_0^f) & \mathbf{0} \\ \mathbf{A}(\boldsymbol{\theta}_{1I}^f) & \mathbf{0} & \mathbf{A}(\boldsymbol{\theta}_0^f) \end{bmatrix}
 \end{aligned} \tag{3.35}$$

The virtual work of the film finally reads:

$$\delta \mathcal{P}_{\text{int}}^f = \int_0^L \delta \boldsymbol{\Gamma}_{\text{gen}}^{fT} \mathbf{S}_{\text{gen}}^f dx \tag{3.36}$$

3.3.2 Internal virtual work of the substrate

The virtual work of the substrate is obtained in a similar manner:

$$\delta \mathcal{P}_{\text{int}}^s = b \int_{\omega^s} \sum_{j=-1}^{+1} \delta \gamma_{-j}^{sT} \mathbf{S}_j^s d\omega^s = b \int_{\omega^s} \delta \boldsymbol{\Gamma}_{\text{gen}}^{sT} \mathbf{S}_{\text{gen}}^s d\omega \tag{3.37}$$

where $\boldsymbol{\Gamma}_{\text{gen}}^s$ and $\mathbf{S}_{\text{gen}}^s$ are the generalised strain and the generalised stress in the substrate, respectively. The following constitutive and geometric equations hold

$$\begin{aligned}
 \mathbf{S}_{\text{gen}}^s &= \mathbf{D}_{\text{gen}}^s \boldsymbol{\Gamma}_{\text{gen}}^s \\
 \boldsymbol{\Gamma}_{\text{gen}}^s &= \mathbf{H}_{\text{gen}}^s \boldsymbol{\theta}_{\text{gen}}^s
 \end{aligned} \tag{3.38}$$

where the strain-displacement relationship is assumed to be linear. The matrices $\mathbf{D}_{\text{gen}}^s$ and $\mathbf{H}_{\text{gen}}^s$ are defined in a manner similar to $\mathbf{D}_{\text{gen}}^f$ and $\mathbf{H}_{\text{gen}}^f$, see Eq. (3.35), and they are not reported for the sake of brevity. The generalised displacement gradient $\boldsymbol{\theta}_{\text{gen}}^s$ is:

$$\boldsymbol{\theta}_{\text{gen}}^{sT} = \left\{ \boldsymbol{\theta}_0^{sT} \quad \boldsymbol{\theta}_{1R}^{sT} \quad \boldsymbol{\theta}_{1I}^{sT} \right\} \tag{3.39}$$

in which

$$\begin{aligned}\boldsymbol{\theta}_0^{sT} &= \left\{ u_{0,x}^s \quad u_{0,z}^s \quad 0 \quad 0 \right\} \\ \boldsymbol{\theta}_{1R}^{sT} &= \left\{ u_{1R,x}^s - qu_{1I}^s \quad u_{1R,z}^s \quad w_{1,x}^s \quad w_{1,z}^s \right\} \\ \boldsymbol{\theta}_{1I}^{sT} &= \left\{ qu_{1R}^s + u_{1I,x}^s \quad u_{1I,z}^s \quad qw_1^s \quad 0 \right\}\end{aligned}\quad (3.40)$$

It should be noted that the first-order harmonic of the axial displacement should be accounted for, otherwise the in-plane displacement \mathcal{U}^s would vary slowly along the x direction, which will result in a spurious over-stiffening phenomenon named ‘‘oscillation locking’’, see details in Section 3.4.3.

The congruency of the displacement field at film and substrate interface Γ is imposed by means of the Lagrange multiplier $\boldsymbol{\mu}$ and the coupling variational term \mathcal{L} in Eq. (3.5), which is realised by coupling the envelopes of the displacement field

$$\begin{aligned}\mathcal{U}_0^f(x, h_s) &= \mathcal{U}_0^s(x, h_s) \\ \mathcal{U}_1^f(x, h_s) &= \mathcal{U}_1^s(x, h_s) \\ \mathcal{W}_0^f(x, h_s) &= \mathcal{W}_0^s(x, h_s) \\ \mathcal{W}_1^f(x, h_s) &= \mathcal{W}_1^s(x, h_s)\end{aligned}\quad (3.41)$$

Its virtual variation thus reads

$$\begin{aligned}\delta\mathcal{L} &= \mathcal{L}(\delta\boldsymbol{\mu}, \mathbf{u}) + \mathcal{L}(\boldsymbol{\mu}, \delta\mathbf{u}) = \\ &\int_{\Gamma} \left\{ \delta\mu_{u_0} \left[\mathcal{U}_0^f(x, h_s) - \mathcal{U}_0^s(x, h_s) \right] + \delta\mu_{u_{1R}} \left[\mathcal{U}_{1R}^f(x, h_s) - \mathcal{U}_{1R}^s(x, h_s) \right] + \right. \\ &\quad \left. \delta\mu_{u_{1I}} \left[\mathcal{U}_{1I}^f(x, h_s) - \mathcal{U}_{1I}^s(x, h_s) \right] + \delta\mu_{w_1} \left[\mathcal{W}_1^f(x, h_s) - \mathcal{W}_1^s(x, h_s) \right] \right\} d\Gamma + \\ &\int_{\Gamma} \left\{ \mu_{u_0} \left[\delta\mathcal{U}_0^f(x, h_s) - \delta\mathcal{U}_0^s(x, h_s) \right] + \mu_{u_{1R}} \left[\delta\mathcal{U}_{1R}^f(x, h_s) - \delta\mathcal{U}_{1R}^s(x, h_s) \right] + \right. \\ &\quad \left. \mu_{u_{1I}} \left[\delta\mathcal{U}_{1I}^f(x, h_s) - \delta\mathcal{U}_{1I}^s(x, h_s) \right] + \mu_{w_1} \left[\delta\mathcal{W}_1^f(x, h_s) - \delta\mathcal{W}_1^s(x, h_s) \right] \right\} d\Gamma = \\ &b \int_0^L \left\{ \delta\mu_{u_0} \left[u_0^f - u_0^s \right] + \delta\mu_{u_{1R}} \left[h_f q w_1^f - 2u_{1R}^s \right] + \right. \\ &\quad \left. \delta\mu_{u_{1I}} \left[h_f w_{1,x}^f - (-2u_{1I}^s) \right] + \delta\mu_{w_1} \left[2w_1^f - 2w_1^s \right] \right\} dx + \\ &b \int_0^L \left\{ \mu_{u_0} \left[\delta u_0^f - \delta u_0^s \right] + \mu_{u_{1R}} \left[h_f q \delta w_1^f - 2\delta u_{1R}^s \right] + \right. \\ &\quad \left. \mu_{u_{1I}} \left[h_f \delta w_{1,x}^f - (-2\delta u_{1I}^s) \right] + \mu_{w_1} \left[2\delta w_1^f - 2\delta w_1^s \right] \right\} dx\end{aligned}\quad (3.42)$$

The matrix form of Eq. (3.42) reads:

$$\delta\mathcal{L}(\boldsymbol{\mu}, \mathbf{u}) = \int_0^L \left[\delta\boldsymbol{\mu}^T \left(\mathbf{D}_l^f \boldsymbol{\theta}_l^f - \mathbf{D}_l^s \boldsymbol{\theta}_l^s \right) + \left(\delta\boldsymbol{\theta}_l^{fT} \mathbf{D}_l^{fT} - \delta\boldsymbol{\theta}_l^{sT} \mathbf{D}_l^{sT} \right) \boldsymbol{\mu} \right] dx \quad (3.43)$$

where the subscript “ l ” stands for the terms related to the Lagrange multiplier, $\boldsymbol{\theta}_l^f$ and $\boldsymbol{\theta}_l^s$ are, respectively, the displacement gradient vectors of the film and the substrate

$$\begin{aligned}\boldsymbol{\theta}_l^{fT} &= \left\{ u_0^f \quad w_1^f \quad w_{1,x}^f \right\} \\ \boldsymbol{\theta}_l^{sT} &= \left\{ u_0^s \quad u_{1R}^s \quad u_{1I}^s \quad w_1^s \right\}\end{aligned}\quad (3.44)$$

\mathbf{D}_l^f and \mathbf{D}_l^s are the corresponding constant matrices that can be derived conveniently from Eq. (3.42), which are not shown here for the sake of brevity.

3.3.3 External work and weak form of the governing equation

Due to an external load \mathbf{F} applied on the film lateral surface, see Fig. 3, the external virtual work is supposed to be:

$$\delta \mathcal{P}_{\text{ext}} = \lambda b \delta \boldsymbol{\theta}_{\text{gen}}^{fT} \mathbf{F} \quad (3.45)$$

where λ is a “load parameter”. The macroscopic governing equation, finally, reads:

$$\begin{aligned}\int_0^L \left[\delta \boldsymbol{\theta}_{\text{gen}}^{fT} \left(\mathbf{H}_{\text{gen}}^{fT} + \mathbf{A}^T \left(\boldsymbol{\theta}_{\text{gen}}^f \right) \right) \mathbf{S}_{\text{gen}}^f \right] dx + b \int_{\omega^s} \delta \boldsymbol{\theta}_{\text{gen}}^{sT} \mathbf{D}_{\text{gen}}^s \boldsymbol{\theta}_{\text{gen}}^s d\omega + \\ \int_0^L \left[\delta \boldsymbol{\mu}^T \left(\mathbf{D}_l^f \boldsymbol{\theta}_l^f - \mathbf{D}_l^s \boldsymbol{\theta}_l^s \right) + \left(\delta \boldsymbol{\theta}_l^{fT} \mathbf{D}_l^{fT} - \delta \boldsymbol{\theta}_l^{sT} \mathbf{D}_l^{sT} \right) \boldsymbol{\mu} \right] dx = \lambda b \delta \boldsymbol{\theta}_{\text{gen}}^{fT} \mathbf{F}\end{aligned}\quad (3.46)$$

3.3.4 Finite element discretisation

The finite element method is used to solve the non-linear system in Eq. (3.46). A three-node one-dimensional element with two degrees of freedom

$$\mathbf{v}_i^{efT} = \left\{ u_{0i}^{ef} \quad w_{1i}^{ef} \right\} \quad (3.47)$$

for each node i is used for the film, whereas two-dimensional eight-node elements with four degrees of freedom

$$\mathbf{v}_i^{esT} = \left\{ u_{0i}^{es} \quad u_{1Ri}^{es} \quad u_{1Ii}^{es} \quad w_{1i}^{es} \right\} \quad (3.48)$$

for each node i is used for the substrate. The Lagrange multiplier is discretised as the film unknowns:

$$\mathbf{v}_i^{elT} = \left\{ \mu_{u_{0i}}^e \quad \mu_{u_{1Ri}}^e \quad \mu_{u_{1Ii}}^e \quad \mu_{w_{1i}}^e \right\} \quad (3.49)$$

The elemental nodal unknown vectors can be written as:

$$\begin{aligned} \mathbf{v}^{efT} &= \left\{ \mathbf{v}_I^{efT} \quad \mathbf{v}_{II}^{efT} \quad \mathbf{v}_{III}^{efT} \right\} \\ \mathbf{v}^{esT} &= \left\{ \mathbf{v}_I^{esT} \quad \mathbf{v}_{II}^{esT} \quad \mathbf{v}_{III}^{esT} \quad \mathbf{v}_{IV}^{esT} \quad \mathbf{v}_V^{esT} \quad \mathbf{v}_{VI}^{esT} \quad \mathbf{v}_{VII}^{esT} \quad \mathbf{v}_{VIII}^{esT} \right\} \\ \mathbf{v}^{elT} &= \left\{ \mathbf{v}_I^{elT} \quad \mathbf{v}_{II}^{elT} \quad \mathbf{v}_{III}^{elT} \right\} \end{aligned} \quad (3.50)$$

The roman numbers denote the node order in an element. For example, I indicates the first node of the element.

The vector unknowns \mathbf{v}^{efT} and \mathbf{v}^{elT} are characterised by three-node quadratic shape functions. The serendipity eight-node shape functions are used for the unknown vector \mathbf{v}^{esT} . The shape functions are not presented for the sake of brevity, which can be found in Bathe (2006).

The element displacement gradient vectors $\boldsymbol{\theta}_{\text{gen}}^{ef}$, $\boldsymbol{\theta}_{\text{gen}}^{es}$, $\boldsymbol{\theta}_l^{ef}$, $\boldsymbol{\theta}_l^{es}$ and the Lagrange multiplier $\boldsymbol{\mu}^e$ are expressed as:

$$\begin{aligned} \boldsymbol{\theta}_{\text{gen}}^{ef} &= \mathbf{G}^f \mathbf{v}^{ef} \\ \boldsymbol{\theta}_{\text{gen}}^{es} &= \mathbf{G}^s \mathbf{v}^{es} \\ \boldsymbol{\theta}_l^{ef} &= \mathbf{G}_l^f \mathbf{v}^{ef} \\ \boldsymbol{\theta}_l^{es} &= \mathbf{G}_l^s \mathbf{v}^{es} \\ \boldsymbol{\mu}^e &= \mathbf{G}^l \mathbf{v}^{el} \end{aligned} \quad (3.51)$$

where \mathbf{G}^f , \mathbf{G}^s , \mathbf{G}_l^f , \mathbf{G}_l^s and \mathbf{G}^l contain the shape functions and their derivatives, see Crisfield (1996).

Finally, the weak form of the governing equations discretised by the finite element reads

$$\begin{aligned} &\int_0^{l_e} \delta \mathbf{v}^{efT} \mathbf{B}^T \left(\mathbf{v}^{ef} \right) \mathbf{S}_{\text{gen}}^{ef} dx + \int_{\omega_s^e} \delta \mathbf{v}^{esT} \mathbf{K}^s \mathbf{v}^{es} d\omega + \\ &\int_0^{l_e} \left[\delta \mathbf{v}^{elT} \left(\mathbf{C}_1 \mathbf{v}^{ef} - \mathbf{C}_2 \mathbf{v}^{es} \right) + \left(\delta \mathbf{v}^{efT} \mathbf{C}_1^T - \delta \mathbf{v}^{esT} \mathbf{C}_2^T \right) \mathbf{v}^{el} \right] dx = \lambda \delta \mathbf{v}^{efT} \mathbf{f}^e \end{aligned} \quad (3.52)$$

where the following relations and matrix terms are introduced

$$\begin{aligned}
\mathbf{S}_{\text{gen}}^{ef} &= \mathbf{D}_{\text{gen}}^f \left[\mathbf{B}_{\text{lin}}^f + \frac{1}{2} \mathbf{B}_{\text{nl}}^f(\mathbf{v}^{ef}) \right] \mathbf{v}^{ef} \\
\mathbf{B}(\mathbf{v}^{ef}) &= \mathbf{B}_{\text{lin}}^f + \mathbf{B}_{\text{nl}}^f(\mathbf{v}^{ef}) \\
\mathbf{B}_{\text{lin}}^f &= \mathbf{H}_{\text{gen}}^f \mathbf{G}^f \\
\mathbf{B}_{\text{nl}}^f(\mathbf{v}^{ef}) &= \mathbf{A}(\mathbf{v}^{ef}) \mathbf{G}^f \\
\mathbf{K}^s &= \mathbf{G}^{sT} \mathbf{D}_{\text{gen}}^s \mathbf{G}^s \\
\mathbf{C}_1 &= \mathbf{G}^{lT} \mathbf{D}_l^f \mathbf{G}_l^f \\
\mathbf{C}_2 &= \mathbf{G}^{lT} \mathbf{D}_l^s \mathbf{G}_l^s
\end{aligned} \tag{3.53}$$

The resulting non-linear problem is solved by the Asymptotic Numerical Method (Cochelin et al. (1994)). For each element, the unknowns are determined at the nodes and the stress at the Gauss points. Details on the use of the ANM can be easily found in our papers (Liu et al. (2012); Yu et al. (2015); Yang et al. (2015)) and thus are not presented in this work. The obtained macroscopic model is referred as “macroscopic model I”.

3.4 Numerical results and discussions

The film/substrate system is subjected to compressive concentrated forces of equal modulus F and opposite verse as illustrated in Fig. 3.3. The forces act along the axial direction at the through-the-thickness mid point of the film. The lower

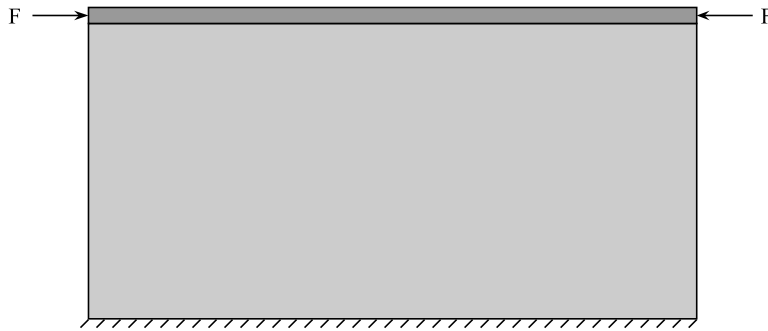


Figure 3.3: Sketch of the film/substrate system under compression forces

surface of the substrate ($z/h_t = 0$) is fixed. This boundary condition is obtained by setting $u_0^s(x, 0)$, $u_{1R}^s(x, 0)$, $u_{1I}^s(x, 0)$ and $w_1^s(x, 0)$ equal to zero. The vertical displacements at $x/L = 0$ and 1 are also fixed by imposing a nil value for $w_1^s(0, z)$,

$w_1^s(L, z)$, $w_1^f(0, z)$ and $w_1^f(L, z)$.

The results obtained by the macroscopic model are compared with a two-dimensional non-linear elasticity solution obtained by the finite element software ABAQUS. The latter is referred to as either “2D full model” or “ABAQUS”. For this ABAQUS solution, the film is modelled by 3-node beam elements (B22) and the substrate by 8-node bi-quadratic plane-strain elements (CPE8R) with reduced integration (Yang et al. (2015)). To ensure the displacement congruency at the film/substrate interface, the degrees of freedom in the beam elements are bound to the plane-strain elements by using “tie” constraints. Mesh densities are examined to ensure convergent results.

3.4.1 Validation

Numerical examples with different Young’s modulus ratios E_s/E_f and thickness ratios h_s/h_f are performed to validate the proposed macroscopic model. This first set of analyses is addressed as “problem I”. Table 3.1 presents the material properties and geometric parameters. E_s/E_f ranges from 10^{-5} to 10^{-3} representing typical

Table 3.1: Material and geometric parameters of the film/substrate, problem I.

E_f (10^4 MPa)	E_s/E_f	ν_s	L (10^{-1} m)	b (m)	h_f/L	h_s/h_f
6.9	$10^{-5} - 10^{-3}$	0.3	5.0	1.0	1/200	$10 - 10^3$

materials for stiff film layer resting on a compliant substrate Huang et al. (2005). The thickness ratio h_s/h_f varies between 10, for very thin substrates, and 10^3 for very thick substrates.

For the proposed macroscopic model, a mesh with 8 elements along the x direction and 40 elements in z direction in the substrate is used. This implies about $4.33 \cdot 10^3$ degrees of freedom (DOFs). Linear eigenvalue buckling analyses using function BUCKLE in the ABAQUS (Cao et al. (2012)) are performed to obtain the critical compressive load λ_c and the corresponding half-wave number q_0 of the considered film/substrate systems. Table 3.2 presents the results of the two parameters obtained by the macroscopic model I and 2D full model. Good results agreement is observed for all examples. This confirms the validation of the proposed macroscopic FE model in predicting the critical load and wavenumber in the film/substrate systems. From Table 3.2, one notices that the critical load and the wavenumber decrease as the substrate becomes thicker and softer. For a fixed E_s/E_f ratio, the results change very little when h_s/h_f varies from 10^2 to 10^3 , because only a limited

Table 3.2: Half-wave number q_0 and critical load parameter λ_c . “Present” stands for Fourier-series macroscopic model I and “ABAQUS” is 2D full model by ABAQUS. Problem I.

h_s/h_f	10			10^2			10^3		
	q_0	$10^{-4}\lambda_c$ (MPa)		q_0	$10^{-4}\lambda_c$ (MPa)		q_0	$10^{-4}\lambda_c$ (MPa)	
E_s/E_f		Present	ABAQUS		Present	ABAQUS		Present	ABAQUS
10^{-3}	12	143	143	9	108	109	9	111	109
10^{-4}	8	39.5	38.5	5	23.6	23.4	5	23.7	23.4
10^{-5}	4	12.8	12.8	2	5.91	5.85	2	5.82	5.76

part of the substrate near the interface contributes to the instability phenomenon while the remaining part far from the interface is unstrained. This is also evident from the wrinkling color map of a thin film resting on a very thick substrate in Fig. 3.4. These prominent features in the wrinkling phenomenon of a stiff film on an elastic compliant substrate are similar to that revealed by Huang et al. (2005) through analytical solutions and Yang et al. (2015) through numerical results with finite element method.

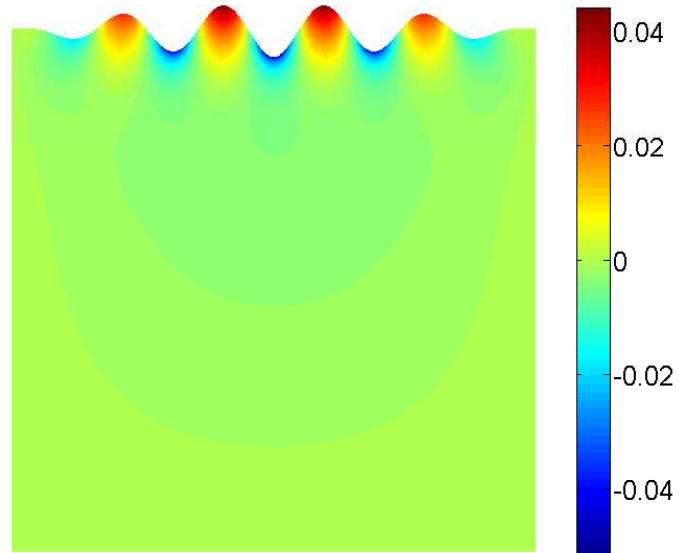
3.4.2 Convergence and computation cost

The model convergence is studied by varying the axial and through-the-thickness discretisation of the substrate. The same film/substrate material and geometrical parameters as in Yang et al. (2015) are considered and summarised in Table 3.3. The left and right edges of the film/substrate system are fixed. This set of analyses is addressed as “problem II”.

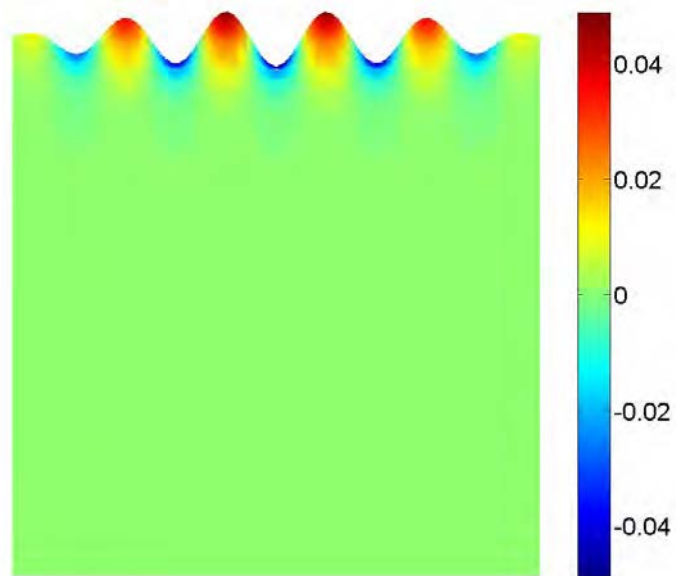
Table 3.3: Material and geometric parameters of the film/substrate, problem II.

E_f (10^5 MPa)	E_s/E_f	ν_s	L (10^{-3} m)	b (10^{-3} m)	h_f/L	h_s/h_f
1.8	10^{-5}	0.3	1.0	1.0	10^{-3}	10^3

Fig. 3.4 presents the instability pattern in the neighbourhood of the bifurcation point as a colour map. The macroscopic model correctly predicts the shape and the number of wrinkles. For the ABAQUS model, a mesh $N_{ex} \times N_{ez} = 80 \times 81$ with $3.95 \cdot 10^4$ DOFs is used to model the film/substrate structure. N_{ex} and N_{ez} represent the element number along the x - and z -directions, respectively. The non-linear post-buckling solution in the ABAQUS is performed by the Riks algorithm, where the eigenmode of interest scaled by a very small factor is introduced as



(a)



(b)

Figure 3.4: Transverse displacement $50 \cdot w$ (10^{-3} m) color map: (a) ABAQUS and (b) macroscopic model I, problem II.

the geometrical imperfection to initiate instability. In the macroscopic model I, a transverse perturbation force $10^{-5} \cdot F$ is applied at the point $x = L/2$ on the film to trigger the buckling. The non-linear calculation is piloted by setting $q_0 = 11$. The solution convergence is achieved by considering different meshes for the Fourier-series macroscopic model. The mesh details are presented in Table 3.4. The DOFs

	N_{ex}	N_{ez}	Elements number	DOFs
ABAQUS	80	81	6'480	39'525
Present, mesh 1	8	31	248	3'290
Present, mesh 2	8	41	328	4'330
Present, mesh 3	10	31	310	4'050

Table 3.4: Mesh details for problem II.

of the mesh scheme 1 (8×31 elements) are an order of magnitude lower than that of ABAQUS solution. Fig. 3.5 shows the bifurcation path of the transverse displacement at the point ($x = L/2, z = h_s + h_f/2$) versus the applied load for the macroscopic model I with three mesh schemes. The critical load obtained by all the considered mesh schemes converges to $\lambda_c = 0.0498$ MPa and agrees well with the reference solution by ABAQUS, which shows that the macroscopic model with mesh 1 is sufficient to accurately predict the buckling load of the considered film/substrate system. Besides, the responses in the post-buckling process also match fairly well. The proposed macroscopic model I is able to correctly describe the film/substrate wrinkling with reduced computational cost.

Here, we further compare the computation efforts of the Fourier-based macroscopic model and the ABAQUS model in the theoretical aspect. A qualitative analysis on the computing cost of the two models is conducted by building the relations between the element number and the geometrical and material parameters in the film/substrate system.

For the ABAQUS model, the element size l_e^f should be proportional to the wavelength of the wrinkles λ^* , i.e., $l_e^f \sim \lambda^*$, which means that a larger wavelength corresponds to a larger element size. For the film/substrate system with very thick substrate in the plane-strain case Huang et al. (2005); Mei et al. (2011), the wavelength can be scaled by

$$\lambda^* \sim h_f \left(\frac{\bar{E}_f}{\bar{E}_s} \right)^{1/3} \quad (3.54)$$

where $\bar{E} = E/(1 - \nu^2)$ is the plane-strain modulus. The element aspect ratio is assumed equal to one Yu et al. (2015). Then, the element number (approximate to

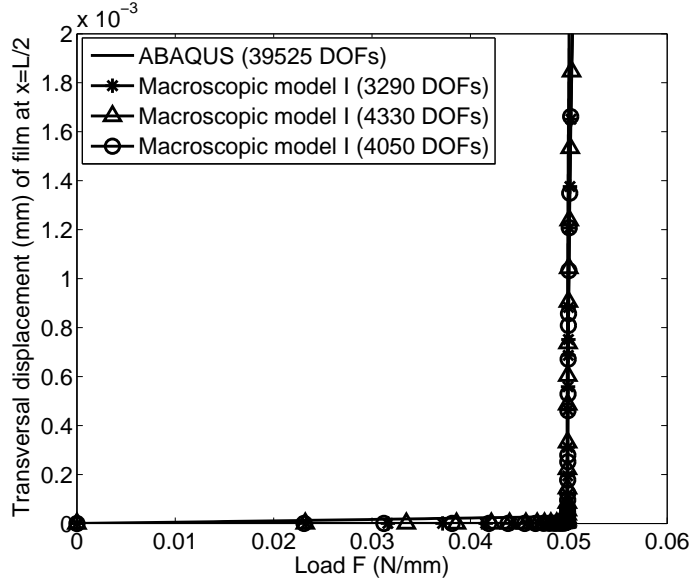


Figure 3.5: Bifurcation curves for ABAQUS solution and two-dimensional macroscopic model I with different meshes, problem II.

the node number) of the system can be expressed as

$$n_e^f = n_e^{fx} \cdot n_e^{fz} \sim \frac{L}{l_e^f} \cdot \frac{h_s}{l_e^f} \sim \frac{Lh_s}{(\lambda^*)^2} \quad (3.55)$$

where $n_e^{fx} \sim \frac{L}{l_e^f}$ and $n_e^{fz} \sim \frac{h_s}{l_e^f}$ are the element number in the x and z directions, respectively, and L is the total length of the system.

For the proposed macroscopic model, several elements are generally sufficient to well characterize the wrinkles in the x direction since only the slowly varying amplitude of the wrinkles needs to be simulated. Therefore, the element number in the x direction, n_e^{mx} , can be assumed as a constant independent on the geometrical and material parameters (Huang et al. (2015)). The most important factor to determine the problem size for the macroscopic model should be the vertical displacement in the substrate, \mathcal{W}^s , which shows a sharp but monotonic variation in the area near the film. According to our previous study (Yang et al. (2015)), the thickness of such an area with sharp-varying in \mathcal{W}^s is about λ^* . Therefore, the element size in the z direction can be scaled by $l_e^{mz} \sim \lambda^*$ and corresponding element number satisfies $n_e^{mz} \sim h_s/\lambda^*$. Following the above definitions, the total element number follows

$$n_e^m = n_e^{mx} \cdot n_e^{mz} \sim \frac{h_s}{\lambda^*} \quad (3.56)$$

Let n_e^f and n_e^m be the approximations of the computation cost for the two modeling methods. Then, the ratio of computation cost should satisfy

$$r = \frac{n_e^f}{n_e^m} \sim \frac{L}{\lambda^*} \sim \frac{L}{h_f} \left(\frac{\bar{E}_s}{\bar{E}_f} \right)^{1/3} \quad (3.57)$$

We can easily find that for a larger slenderness ratio $\frac{L}{h_f}$ or modulus ratio $\frac{\bar{E}_s}{\bar{E}_f}$, the macroscopic model will show better computation performance than the ABAQUS model.

3.4.3 Discussions on Fourier-based approach and oscillation locking

3.4.3.1 The first harmonic of Fourier series

The Fourier-based approach recently has been efficiently used in analysing instabilities with spatially periodic patterns in thin structures such as the beam on Winkler's foundation (Damil and Potier-Ferry (2010); Mhada et al. (2012)) and the thin metal sheet (Damil et al. (2013, 2014); Huang et al. (2015); Attipou et al. (2015)). In these structures, the Fourier-based models are usually discretized with structural elements, i.e., beam element and plate element, in which the neutral axial displacements are always assumed not to fluctuate along the x direction within the Fourier series approach, i.e., $u^f = u_0^f$ (see Eq. (3.17)). The assumption is valid for these structural elements since the fluctuation in the area such as the bottom or top face of these structures can be described by the derivatives of deflection \mathcal{W}^f (see Eq. (3.21)). Thus, in the Fourier-series expansion of the neutral axial displacement, the first harmonic representing the fluctuation is overlooked in these Fourier-based models.

However, for the film/substrate system that is composed of two kinds of elements (structural elements in the film and continuum elements in the substrate), it is necessary to take account for the first harmonic of the axial displacement in the substrate. Due to the compatibility of axial displacements at the film/substrate interface, when wrinkles occur in the film/substrate system, the oscillating bottom face of the film induces the occurrence of oscillation in the substrate. However, the zero harmonic \mathcal{U}_0^s representing the mean field of the axial displacement can not approximate this oscillation, thus the first harmonic \mathcal{U}_1^s should be taken into account, see Fig. 3.6. The reasonableness of introducing the first harmonic has been verified through comparative analysis in terms of the critical load and wrinkling

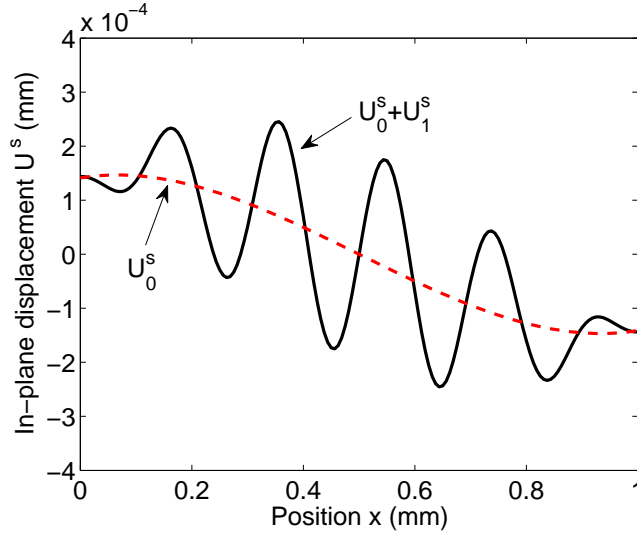


Figure 3.6: Axial displacement distribution along x at $z = 0.95$ mm after bifurcation point in the substrate. Problem II.

wavenumber in several numerical tests. The macroscopic model I in Section 4.2 and 4.3 takes into account the first harmonics and accurate results are obtained. If the first harmonic is not considered in the substrate, in another word, the same assumption as made in the previous Fourier-based beam and plate models is used, i.e., $\mathcal{U}^s = \mathcal{U}_0^s$, the axial displacement continuity at the interface is then not satisfied: the axial displacement of the film's bottom face fluctuates, while the substrate does not. Therefore, the substrate becomes stiffer than actually it is and a higher external load is needed to trigger the buckling. In Fig. 3.7, the critical load predicted by the macroscopic model II is about 12% higher than that obtained by the macroscopic model I or 2D full model. The macroscopic model II is the macroscopic model that considers only the mean field \mathcal{U}_0^s of axial displacement and uses plane-strain constitutive law in the substrate. This further certifies the importance of the first harmonic in approximating the axial displacement in the continuum element.

3.4.3.2 Oscillation locking

The previously mentioned over-stiffening behavior can be found in locking phenomena such as the membrane locking (Reddy (2004a)) or the Poisson thickness locking (Carrera and Brischetto (2008a,b)). The occurrence of these phenomena are related to the assumed computational approximations. For example, the Poisson thickness locking is caused by the over-simplified kinematic assumption in plate or shell analysis. In this Chapter, the over-stiffening phenomenon in the substrate

leading to higher critical load is also caused by an over-simplification of the kinematics. Within the Fourier-series approach, we name this kind of phenomenon as “oscillation locking”.

To avoid the oscillation locking, one can use higher order functions, i.e., the first harmonic of the axial displacement in the substrate $\mathcal{U}^s = \mathcal{U}_0^s + \mathcal{U}_1^s e^{iqx} + \mathcal{U}_{-1}^s e^{-iqx}$. This is the way to derive the macroscopic model I in Section 3 and the accuracy of this model has been validated in Section 4.1 and 4.2. In addition, we also found an effective way to alleviate the locking problem by modifying the elastic coefficient of the substrate when only the mean field of axial displacement is considered in the substrate. This manner is similar to the way dealing with thickness locking in Carrera and Brischetto (2008a,b). A detailed discussion on the alleviation of oscillation locking is presented below.

In the substrate, according to the assumption $\mathcal{U}^s = \mathcal{U}_0^s$, the axial displacement shows no fluctuation and varies almost linearly (see the dotted line in Fig. 3.6, thus the axial strain ϵ_{xx} should be almost a constant. In the plane-strain constitutive relation of the substrate, the axial strain ϵ_{xx} has a contribution (ϵ_{xx}^ν) due to the Poisson effect

$$\epsilon_{xx}^\nu \propto \nu \epsilon_{zz} \quad (3.58)$$

Rapid fluctuation of the transverse normal strain ϵ_{zz} along the x -direction causes the related ϵ_{xx}^ν to rapidly oscillate. This is in contradiction with the kinematic assumption of the macroscopic model, i.e., ϵ_{xx} is constant. Similar to the second remedy in treating the thickness locking in Carrera and Brischetto (2008a), we modify the elastic coefficient by forcing the axial strain ϵ_{xx} to meet the kinematic assumption of the macroscopic model. Thus, the rapid fluctuating axial strain ϵ_{xx}^ν should be eliminated, which is achieved by setting a nil Poisson ratio in the substrate. The modified elastic coefficients become

$$\begin{aligned} C_{11}^s &= C_{33}^s = E_s \\ C_{13}^s &= 0 \\ C_{55}^s &= G \end{aligned} \quad (3.59)$$

where G is the shear modulus: $G = E_s/2(1 + \nu_s)$. It leads to a reduction in the elastic coefficients and thus reduces the stiffness of the substrate. The macroscopic model with only \mathcal{U}_0^s for the in-plane axial displacement and the modified elastic coefficient is referred as “macroscopic model III” in the following.

The critical load and the half-wave number obtained by the macroscopic model III are presented in Table 3.5 for problem I. Good result agreement is observed com-

pared with the reference solutions in Table 3.2. The bifurcation curves for different

Table 3.5: Half-wave number q_0 and critical load parameter λ_c for problem I via the macroscopic model III with elastic coefficient correction. Reference ABAQUS results are presented in Table 3.2.

$\frac{h_s}{h_f}$	10		10^2		10^3	
$\frac{E_s}{E_f}$	q_0	$10^{-4}\lambda_c$ (MPa)	q_0	$10^{-4}\lambda_c$ (MPa)	q_0	$10^{-4}\lambda_c$ (MPa)
10^{-3}	12	140	9	110	9	111
10^{-4}	8	37.8	5	24.0	5	24.0
10^{-5}	4	11.7	2	5.94	2	5.86

models in the problem II are plotted in Fig. 3.7. The critical load predicted by the

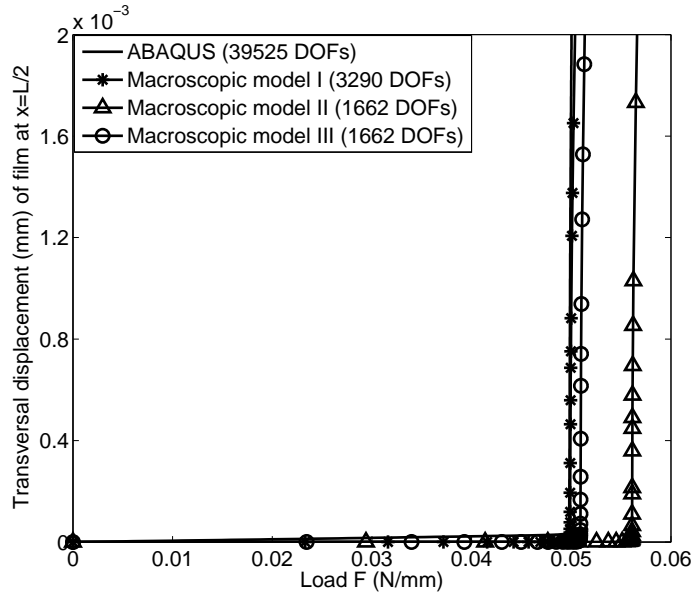


Figure 3.7: Bifurcation curves, problem II, three different kinds of macroscopic model and mesh 1.

two-dimensional macroscopic model III is fairly close to the reference. Compared with the macroscopic model II, the oscillation locking is obviously alleviated in the macroscopic model III, showing that the reduction of elastic coefficient is also an effective approach. Besides, the degrees of freedom of this solution (1662 DOFs) are almost half of those in the two-dimensional macroscopic model I with a first harmonic term in the axial displacement of the substrate (3290 DOFs). Compared to the first remedy (using higher order approximation functions), this method can save

considerable computational cost (the model has less unknowns to be determined).

3.5 Conclusion

A two-dimensional Fourier-based finite element model has been introduced to study the wrinkling in thin stiff films on compliant substrates. The proposed model is able to accurately and quickly characterize the wrinkling phenomena in film/substrate systems with only several elements in the wrinkle direction. Unlike the 2D full model, the size of the elements in the wrinkle direction is independent on the wrinkling wavelength. Numerical examples have been performed to validate and assess the proposed model by determining the critical wrinkling loads and half-wave number. Results prove that the Fourier-series model yields solutions very close to the reference ABAQUS ones at a reduced computational cost. Introducing the first harmonic of the Fourier series expansion of axial displacement in continuum element has been proved to be important in approximating the actual kinematical in substrate. Furthermore, a spurious over-stiffening phenomenon named as "oscillation locking" is pointed out within the Fourier series approach, which is caused by an over-simplification of actual kinematics, i.e., the elimination of the first harmonic. Two methods are proposed to avoid the locking effect. The first one stems from a physical consideration and consists in introducing the first harmonic of in-plane displacement in the substrate. The second one is to modify the elastic coefficient of the substrate so as to eliminate the oscillating axial strain originating from Poisson effect and match with the kinematic assumption in Fourier-series approach. The latter is recommended as far as the computational costs are concerned. As a final remark, it is well known that, as any reduced model, the proposed model may be not accurate near the boundary. A possible solution could be the use of a multi-scale model where a full model is considered close to the boundary and the Fourier-series model in the bulk, see Hu et al. (2011). The two models are bridged by the Arlequin method (Hu et al. (2011, 2010); Ben Dhia and Rateau (2005); Hu et al. (2009b)). This approach proves to be accurate yet computationally efficient to study the instabilities in sandwich structures, see Yu et al. (2013).

1D Fourier model for film/substrate instability

Contents

4.1 Introduction	62
4.2 Microscopic model	64
4.2.1 Kinematics	64
4.2.2 Geometric equation and constitutive law	67
4.3 Macroscopic model	68
4.3.1 General macroscopic formulation	68
4.3.2 Discretization	79
4.4 Numerical results	81
4.4.1 Validation	81
4.4.2 Mesh convergence	83
4.4.3 Fourier coefficient study	84
4.5 Conclusion	89

Abstract

In this Chapter, a new Fourier-related double scale approach is presented to study the wrinkling of thin films on compliant substrates. By using the method of Fourier series with slowly variable coefficients, the 1D microscopic model proposed by Yang et al. (2015) is transformed into a 1D macroscopic film/substrate model whose mesh size is independent on the wrinkling wavelength. Numerical tests prove that the new model improves computational efficiency significantly with accurate results, especially when dealing with wrinkling phenomena with vast wavenumbers. Besides, we propose a strategy to efficiently trace the wrinkling pattern corresponding to the lowest critical load by accounting for several harmonics of Fourier series in this new model. The established nonlinear system is solved by the Asymptotic Numerical Method (ANM), which has advantages of efficiency and reliability for stability

analyses.

Present Chapter corresponds to the published research paper (Huang et al., 2017) [Composite Structures, 160: 613-624, 2017.]. A self-consistent notation is adopted.

Keywords: Fourier series, CUF, Film/substrate, Wrinkling, Asymptotic Numerical Method

4.1 Introduction

System of a stiff layer resting on soft substrate exists widely in nature (human skin (Cerda and Mahadevan (2003))) and engineering fields (intelligent materials, biomedical field (Li et al. (2011))). When subjected to in-plane compression or exposed to the reduction of temperature field (Bowden et al. (1998)), the mismatch of mechanical properties or coefficients of thermal expansion of layers may lead to wrinkles. The wrinkles may pose a limit on the performance of materials or structures (Allen (1969)) and are always thought to be avoided, but nowadays may find some applications such as assembly of materials (Li et al. (2012)), measuring the mechanical properties of materials in modern metrology (Stafford et al. (2004)). For these reasons, it is quite necessary to characterize the wrinkling of the system in an accurate and efficient way.

As early as forty years ago, the stability analysis of multi-layered materials was investigated by Allen (1969) in the framework of sandwich panel designs in airplanes. From then on, much of theoretical work on substrate-bonded films has been proposed on the basis of linear perturbation analysis (see Niu and Talreja (1999)), which focused on determining the critical membrane force and wavelength of wrinkles. Recently, some nonlinear analyses were performed to further investigate and comprehend wrinkle characteristics in film/substrate systems. Using energy calculation, Chen and Hutchinson (2004) showed that the herringbone mode constitutes a minimum energy configuration among computed modes for a film under equal biaxial compression. Huang et al. (2004) modeled the substrate as an array of spring dashpots and developed a spectral method to inspect the evolution of wrinkling configurations, whose results showed that the anisotropy of the film forces affects the evolution of wrinkling patterns. As an extension work, Huang et al. (2005) extended their original spring model to a model representing the substrate by three-dimensional elastic field and investigated the influence of the Young's modulus, the thickness of substrate on the amplitude and wavelength of the sinusoidal

wrinkles. Through experiments and analytical solutions, Jiang et al. (2008) found the width effect on wrinkles of film/substrate that the amplitude and wavelength of wrinkles increase with the film width. Unlike the results obtained by the small deformation theory (Chen and Hutchinson (2004); Huang et al. (2005, 2004); Jiang et al. (2008)), Song et al. (2008) considered finite strain and nonlinear constitutive law in the substrate, and found that the buckling wavelength does not keep constant as in Chen and Hutchinson (2004); Huang et al. (2005, 2004) but relates to the large prestrain. To model the film/substrate system more efficiently, Yang et al. (2015) proposed a high order model based on the concept of the Carrera's Unified Formulation (CUF) (Carrera (2003a); He et al. (2011)), and results verified that the CUF model yielded accurate results with low computational cost. Similar methods based on such enriched kinematical functions have been widely used in the mechanical analysis of composite plates (Reddy (1984); Vidal and Polit (2008); Polit and Touratier (2000); Ferreira et al. (2011)).

In the above film/substrate systems, instability patterns are usually nearly periodic in spatial. Based on an efficient multi-scale approach established by Damil and Potier-Ferry (2010, 2008) that exploits such periodic nature and the effective CUF model of Yang et al. (2015), a Fourier-related one-dimensional model is developed to study the wrinkling phenomena in thin stiff films on compliant substrates. In the framework of the multi-scale approach (often referred to as "Fourier series with slowly varying coefficients"), the unknowns to be solved in Yang et al. (2015) are expanded by the Fourier series, which leads to the Fourier coefficients as the new unknowns varying much more slowly than the former unknowns (we address the former unknowns as "microscopic" and the latter "macroscopic" in this Chapter). Usually using rather coarse spatial meshes is sufficient to describe the slowly varying envelopes, therefore computational efficiency can be improved significantly (Damil and Potier-Ferry (2010); Liu et al. (2012); Huang et al. (2015)). This approach is firstly applied to study the instability phenomena in beams on Winkler foundation (Damil and Potier-Ferry (2010, 2008)) with a most simplified macroscopic model, in which only the zero harmonic (mean field) and the first order harmonics (envelops) are taken into account. Results showed that the macroscopic model has two advantages compared to the Landau-Ginzburg technique: 1) not only the bifurcation point but also the post-buckling path can be captured and 2) the coupled global and local instability patterns can be incorporated and characterised, see Liu et al. (2012). In this Chapter, a similar most simplified macroscopic model is firstly presented to investigate the instability of the film/substrate structures. As like any reduced models, the Fourier models may loss some accuracy in the vicinity of

boundary. To handle this issue, Mhada et al. (2012) took into account phase change in macroscopic model, and Hu et al. (2011) proposed to establish multi-scale model containing microscopic model near the boundary and macroscopic model in the bulk, the two models were bridged by the Arlequin method (Ben Dhia and Rateau (2005)). Results showed that the multi-scale model treats boundary conditions better. For the above Fourier models, only two harmonics (the first order envelopes and the mean field) were taken into account, thus the wrinkling wavelength or wavenumber should be a prior set variable, which may lead to some inconvenience by trying different wavelengths or wavenumbers to find the lowest critical buckling load. In this Chapter, we propose another strategy to trace the lowest critical load by deriving a macroscopic model considering several harmonics of the Fourier series. Results show that, independent on the preset wavelength, the macroscopic model can automatically trace the lowest wrinkling critical load. The established nonlinear system for the instability problems of the film/substrate structures shows strong nonlinearity with bifurcation branches, therefore it is difficult to trace the so-called equilibrium path. Two kinds of widely used methods to solve these nonlinear problems can be the classical predictor-corrector methods (e.g. the Newton-Raphson method and the arc-length method) and the perturbation methods (H. S. Shen (2013)). By coupling the perturbation method with numerical method, Damil and Potier-Ferry (1990); Cochelin et al. (2007, 1994) proposed an attractive nonlinear solver known as the Asymptotic Numerical Method (ANM), which is effective and robust especially in tracing bifurcation path in instability problems. In this Chapter, the ANM is used to solve the established nonlinear equations.

This Chapter is structured as follows. The 1D microscopic model for film/substrate system is reviewed in Section 4.2. In Section 4.3, the macroscopic model is deduced by the Fourier series, and the nonlinear equations are solved by the Asymptotic Numerical Method. In Section 4.4, numerical tests have been carefully investigated to valid the established macroscopic model.

4.2 Microscopic model

4.2.1 Kinematics

We consider a two-dimensional elastic stiff film resting on an elastic soft compliant substrate, as depicted in Fig. 4.1. Let x and z be the longitudinal and the transverse coordinates, L and b are the length and the width of the structure, respectively. The thickness of the top film and substrate are, respectively, h_f and h_s . The substrate

is ideally divided into a core and a bottom layer of thickness h_c and h_b as in Yang et al. (2015). This division allows to describe the rapid displacement variation along the z direction close to the thin film by high-order kinematic theories and slowly varying kinematics far away from the top film by low-order polynomials, so that less variables are needed to accurately describe the displacement field in the film/substrate structure.

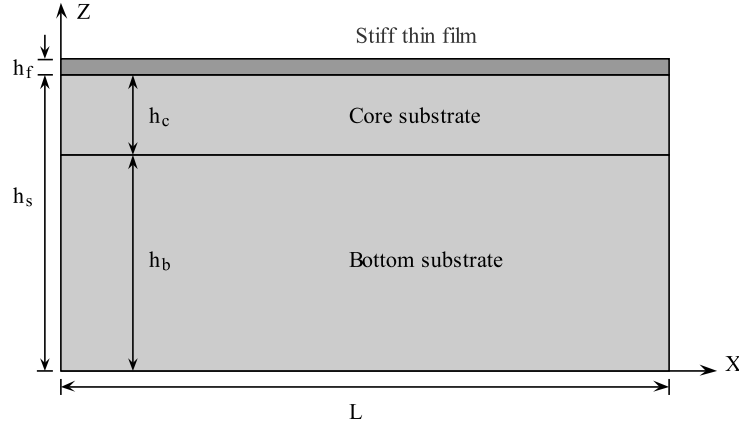


Figure 4.1: Sketch of an elastic thin stiff film on a compliant substrate

As the same kinematic proposed in Yang et al. (2015), the thin film is modeled as the Euler-Bernoulli's beam:

$$\begin{aligned} \text{Film: } \mathcal{U}^f(x, z) &= u_0^f(x) - \left(z - \frac{h_f + 2h_s}{2}\right) \mathcal{W}_{,x}^f(x, z) & z \in [h_s, h_s + h_f] \\ \mathcal{W}^f(x, z) &= w^f(x) \end{aligned} \quad (4.1)$$

where the superscript “ f ” stands for the film, the notation “ x ” stands for $\frac{\partial}{\partial x}$, $\mathcal{U}(x, z)$ and $\mathcal{W}(x, z)$ represent the displacements along the x - and z -axis, respectively. The two unknown functions u_0^f and w^f are the components of the displacements of the mid-plane of the film. The substrate is modeled as a plane-strain elastic solid:

$$\begin{aligned} \text{Core: } \mathcal{U}^c(x, z) &= F_\tau(z) u_\tau^c(x) \\ \mathcal{W}^c(x, z) &= F_\tau(z) w_\tau^c(x) \end{aligned} \quad z \in [h_b, h_s] \quad \tau \in [0, n_c] \quad (4.2)$$

$$\begin{aligned} \text{Bottom: } \mathcal{U}^b(x, z) &= F_\tau(z) u_\tau^b(x) \\ \mathcal{W}^b(x, z) &= F_\tau(z) w_\tau^b(x) \end{aligned} \quad z \in [0, h_b] \quad \tau \in [0, n_b] \quad (4.3)$$

where superscripts “ c ” and “ b ” stand for the core and bottom layer of substrate, re-

spectively. The notation $F_\tau(z)$ represents the through-the-thickness approximating function within CUF framework, which generally can be an element of a generic approximation base. Within this work, the Mac Laurin's polynomials z^n are adopted as expansion function. The notations u_τ and w_τ are the unknown displacement functions along the beam axis. According to the Einstein rule, repeated indexes denote summation, thus $\mathcal{U}^c(x, z)$, as an example, can be explicitly written as:

$$\mathcal{U}^c(x, z) = u_0^c + zu_1^c + z^2u_2^c + \cdots + z^nu_n^c \quad n \in \mathbb{N} \quad (4.4)$$

As a result, a family of one-dimensional refined beam models can be systematically obtained considering the expansion function order as a free parameter of the formulation, that is, n can be an arbitrary value. In this film/substrate system, the variable n is valued as n_c and n_b for the core and bottom layer of substrate, respectively.

The continuity of the displacement field between the layers film/core and core/bottom is ensured by

$$\begin{aligned} \mathcal{U}^f(x, h_s) &= \mathcal{U}^c(x, h_s) \\ \mathcal{W}^f(x, h_s) &= \mathcal{W}^c(x, h_s) \\ \mathcal{U}^c(x, h_b) &= \mathcal{U}^b(x, h_b) \\ \mathcal{W}^c(x, h_b) &= \mathcal{W}^b(x, h_b) \end{aligned} \quad (4.5)$$

For the interface of the film and the core substrate, the displacement continuity is ensured by substituting Eqs. (4.1) and (4.2) into Eq. (4.5):

$$\begin{aligned} u_0^c &= u_0^f + \frac{1}{2}h_f w_{,x}^f - \bar{F}_i u_i^c \\ w_0^c &= w^f - \bar{F}_i w_i^c \end{aligned} \quad i \in [1, n_c] \quad (4.6)$$

where $\bar{F}_i = h_s^i$. Then Eq. (4.2) can be rewritten as:

$$\begin{aligned} \mathcal{U}^c &= u_0^f + \frac{1}{2}h_f w_{,x}^f + (F_i - \bar{F}_i)u_i^c \\ \mathcal{W}^c &= w^f + (F_i - \bar{F}_i)w_i^c \end{aligned} \quad z \in [h_b, h_s] \quad i \in [1, n_c] \quad (4.7)$$

The congruency of the displacement field at the interface $\Gamma = \{(x, y, z) : x \in [0, L], y \in [-b/2, b/2], z = h_b\}$ of the core and bottom layers is ensured via the Constrained Variational Principle (CVP). By introducing the Lagrange multipliers $\boldsymbol{\mu} = \langle \mu_1, \mu_2 \rangle$ as fictitious gluing forces, it results in the constrain term $\mathcal{L}(\boldsymbol{\mu}, \mathbf{u})$:

$$\mathcal{L}(\boldsymbol{\mu}, \mathbf{u}) = \int_{\Gamma} \mu_1 \left[\mathcal{U}^c(x, h_b) - \mathcal{U}^b(x, h_b) \right] + \mu_2 \left[\mathcal{W}^c(x, h_b) - \mathcal{W}^b(x, h_b) \right] d\Gamma \quad (4.8)$$

4.2.2 Geometric equation and constitutive law

The geometric equation and constitute law meet the following assumptions:

1. the material behavior is linearly elastic and meets the Hooke's law,
2. the Green-Lagrange strain is used to describe the relationships between strain and displacement in the film,
3. the small displacement with moderate rotation is assumed for the film and the substrate small displacement.

The above assumptions are given by the following equations:

$$\begin{aligned}
\sigma_{xx}^f &= E_f \epsilon_{xx}^f = E_f \left(\mathcal{U}_{,x}^f + \frac{1}{2} (\mathcal{W}_{,x}^f)^2 \right) \\
\sigma_{xx}^s &= C_{11}^s \epsilon_{xx}^s + C_{13}^s \epsilon_{zz}^s = C_{11}^s \mathcal{U}_{,x}^s + C_{13}^s \mathcal{W}_{,z}^s \\
\sigma_{zz}^s &= C_{13}^s \epsilon_{xx}^s + C_{33}^s \epsilon_{zz}^s = C_{13}^s \mathcal{U}_{,x}^s + C_{33}^s \mathcal{W}_{,z}^s \\
\sigma_{xz}^s &= 2C_{55}^s \epsilon_{xz}^s = C_{55}^s (\mathcal{U}_{,z}^s + \mathcal{W}_{,x}^s)
\end{aligned} \tag{4.9}$$

with

$$\begin{aligned}
C_{11}^s &= C_{33}^s = \frac{1 - \nu_s}{(1 + \nu_s)(1 - 2\nu_s)} E_s \\
C_{13}^s &= \frac{\nu_s}{(1 + \nu_s)(1 - 2\nu_s)} E_s \\
C_{55}^s &= \frac{E_s}{2(1 + \nu_s)}
\end{aligned} \tag{4.10}$$

where E_f is the Young's modulus of the film, E_s and ν_s are the Young's modulus and Poisson's ratio of the substrate. The subscript "s" represents "c" or "b" for the core or bottom layer of substrate for brevity.

Considering the constrained variational problem, the weak form of the governing equations are obtained by using the Principal of Virtual Displacement as follows:

$$\delta \mathcal{P}_{int} + \delta \mathcal{L} = \delta \mathcal{P}_{ext} \tag{4.11}$$

where $\delta \mathcal{P}_{int}$ is the virtual internal work and $\delta \mathcal{P}_{ext}$ the virtual external work. The internal virtual work of the film/substrate system is expressed as:

$$\begin{aligned}
\delta \mathcal{P}_{int} &= \int_{V^f} \sigma_{xx}^f \delta \epsilon_{xx}^f dV^f + \int_{V^c} (\sigma_{xx}^c \delta \epsilon_{xx}^c + \sigma_{zz}^c \delta \epsilon_{zz}^c + 2\sigma_{xz}^c \delta \epsilon_{xz}^c) dV^c \\
&\quad + \int_{V^b} (\sigma_{xx}^b \delta \epsilon_{xx}^b + \sigma_{zz}^b \delta \epsilon_{zz}^b + 2\sigma_{xz}^b \delta \epsilon_{xz}^b) dV^b
\end{aligned} \tag{4.12}$$

where V^f , V^c and V^b express the integration volumes of the film, core and bottom substrates, respectively. By using Eqs. (4.1-4.3) and substituting Eqs. (4.6-4.10)

into Eq. (4.12), a 1D microscopical model could be deduced, see more details in Yang et al. (2015). In the next part, the technique of slowly varying Fourier coefficient is applied to the above equations to derive the one-dimensional macroscopical model.

4.3 Macroscopic model

In this part, the macroscopic film/substrate model will be presented based on the concept of Fourier series with slowly varying coefficients. The principle of the Fourier-related approach is to write the unknown field in the following form:

$$\mathbf{U}(x, z) = \sum_{j=-\infty}^{+\infty} \mathbf{U}_j(x, z) e^{ijqx} \quad (4.13)$$

where the Fourier coefficient $\mathbf{U}_j(x, z)$ denotes the envelope for the j th order harmonic, which is conjugated with $\mathbf{U}_{-j}(x, z)$. For simplicity, the macroscopic unknown field $\mathbf{U}_j(x, z)$ is assumed to slowly vary in a single direction over a period $\left[x, x + \frac{2\pi}{q} \right]$ of the oscillation. The wavenumber q is defined as

$$q = \frac{\pi}{L} q_0 \quad (4.14)$$

in which, L is the length of film/substrate and q_0 is a chosen integer wave-parameter: $q_0 \in \mathbb{N}$ and $q_0 \geq 2$. In practice, the number of Fourier coefficients considered is finite. But at least two functions $\mathbf{U}_0(x, z)$ and $\mathbf{U}_1(x, z)$ are needed to describe nearly periodic patterns: $\mathbf{U}_0(x, z)$ can be identified to the mean value while $\mathbf{U}_1(x, z)$ represents the envelope or the amplitude of the spatial oscillations, see Fig. 4.2. These two harmonics of the Fourier series have been used to describe instability phenomena in beams on Winkler's foundation (Damil and Potier-Ferry (2010)), sandwich beams (Yu et al. (2013); Mhada et al. (2013)) and thin metal films (Damil et al. (2013, 2014); Huang et al. (2015)), and rather good estimations in wrinkling pattern and critical load have been observed.

4.3.1 General macroscopic formulation

To establish the macroscopic equations satisfied by the envelopes \mathbf{U}_j , we firstly introduce some rules proposed by Damil and Potier-Ferry (2010). If $a(x)$ and $b(x)$ are Fourier series with slowly varying coefficients as in Eq. (4.13), the following

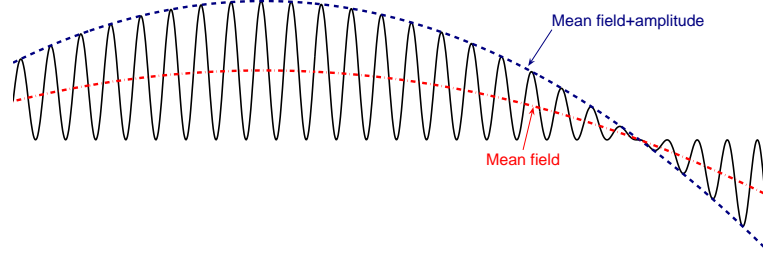


Figure 4.2: At least two macroscopic fields are necessary to describe a nearly periodic response: the mean field and the amplitude of the fluctuation.

identities hold:

$$\int_0^l a(x)b(x)dx = \int_0^l \sum_{j=-\infty}^{\infty} a_j(x)b_{-j}(x)dx \quad (4.15)$$

$$\left(\frac{da}{dx}\right)_j = (a')_j = \left(\frac{d}{dx} + \mathbf{i}jq\right)a_j = (a_j)' + \mathbf{i}jq a_j \quad (4.16)$$

$$\left(\frac{d^2a}{dx^2}\right)_j = (a'')_j = \left(\frac{d}{dx} + \mathbf{i}jq\right)^2 a_j = (a_j)'' + 2\mathbf{i}jq(a_j)' - j^2 q^2 a_j \quad (4.17)$$

$$(ab)_j = \sum_{j_1=-\infty}^{+\infty} a_{j_1} b_{j-j_1} \quad (4.18)$$

Using the above identities, the macroscopical version of the displacement fields in Eqs. (4.1-4.3) are expressed as

$$\mathcal{U}_j^f(x, z) = (u_0^f)_j - \left(z - \frac{h_f + 2h_s}{2}\right) \left(\frac{d}{dx} + \mathbf{i}jq\right) \mathcal{W}_j^f \quad z \in [h_s, h_s + h_f] \quad (4.19)$$

$$\mathcal{W}_j^f(x, z) = w_j^f$$

$$\begin{aligned} \mathcal{U}_j^c(x, z) &= F_\tau (u_\tau^c)_j \\ \mathcal{W}_j^c(x, z) &= F_\tau (w_\tau^c)_j \end{aligned} \quad z \in [h_b, h_s] \quad \tau \in [0, n_c] \quad (4.20)$$

$$\begin{aligned} \mathcal{U}_j^b(x, z) &= F_\tau (u_\tau^b)_j \\ \mathcal{W}_j^b(x, z) &= F_\tau (w_\tau^b)_j \end{aligned} \quad z \in [0, h_b] \quad \tau \in [0, n_b] \quad (4.21)$$

and the macroscopic form of Eq. (4.7) could be written as

$$\begin{aligned} \mathcal{U}_j^c &= (u_0^f)_j + \frac{1}{2} h_f \left(\frac{d}{dx} + \mathbf{i}jq\right) w_j^f + (F_i - \bar{F}_i)(u_i^c)_j \\ \mathcal{W}_j^c &= w_j^f + (F_i - \bar{F}_i)(w_i^c)_j \end{aligned} \quad (4.22)$$

The macroscopic constitutive laws are thus as follows:

$$\begin{aligned}
(\sigma_{xx}^f)_j &= E_f (\epsilon_{xx}^f)_j = E_f \left(\left(\frac{d}{dx} + \mathbf{i}jq \right) \mathcal{W}_j^f + \frac{1}{2} \sum_{j_1=-\infty}^{+\infty} \left(\frac{d}{dx} + \mathbf{i}j_1q \right) \left(\frac{d}{dx} + \mathbf{i}(j-j_1)q \right) \mathcal{W}_{j_1}^f \mathcal{W}_{j-j_1}^f \right) \\
(\sigma_{xx}^s)_j &= (C_{11}\epsilon_{xx}^s + C_{13}\epsilon_{zz}^s)_j = C_{11} \left(\frac{d}{dx} + \mathbf{i}jq \right) \mathcal{W}_j^s + C_{13} \mathcal{W}_{j,z}^s \\
(\sigma_{zz}^s)_j &= (C_{13}\epsilon_{xx}^s + C_{33}\epsilon_{zz}^s)_j = C_{13} \left(\frac{d}{dx} + \mathbf{i}jq \right) \mathcal{W}_j^s + C_{33} \mathcal{W}_{j,z}^s \\
(\sigma_{xz}^s)_j &= 2C_{55} (\epsilon_{xz}^s)_j = C_{55} \left(\mathcal{W}_{j,z}^s + \left(\frac{d}{dx} + \mathbf{i}jq \right) \mathcal{W}_j^s \right)
\end{aligned} \tag{4.23}$$

After substituting Eq. (4.23) into Eq. (4.12), the macroscopic version of the internal virtual work is:

$$\begin{aligned}
\delta \mathcal{P}_{int} &= \int_{V^f} \sum_{j=-n_j}^{+n_j} (\sigma_{xx}^f)_j \delta(\epsilon_{xx}^f)_{-j} dV^f \\
&\quad \int_{V^c} \sum_{j=-n_j}^{+n_j} \left((\sigma_{xx}^c)_j \delta(\epsilon_{xx}^c)_{-j} + (\sigma_{zz}^c)_j \delta(\epsilon_{zz}^c)_{-j} + 2(\sigma_{xz}^c)_j \delta(\epsilon_{xz}^c)_{-j} \right) dV^c \tag{4.24} \\
&\quad \int_{V^b} \sum_{j=-n_j}^{+n_j} \left((\sigma_{xx}^b)_j \delta(\epsilon_{xx}^b)_{-j} + (\sigma_{zz}^b)_j \delta(\epsilon_{zz}^b)_{-j} + 2(\sigma_{xz}^b)_j \delta(\epsilon_{xz}^b)_{-j} \right) dV^b
\end{aligned}$$

where n_j is the number of Fourier coefficients. In the following, before the finite element computational scheme is established, some assumptions are introduced according to Damil and Potier-Ferry (2010): u_0^f , u_τ^c , u_τ^b do not fluctuate, i.e $u_0^f \stackrel{def}{=} (u_0^f)_0$, $u_\tau^c \stackrel{def}{=} (u_\tau^c)_0$, $u_\tau^b \stackrel{def}{=} (u_\tau^b)_0$.

4.3.1.1 Internal virtual work of the film

As the thin film is modeled as the nonlinear beam, the virtual work of the film could be expressed as:

$$\delta \mathcal{P}_{int}^f = \int_{V^f} \sigma_{xx}^f \delta \epsilon_{xx}^f dV^f = \int_0^L N^f \delta \gamma + M^f \delta w_{,xx} dx \tag{4.25}$$

in which

$$\gamma = u_{0,x}^f + \frac{1}{2} w_{,x}^f{}^2 \quad N^f = E_f b h_f \gamma \quad M^f = E_f I_f w_{,xx}^f \quad I_f = 1/12 b h_f^3 \tag{4.26}$$

The macroscopic version of internal virtual work of the film in Eq. (4.25) could be rewritten as:

$$\delta \mathcal{P}_{int}^f = \int_{V^f} \sum_{j=-n_j}^{+n_j} (\sigma_{xx}^f)_j \delta(\epsilon_{xx}^f)_{-j} dV^f = \int_0^L \sum_{j=-n_j}^{+n_j} (N_j^f \delta\gamma_{-j} + M_j^f \delta(w_{,xx}^f)_{-j}) dx \quad (4.27)$$

With the assumption that the axial force $N^f(x)$ does not fluctuate Damil and Potier-Ferry (2010): $N^f(x) = N_0^f(x)$, $\gamma(x) = \gamma_0(x)$, Eq. (5.42) can be simplified as:

$$\delta \mathcal{P}_{int}^f = \int_0^L N_0^f \delta\gamma_0 + \sum_{j=-n_j}^{+n_j} M_j^f \delta(w_{,xx}^f)_{-j} dx \quad (4.28)$$

where

$$\begin{aligned} N_0^f &= E_f b h_f \left(u_{0,x}^f + \frac{1}{2} \sum_{j=-n_j}^{+n_j} \left(\frac{d}{dx} + \mathbf{i}jq \right) \left(\frac{d}{dx} - \mathbf{i}jq \right) w_j^f w_{-j}^f \right) \\ M_j^f &= E_f I_f \left(\left(\frac{d^2}{dx^2} + 2\mathbf{i}jq \frac{d}{dx} - j^2 q^2 \right) w_j^f \right) \end{aligned} \quad (4.29)$$

The generalized strain $\{\gamma^f\}$ of the film could be defined as:

$$\{\gamma^f\} = ([\mathbf{H}] + \frac{1}{2}[\mathbf{A}(\boldsymbol{\theta}^f)])\{\boldsymbol{\theta}^f\} \quad (4.30)$$

in which

$$[\mathbf{H}] = \begin{bmatrix} 1 & 0 & 0 & 0 & 0 & 0 & \cdots & 0 & 0 & 0 \\ 0 & 0 & 1 & 0 & 0 & 0 & \cdots & 0 & 0 & 0 \\ 0 & 0 & 0 & 1 & 0 & 0 & \cdots & 0 & 0 & 0 \\ 0 & 0 & 0 & 0 & 1 & 0 & \cdots & 0 & 0 & 0 \\ 0 & 0 & 0 & 0 & 0 & 1 & \cdots & 0 & 0 & 0 \\ \vdots & \vdots & \vdots & \vdots & \vdots & \vdots & \ddots & 0 & 0 & 0 \\ 0 & 0 & 0 & 0 & 0 & 0 & 0 & 1 & 0 & 0 \\ 0 & 0 & 0 & 0 & 0 & 0 & 0 & 0 & 1 & 0 \\ 0 & 0 & 0 & 0 & 0 & 0 & 0 & 0 & 0 & 1 \end{bmatrix} \quad (4.31)$$

$$[\mathbf{A}(\boldsymbol{\theta}^f)] = 2 \begin{bmatrix} 0 & \frac{1}{2}w_{0,x}^f & 0 & q^2w_1^f & w_{1,x}^f & 0 & \cdots & j^2q^2w_{n_j}^f & w_{n_j,x}^f & 0 \\ 0 & 0 & 0 & 0 & 0 & 0 & \cdots & 0 & 0 & 0 \\ 0 & 0 & 0 & 0 & 0 & 0 & \cdots & 0 & 0 & 0 \\ 0 & 0 & 0 & 0 & 0 & 0 & \cdots & 0 & 0 & 0 \\ 0 & 0 & 0 & 0 & 0 & 0 & \cdots & 0 & 0 & 0 \\ \vdots & \vdots & \vdots & \vdots & \vdots & \vdots & \ddots & 0 & 0 & 0 \\ 0 & 0 & 0 & 0 & 0 & 0 & 0 & 0 & 0 & 0 \\ 0 & 0 & 0 & 0 & 0 & 0 & 0 & 0 & 0 & 0 \\ 0 & 0 & 0 & 0 & 0 & 0 & 0 & 0 & 0 & 0 \end{bmatrix}$$

$$\langle \boldsymbol{\theta}^f \rangle = \left\langle \begin{matrix} u_{0,x}^f & w_{0,x}^f & w_{0,xx}^f & w_1^f & w_{1,x}^f & w_{1,xx}^f & \cdots & w_{n_j}^f & w_{n_j,x}^f & w_{n_j,xx}^f \end{matrix} \right\rangle \quad (4.32)$$

where $[\mathbf{H}] \in \mathbb{R}^{(2+3n_j) \times (3+3n_j)}$, $[\mathbf{A}(\boldsymbol{\theta}^f)] \in \mathbb{R}^{(2+3n_j) \times (3+3n_j)}$ and $\{\boldsymbol{\theta}^f\} \in \mathbb{R}^{(3+3n_j) \times 1}$. Note that $[\mathbf{A}(\boldsymbol{\theta}^f)]$ and $\{\boldsymbol{\theta}^f\}$ are linear functions of u_0^f , w_0^f and w_j^f , thus the internal virtual work of the film Eq. (4.28) is a quadratic expression in terms of the displacement, and the generalized stress $\{\mathbf{S}^f\}$ is defined as:

$$\{\mathbf{S}^f\} = [\mathbf{D}^f]([\mathbf{H}] + \frac{1}{2}[\mathbf{A}(\boldsymbol{\theta}^f)]) \{\boldsymbol{\theta}^f\} \quad (4.33)$$

in which:

$$[\mathbf{D}^f] = \text{diag}(E_f b h_f \quad 2E_f b h_f \quad E_f I_f \quad 2q^4 E_f I_f \quad 12q^2 E_f I_f \quad 2E_f I_f \quad \cdots \quad 2n_j^4 q^4 E_f I_f \quad 12n_j^2 q^2 E_f I_f \quad 2E_f I_f) \quad (4.34)$$

To unify the unknowns, the unknown vector $\{\boldsymbol{\theta}^f\}$ of the film is expressed as a function of the whole unknown vector $\{\boldsymbol{\theta}\} \in \mathbb{R}^{(6+4n_j+(4+2n_j)(n_c+n_b+1)) \times 1}$ by introducing a transform matrix $[\mathbf{R}^f]$:

$$\{\boldsymbol{\theta}^f\} = [\mathbf{R}^f] \{\boldsymbol{\theta}\} \quad (4.35)$$

where

$$\begin{aligned} \langle \boldsymbol{\theta} \rangle = & \langle u_0^f \quad u_{0,x}^f \quad w_0^f \quad w_{0,x}^f \quad w_{0,xx}^f \quad \cdots \quad w_{n_j}^f \quad w_{n_j,x}^f \quad w_{n_j,xx}^f \\ & u_1^c \quad u_{1,x}^c \quad \cdots \quad u_{n_c}^c \quad u_{n_c,x}^c \quad (w_1^c)_0 \quad (w_{1,x}^c)_0 \quad \cdots \quad (w_{n_c}^c)_0 \\ & (w_{n_c,x}^c)_0 \quad \cdots \quad (w_1^c)_{n_j} \quad (w_{1,x}^c)_{n_j} \quad \cdots \quad (w_{n_c}^c)_{n_j} \quad (w_{n_c,x}^c)_{n_j} \\ & u_0^b \quad u_{0,x}^b \quad \cdots \quad u_{n_b}^b \quad u_{n_b,x}^b \quad (w_0^b)_0 \quad (w_{0,x}^b)_0 \quad \cdots \quad (w_{n_b}^b)_0 \quad (w_{n_b,x}^b)_0 \quad \cdots \quad (w_0^b)_{n_j} \\ & (w_{0,x}^b)_{n_j} \quad \cdots \quad (w_{n_b}^b)_{n_j} \quad (w_{n_b,x}^b)_{n_j} \quad \mu_1 \quad (\mu_2)_0 \quad \cdots \quad (\mu_2)_{n_j} \rangle \end{aligned} \quad (4.36)$$

for the sake of brevity, the details of the transform matrix are not presented. Thus, the virtual work of the film could be written as:

$$\delta \mathcal{P}_{int}^f = \int_0^L \langle \delta \boldsymbol{\gamma}^f \rangle \{\mathbf{S}^f\} dx = \int_0^L \langle \delta \boldsymbol{\theta} \rangle^T [\mathbf{R}^f]^T ([\mathbf{H}] + [\mathbf{A}(\boldsymbol{\theta}^f)]) \{\mathbf{S}^f\} dx \quad (4.37)$$

where $^T[\square]$ represents the transpose of a matrix.

4.3.1.2 Internal virtual work of the core substrate

By applying the macroscopic displacement fields Eqs. (4.20), (4.22) and the macroscopic stress Eq. (4.23) of core substrate into Eq. (4.24), the virtual work of the core substrate becomes:

$$\begin{aligned} \delta \mathcal{P}_{int}^c = & \int_{V^c} \sum_{j=-n_j}^{+n_j} \left((\sigma_{xx}^c)_j \delta(\epsilon_{xx}^c)_{-j} + (\sigma_{zz}^c)_j \delta(\epsilon_{zz}^c)_{-j} + 2(\sigma_{xz}^c)_j \delta(\epsilon_{xz}^c)_{-j} \right) dV^c \\ = & \int_0^L \left[N_{xx0}^c \delta u_{0,x}^f + M_{1xz0}^c \delta w_{0,x}^f + M_{2xx0}^c \delta w_{0,xx}^f + M_{xxzxj}^c \delta w_{-j}^f \right. \\ & + M_{1xzxj}^c \delta w_{-j,x}^f + M_{2xxj}^c \delta w_{-j,xx}^f + N_{xzi}^c \delta u_i^c + N_{xxi}^c \delta u_{i,x}^c \\ & \left. + M_{zzz0}^c \delta(w_i^c)_0 + M_{1xzi0}^c \delta(w_{i,x}^c)_0 + M_{zzxzi}^c \delta(w_i^c)_{-j} + M_{1xzi}^c \delta(w_{i,x}^c)_{-j} \right] \end{aligned} \quad (4.38)$$

where $i \in [1, n_c]$, $j \in [1, n_j]$. Because $\mathcal{U}^s(x, z)$ does not fluctuate along the x direction according to Section 3.1, i.e., $\mathcal{U}^s(x, z) = \mathcal{U}_0^s(x, z)$, the in-plane strain ϵ_{xx}^s and stress σ_{xx}^s show no oscillation: $\epsilon_{xx}^s = (\epsilon_{xx}^s)_0$, $\sigma_{xx}^s = (\sigma_{xx}^s)_0$. This would cause a

spurious phenomenon called “oscillation locking” in the macroscopic film/substrate model. The mechanism of the phenomenon is carefully explained and two proper remedies are proposed to treat it in Huang et al. (2017a). In this Chapter, one of the two remedies, similar to the way of treating the Poisson locking in plate theories (Carrera and Brischetto (2008a)), is used by modifying the constitutive relations in the substrate. As a result, the modified elastic coefficients are $C_{11} = C_{33} = E_s$, $C_{13} = 0$, $C_{55} = E_s/2(1 + \nu_s)$. The core stress resultants are:

$$\begin{aligned}
\frac{N_{xx0}^c}{b} &= J_{00}^{11c}(u_{0,x}^f + \frac{h_f}{2}w_{0,xx}^f) + J_{0i}^{11c}u_{i,x}^c + J_{0i,z}^{13c}(w_i^c)_0 \\
\frac{M_{1xz0}^c}{b} &= J_{00}^{55c}w_{0,x}^f + J_{0i,z}^{55c}u_i^c + J_{0i}^{55c}w_{0,x}^c \\
\frac{M_{2xx0}^c}{b} &= J_{00}^{11c}\frac{h_f}{2}(u_{0,x}^f + \frac{h_f}{2}w_{0,xx}^f) + J_{0i}^{11c}\frac{h_f}{2}u_{i,x}^c + J_{0i}^{13c}\frac{h_f}{2}(w_i^c)_0 \\
\frac{M_{xzxj}^c}{b} &= (j^2q^2J_{jj}^{11c} + J_{jj}^{55c})w_j^f - J_{jj}^{11c}w_{j,xx}^f + J_{ij}^{55c}(w_i^c)_j - J_{0i,z}^{13c}h_fj^2q^2(w_i^c)_j \\
\frac{M_{1xzxj}^c}{b} &= J_{1jj}^{1155c}w_{j,x}^f + J_{1ij}^{55c}(w_{i,x}^c)_j \\
\frac{M_{2xxj}^c}{b} &= -J_{jj}^{11c}w_j + J_{00}^{11c}\frac{h_f^2}{2}w_{j,xx}^f + J_{0i,z}^{13c}h_f(w_i^c)_j \\
\frac{N_{xzi}^c}{b} &= J_{i,z0}^{55c}w_{0,x}^f + J_{i,zm,z}^{55c}u_m^c + J_{i,zm}^{55c}(w_{m,x}^c)_0 \\
\frac{N_{xxi}^c}{b} &= J_{i0}^{11c}(u_{0,x}^f + \frac{h_f}{2}w_{0,xx}^f) + J_{im}^{11c}u_{m,x}^c + J_{im,z}^{13c}(w_m^c)_0 \\
\frac{M_{zzi0}^c}{b} &= J_{i,zm,z}^{33c}(w_m^c)_0 + J_{i,z0}^{13c}u_{0,x}^f + J_{i,z0}^{13c}\frac{h_f}{2}j^2q^2w_{0,xx}^f + J_{i,zm}^{13c}u_{i,x}^c \\
\frac{M_{1xzi0}^c}{b} &= J_{i0}^{55c}w_{0,x}^f + J_{im,z}^{55c}u_m^c + J_{im}^{55c}(w_{m,x}^c)_0 \\
\frac{M_{zzxzij}^c}{b} &= 2j^2q^2J_{i0}^{55c}w_j^f + (2J_{i,zm,z}^{33c} + 2j^2q^2J_{im}^{55c})(w_m^c)_j \\
&\quad + 2J_{i,z0}^{13c}(\frac{h_f}{2}w_{j,xx}^f - j^2q^2w_j^f) \\
\frac{M_{1xzij}^c}{b} &= 2J_{0i}^{55c}w_{j,x}^f + 2J_{im}^{55c}(w_{m,x}^c)_j
\end{aligned} \tag{4.39}$$

where $J_{\square}^{\square c}$ are the constant terms related to the elastic coefficients and the

thickness of the core substrate

$$\begin{aligned}
J_{im}^{xxc} &= \int_{h_b}^{h_s} C_{xx}^c (F_i - \bar{F}_i)(F_m - \bar{F}_m) dz \\
J_{i,zm,z}^{xxc} &= \int_{h_b}^{h_s} C_{xx}^c (F_i - \bar{F}_i)_{,z} (F_m - \bar{F}_m)_{,z} dz \\
J_{i,zm}^{xxc} &= \int_{h_b}^{h_s} C_{xx}^c (F_i - \bar{F}_i)_{,z} (F_m - \bar{F}_m) dz \\
J_{im,z}^{xxc} &= \int_{h_b}^{h_s} C_{xx}^c (F_i - \bar{F}_i) (F_m - \bar{F}_m)_{,z} dz \\
J_{00}^{xxc} &= C_{xx}^c h_c \tag{4.40} \\
J_{i0}^{xxc} &= J_{0i}^{xxc} = \int_{h_b}^{h_s} C_{xx}^c (F_i - \bar{F}_i) dz \\
J_{i,z0}^{xxc} &= J_{0i,z}^{xxc} = \int_{h_b}^{h_s} C_{xx}^c F_{i,z} dz \\
J_{jj}^{11c} &= C_{11}^c \frac{h_f^2}{2} j^2 q^2 h_c, \quad J_{jj}^{55c} = 2C_{55}^c j^2 q^2 h_c, \quad J_{ij}^{55c} = 2j^2 q^2 J_{0i}^{55c} \\
J_{1jj}^{1155c} &= 4J_{jj}^{11c} + 2J_{00}^{55c}, \quad J_{1ij}^{55c} = 2J_{0i}^{55c}
\end{aligned}$$

The superscript “ xx ” represents 11, 13, 33 or 55, see details in Yang et al. (2015).

As a consequence, Eqs. (4.38) and (4.39) can be rewritten in the matrix form in terms of displacements:

$$\delta \mathcal{P}_{int}^c = \int_0^L \langle \delta \boldsymbol{\theta}^c \rangle [\mathbf{D}^c] \{ \boldsymbol{\theta}^c \} dx \tag{4.41}$$

where $[\mathbf{D}^c]$ is the generalised stiffness matrix of core layer that is not here explicitly reported for the sake of brevity, $\{ \boldsymbol{\theta}^c \} \in \mathbb{R}^{(3+3n_j+4n_c+2n_cn_j) \times 1}$ is a vector whose components are the core generalised displacement unknown functions and their

derivatives versus the axial coordinate. It reads as:

$$\begin{aligned} \langle \boldsymbol{\theta}^c \rangle = & \langle u_{0,x}^f \quad w_{0,x}^f \quad w_{0,xx}^f \quad w_1^f \quad w_{1,x}^f \quad w_{1,xx}^f \quad \cdots \quad w_{n_j}^f \quad w_{n_j,x}^f \quad w_{n_j,xx}^f \\ & (u_1^c)_0 \quad \cdots \quad (u_{n_c}^c)_0 \quad (u_{1,x}^c)_0 \quad \cdots \quad (u_{n_c,x}^c)_0 \quad (w_1^c)_0 \quad \cdots \quad (w_{n_c}^c)_0 \\ & (w_{1,x}^c)_0 \quad \cdots \quad (w_{n_c,x}^c)_0 \quad \cdots \quad (w_1^c)_{n_j} \quad \cdots \quad (w_{n_c}^c)_{n_j} \quad (w_{1,x}^c)_{n_j} \quad \cdots \quad (w_{n_c,x}^c)_{n_j} \rangle \end{aligned} \quad (4.42)$$

By unifying the unknowns, the internal virtual work of the core substrate is formulated as:

$$\delta \mathcal{P}_{int}^c = \int_0^L \langle \delta \boldsymbol{\theta}^c \rangle [\mathbf{D}^c] \{ \boldsymbol{\theta}^c \} dx = \int_0^L \langle \delta \boldsymbol{\theta} \rangle^T [\mathbf{R}^c] [\mathbf{D}^c] [\mathbf{R}^c] \{ \boldsymbol{\theta} \} dx = \int_0^L \langle \delta \boldsymbol{\theta} \rangle [\mathbf{K}^c] \{ \boldsymbol{\theta} \} dx \quad (4.43)$$

where $[\mathbf{R}^c]$ is the transition matrix between the total unknown vector $\{ \boldsymbol{\theta} \}$ and the unknown vector of the core $\{ \boldsymbol{\theta}^c \}$.

4.3.1.3 Internal virtual work of the bottom substrate

The derivation process of internal virtual work of the bottom substrate is more or less the same as that of the core layer by replacing Eq. (4.21) and integrating over through-the-thickness and -width coordinates, the internal virtual work of the bottom layer is given as following:

$$\begin{aligned} \delta \mathcal{P}_{int}^b = & \int_{V^b} \sum_{j=-n_j}^{+n_j} \left((\sigma_{xx}^b)_j \delta(\epsilon_{xx}^b)_{-j} + (\sigma_{zz}^b)_j \delta(\epsilon_{zz}^b)_{-j} + 2(\sigma_{xz}^b)_j \delta(\epsilon_{xz}^b)_{-j} \right) dV^b \\ = & \int_0^L \left[N_{xzn}^b \delta u_n^b + N_{xxn}^b \delta u_{n,x}^b + M_{zzn0}^b \delta(w_n^b)_0 \right. \\ & \left. + M_{1xzn0}^b \delta(w_{n,x}^b)_0 + M_{xznj}^b \delta(w_n^b)_{-j} + M_{1xznj}^b \delta(w_{n,x}^b)_{-j} \right] dx \end{aligned} \quad (4.44)$$

where $n \in [0, n_b]$, $j \in [1, n_j]$. The bottom stress resultants are:

$$\begin{aligned}
\frac{N_{xzn}^b}{b} &= J_{n,zp,z}^{55b} u_p^b + J_{n,zp}^{55b} (w_{p,x}^b)_0 \\
\frac{N_{xxn}^b}{b} &= J_{np}^{11b} u_{p,x}^b + J_{np,z}^{13b} (w_p^b)_0 \\
\frac{M_{zzn0}^b}{b} &= J_{n,zp,z}^{33b} (w_p^b)_0 + J_{n,zp}^{13b} u_{p,x}^b \\
\frac{M_{1xzn0}^b}{b} &= J_{np,z}^{55b} u_p^b + J_{np}^{55b} (w_{p,x}^b)_0 \\
\frac{M_{xznj}^b}{b} &= (2J_{n,zp,z}^{33b} + 2j^2 q^2 J_{np}^{55b}) (w_p^b)_j \\
\frac{M_{1xznj}^b}{b} &= 2J_{np}^{55b} (w_{p,x}^b)_j
\end{aligned} \tag{4.45}$$

where

$$\begin{aligned}
J_{np}^{xxb} &= \int_0^{h_b} C_{xx}^b F_n F_p dz \\
J_{n,zp,z}^{xxb} &= \int_0^{h_b} C_{xx}^b F_{n,z} F_{p,z} dz \\
J_{n,zp}^{xxb} &= \int_0^{h_b} C_{xx}^b F_{n,z} F_p dz \\
J_{np,z}^{xxb} &= \int_0^{h_b} C_{xx}^b F_n F_{p,z} dz
\end{aligned} \tag{4.46}$$

By introducing a transform matrix, the internal virtual work of the bottom substrate could be expressed as:

$$\delta \mathcal{P}_{int}^b = \int_0^L \langle \delta \boldsymbol{\theta}^b \rangle [\mathbf{D}^b] \{ \boldsymbol{\theta}^b \} dx = \int_0^L \langle \delta \boldsymbol{\theta} \rangle^T [\mathbf{R}^b] [\mathbf{D}^b] [\mathbf{R}^b] \{ \boldsymbol{\theta} \} dx = \int_0^L \langle \delta \boldsymbol{\theta} \rangle [\mathbf{K}^b] \{ \boldsymbol{\theta} \} dx \tag{4.47}$$

in which

$$\begin{aligned}
\langle \boldsymbol{\theta}^b \rangle &= \langle (u_0^b)_0 \cdots (u_{n_b}^b)_0 (u_{0,x}^b)_0 \cdots (u_{n_b,x}^b)_0 (w_0^b)_0 \cdots (w_{n_b}^b)_0 \\
&\quad (w_{0,x}^b)_0 \cdots (w_{n_b,x}^b)_0 \cdots (w_0^b)_{n_j} \cdots (w_{n_b}^b)_{n_j} (w_{0,x}^b)_{n_j} \cdots (w_{n_b,x}^b)_{n_j} \rangle
\end{aligned} \tag{4.48}$$

where $\{ \boldsymbol{\theta}^b \} \in \mathbb{R}^{2(n_b+1)(n_j+2) \times 1}$, $[\mathbf{R}^b] \in \mathbb{R}^{2(n_b+1)(n_j+2) \times (6+4n_j+(4+2n_j)(n_c+n_b+1))}$.

The congruency of the displacement field at core and bottom layers' interface Γ is realised by means of the Lagrange multiplier $\boldsymbol{\mu}$ through $\delta \mathcal{L}$, whose variation

formulation is as following:

$$\begin{aligned}
\delta\mathcal{L} &= \mathcal{L}(\delta\boldsymbol{\mu}, \mathbf{u}) + \mathcal{L}(\boldsymbol{\mu}, \delta\mathbf{u}) \\
&= \int_{\Gamma} \delta\mu_1 \left[\mathcal{U}^c(x, h_b) - \mathcal{U}^b(x, h_b) \right] + \delta(\mu_2)_0 \left[\mathcal{W}_0^c(x, h_b) - \mathcal{W}_0^b(x, h_b) \right] \\
&\quad + \delta(\mu_2)_j \left[\mathcal{W}_j^c(x, h_b) - \mathcal{W}_j^b(x, h_b) \right] d\Gamma \\
&+ \int_{\Gamma} \mu_1 \left[\delta\mathcal{U}^c(x, h_b) - \delta\mathcal{U}^b(x, h_b) \right] + (\mu_2)_0 \left[\delta\mathcal{W}_0^c(x, h_b) - \delta\mathcal{W}_0^b(x, h_b) \right] \\
&\quad + (\mu_2)_j \left[\delta\mathcal{W}_j^c(x, h_b) - \delta\mathcal{W}_j^b(x, h_b) \right] d\Gamma
\end{aligned} \tag{4.49}$$

where $j \in [1, n_j]$. Then substituting the Eqs. (4.20) and (4.21) into Eq. (4.49) gets:

$$\begin{aligned}
\delta\mathcal{L} &= b \int_0^L \delta\mu_1 \left[u_0^f + \frac{1}{2}h_f \sum_{j=-n_j}^{n_j} \left(\frac{d}{dx} + \mathbf{i}jq \right) w_j + (\tilde{F}_i - \bar{F}_i)u_i^c - \tilde{F}_n u_n^b \right] \\
&\quad + \delta(\mu_2)_0 \left[w_0^f + (\tilde{F}_i - \bar{F}_i)(w_i^c)_0 - \tilde{F}_n (w_n^b)_0 \right] \\
&\quad + \delta(\mu_2)_j \left[w_j^f + (\tilde{F}_i - \bar{F}_i)(w_i^c)_j - \tilde{F}_n (w_n^b)_j \right] dx \\
&+ b \int_0^L \mu_1 \left[\delta u_0^f + \frac{1}{2}h_f (\delta w_{0,x}^f + \sum_{j=-n_j}^{n_j} \left(\frac{d}{dx} + \mathbf{i}jq \right) \delta w_j) + (\tilde{F}_i - \bar{F}_i) \delta u_i^c - \tilde{F}_n \delta u_n^b \right] \\
&\quad + (\mu_2)_0 \left[\delta w_0^f + (\tilde{F}_i - \bar{F}_i) \delta (w_i^c)_0 - \tilde{F}_n \delta (w_n^b)_0 \right] \\
&\quad + (\mu_2)_j \left[\delta w_j^f + (\tilde{F}_i - \bar{F}_i) \delta (w_i^c)_j - \tilde{F}_n \delta (w_n^b)_j \right] dx
\end{aligned} \tag{4.50}$$

in which $\tilde{F}_\tau = h_b^\tau$. After introducing a transform matrix $[\mathbf{R}^{cp}]$, Eq. (4.50) can be rewritten into the matrix form:

$$\delta\mathcal{L}(\boldsymbol{\mu}, \mathbf{u}) = \int_0^L \langle \delta\boldsymbol{\theta}^{cp} \rangle [\mathbf{D}^{cp}] \{ \boldsymbol{\theta}^{cp} \} dx = \int_0^L \langle \delta\boldsymbol{\theta} \rangle^T [\mathbf{R}^{cp}] [\mathbf{D}^{cp}] [\mathbf{R}^{cp}] \{ \boldsymbol{\theta} \} dx = \int_0^L \langle \delta\boldsymbol{\theta} \rangle [\mathbf{K}^{cp}] \{ \boldsymbol{\theta} \} dx \tag{4.51}$$

4.3.1.4 Governing equation

In this Chapter, the body forces are neglected, then the external virtual work could be

$$\delta\mathcal{P}_{ext} = \lambda \int_{S_\sigma} \langle \delta\boldsymbol{\theta} \rangle \{ \mathbf{F} \} dS \tag{4.52}$$

where $\{\mathbf{F}\}$ is the external applied force, and λ is a "load parameter". Hence, the macroscopic governing equation is expressed as:

$$\begin{aligned}
& \int_0^L \langle \delta \boldsymbol{\theta} \rangle^T [\mathbf{R}^f]^T ([\mathbf{H}] + [\mathbf{A}(\boldsymbol{\theta}^f)]) \{\mathbf{S}^f\} dx + \int_0^L \langle \delta \boldsymbol{\theta} \rangle ([\mathbf{K}^c] + [\mathbf{K}^b] + [\mathbf{K}^{cp}]) \{\boldsymbol{\theta}\} dx \\
& = \lambda \int_{S_\sigma} \langle \delta \boldsymbol{\theta} \rangle \{\mathbf{F}\} dS \\
& \{\mathbf{S}^f\} = [\mathbf{D}^f] ([\mathbf{H}] + \frac{1}{2} [\mathbf{A}(\boldsymbol{\theta}^f)]) [\mathbf{R}^f] \{\boldsymbol{\theta}\}
\end{aligned} \tag{4.53}$$

4.3.2 Discretization

The finite element method is used to solve the nonlinear system of Eq. (4.53). A two-node 1D element with $(3 + 2n_j) \cdot (n_c + n_b + 3)$ degrees of freedom for each node is used, which results in the following nodal unknown vector:

$$\begin{aligned}
\mathbf{q}^{IT} = & \{ u_0^f \quad w_0^f \quad w_{0,x}^f \quad w_1^f \quad w_{1,x}^f \quad \cdots \quad w_{n_j}^f \quad w_{n_j,x}^f \\
& u_1^c \quad \cdots \quad u_{n_c}^c \quad (w_1^c)_0 \quad \cdots \quad (w_{n_c}^c)_0 \quad (w_{1,x}^c)_0 \quad \cdots \quad (w_{n_c,x}^c)_0 \quad \cdots \quad (w_1^c)_{n_j} \quad \cdots \quad (w_{n_c}^c)_{n_j} \\
& (w_{1,x}^c)_{n_j} \quad \cdots \quad (w_{n_c,x}^c)_{n_j} \quad u_0^b \quad \cdots \quad u_{n_b}^b \quad (w_0^b)_0 \quad \cdots \quad (w_{n_b}^b)_0 \\
& (w_{0,x}^b)_0 \quad \cdots \quad (w_{n_b,x}^b)_0 \quad \cdots \quad (w_0^b)_{n_j} \quad \cdots \quad (w_{n_b}^b)_{n_j} \\
& (w_{0,x}^b)_{n_j} \quad \cdots \quad (w_{n_b,x}^b)_{n_j} \quad \mu_1 \quad (\mu_2)_0 \quad (\mu_{2,x})_0 \quad \cdots \quad (\mu_2)_{n_j} \quad (\mu_{2,x})_{n_j} \}
\end{aligned} \tag{4.54}$$

$$\{\mathbf{v}\} = \left\{ \begin{array}{c} \mathbf{v}^I \\ \mathbf{v}^{II} \end{array} \right\} \tag{4.55}$$

where I and II denote the first and the second node of the element, $\{\mathbf{v}\}$ is the elementary vector of unknowns. The longitudinal unknown displacement functions u_0^f , u_τ^c , u_τ^b and the Lagrange multiplier μ_1 are discretised by the Lagrange linear shape functions, while the unknowns transverse displacement functions w_j^f , $(w_\tau^c)_j$, $(w_\tau^b)_j$ and the Lagrange multipliers $(\mu_2)_j$ by the Hermite shape functions. The unified discretization of the unknowns can be obtained by:

$$\begin{aligned}
\mathcal{V}_\mathcal{L} & = \Gamma(1)\mathcal{V}_\mathcal{L}^I + \Gamma(2)\mathcal{V}_\mathcal{L}^{II} = \langle \mathbf{N}_\mathcal{L} \rangle \{\mathbf{v}\} \\
\mathcal{V}_\mathcal{H} & = \Gamma(3)\mathcal{V}_\mathcal{H}^I + \Gamma(4)\mathcal{V}_\mathcal{H}^I + \Gamma(5)\mathcal{V}_\mathcal{H}^{II} + \Gamma(6)\mathcal{V}_\mathcal{H}^{II} = \langle \mathbf{N}_\mathcal{H} \rangle \{\mathbf{v}\}
\end{aligned} \tag{4.56}$$

in which, $\mathcal{V}_\mathcal{L}$ denotes the linear functions and $\mathcal{V}_\mathcal{H}$ denotes the Hermite functions, $\langle \mathbf{N}_\mathcal{L} \rangle$ and $\langle \mathbf{N}_\mathcal{H} \rangle$ are corresponding interpolation function matrices whose nonzero

elements are determined by:

$$\Gamma = \left\langle \frac{1-\xi}{2} \quad \frac{1+\xi}{2} \quad \frac{(1-\xi)^2(2+\xi)}{4} \quad \frac{l_e(1-\xi^2)(1-\xi)}{8} \quad \frac{(1+\xi)^2(2-\xi)}{4} \quad \frac{l_e(-1+\xi^2)(1+\xi)}{8} \right\rangle \quad (4.57)$$

The parameter ξ is the elementary local coordinate and l_e is the length of the element. Here, we take u_i^c and $(w_i^c)_j$ for example:

$$u_i^c = \Gamma(1)u_i^{cI} + \Gamma(2)u_i^{cII} = \langle \mathbf{N}_{u_i}^c \rangle \{ \mathbf{v} \} \quad (4.58)$$

$$(w_i^c)_j = \Gamma(3)(w_i^c)_j^I + \Gamma(4)(w_{i,x}^c)_j^I + \Gamma(5)(w_i^c)_j^{II} + \Gamma(6)(w_{i,x}^c)_j^{II} = \langle \mathbf{N}_{w_{ij}}^c \rangle \{ \mathbf{v} \} \quad (4.59)$$

where $\langle \mathbf{N}_{u_i}^c \rangle$ and $\langle \mathbf{N}_{w_{ij}}^c \rangle$ are, respectively, the interpolation function matrix for u_i^c and $(w_i^c)_j$. Other unknowns can be discretised as similar to these definitions. Thus, the unknown vector $\{ \boldsymbol{\theta} \}$ is expressed as:

$$\{ \boldsymbol{\theta} \} = [\mathbf{G}] \{ \mathbf{v} \} \quad (4.60)$$

where $[\mathbf{G}]$ is assembled by $\langle \mathbf{N}_{\mathcal{E}} \rangle$, $\langle \mathbf{N}_{\mathcal{S}} \rangle$ and their derivatives. By substituting Eq. (4.60) in Eq. (4.53), the discretization form of the governing equation is written as:

$$\begin{aligned} \sum_e \langle \delta \mathbf{v} \rangle \int_0^{l_e} \left({}^T [\mathbf{B}^f(\mathbf{v})] \{ \mathbf{S}^f \} + ([\tilde{\mathbf{K}}^c] + [\tilde{\mathbf{K}}^b] + [\tilde{\mathbf{K}}^{cp}]) \{ \mathbf{v} \} \right) dx = \lambda \sum_e \langle \delta \mathbf{v} \rangle \{ \mathbf{f} \}^e \\ \{ \mathbf{S}^f \} = [\mathbf{D}^f] ([\mathbf{B}_l^f] + \frac{1}{2} [\mathbf{B}_{nl}^f(\mathbf{v})]) \{ \mathbf{v} \} \end{aligned} \quad (4.61)$$

where

$$\begin{aligned} [\mathbf{B}^f(\mathbf{v})] &= [\mathbf{B}_l^f] + [\mathbf{B}_{nl}^f(\mathbf{v})] \\ [\mathbf{B}_l^f] &= [\mathbf{H}] [\mathbf{R}^f] [\mathbf{G}] \\ [\mathbf{B}_{nl}^f(\mathbf{v})] &= [\mathbf{A}(\mathbf{v})] [\mathbf{R}^f] [\mathbf{G}] \\ [\tilde{\mathbf{K}}^c] &= {}^T [\mathbf{G}] [\mathbf{K}^c] [\mathbf{G}] \\ [\tilde{\mathbf{K}}^b] &= {}^T [\mathbf{G}] [\mathbf{K}^b] [\mathbf{G}] \\ [\tilde{\mathbf{K}}^{cp}] &= {}^T [\mathbf{G}] [\mathbf{K}^{cp}] [\mathbf{G}] \\ \{ \mathbf{f} \}^e &= \int_{S_\sigma} {}^T [\mathbf{G}] \{ \mathbf{F} \} dS \end{aligned} \quad (4.62)$$

The Asymptotic Numerical Method (ANM) (Cochelin et al. (1994)) is used to solve the set of Eq. (4.61). For each element the unknown vector $\{ \mathbf{v} \}$ is determined at the nodes and the stress vector $\{ \mathbf{S}^f \}$ is determined at the Gauss points. Details on the use of the ANM for the resolution of non linear problems are given in Appendix

A 4.5. Besides, the various boundary conditions of macroscopic model have been deduced in Liu et al. (2012), which will not be illustrated any more in this Chapter.

4.4 Numerical results

In this part, the film/substrate system is subjected to compression as illustrated in Fig. 4.3. The bottommost surface of the substrate ($z = 0$) is clamped. The kinematic boundary condition is obtained straightforwardly by imposing the nodal DOFs corresponding to u_0^b , $(w_0^b)_j$ and $(w_{0,x}^b)_j$ equal to zero. The vertical displacements \mathscr{W} is simply supported and equal to zero at $x/L = 0$ and 1. Two concentrated forces of equal modulus F and opposite verse are applied along the axial direction at the through-the-thickness mid point of the film.

The results obtained by the macroscopic model are compared with the numerical results obtained by a two-dimensional nonlinear elasticity solution with the finite element code ABAQUS, which is referred to as "2D full model" in this paper. The film is modeled by 3-node beam elements (B22) and the substrate by 8-node plane-strain quadrilateral reduced integration elements (CPE8R). The rotational degree of freedom in the beam elements is constrained when connected with the plane-strain elements. To ensure accuracy, very fine meshes are adopted to discrete the film and substrate.

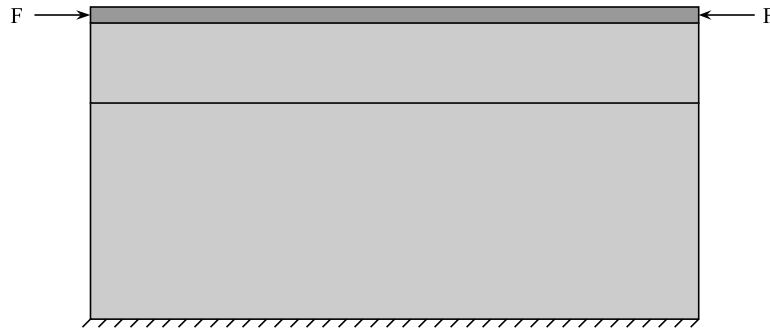


Figure 4.3: Sketch of the film/substrate system under compression forces

4.4.1 Validation

Table 4.1 presents the material properties and geometric parameters. The Young's modulus ratio E_s/E_f ranges from 10^{-5} to 10^{-3} . The thickness ratio h_s/h_f changes between 10, for very thin substrates, and 10^3 , for very thick substrates. This case is referred to as "problem I" to validate the 1D macroscopic model.

Table 4.1: Material and geometric parameters of the film/substrate. Problem I.

$E_f(10^4\text{MPa})$	E_s/E_f	ν_s	$L(10^{-1}\text{m})$	b(m)	h_f/L	h_s/h_f
6.9	$10^{-3} \sim 10^{-5}$	0.3	5.0	1.0	1/200	$10 \sim 10^3$

Table 4.2 presents the critical load parameter λ_c and the corresponding half-wave number q_0 for problem I. The critical load and wavenumber decrease as the substrate becomes softer and thicker. For a given E_s/E_f , the critical load and wavenumber change quite little when h_s/h_f exceeds 10^2 where the substrate becomes quite thick. This shows that only limited part of the substrate near film affects on the instability phenomenon while the remaining part is unstrained and shows almost no influence on such phenomenon (Huang et al. (2005); Yang et al. (2015)). The 1D macroscopic model yields accurate results compared with the 2D full model. The results are obtained by a 1D macroscopic model with $n_c = 7$, $n_b = 3$ and $n_j = 1$ (only zero and first order Fourier coefficients considered) and the mean field \mathscr{W}_0 being zero. The chosen expansion orders n_c and n_b have been proved to be sufficient enough for the considered cases, see Yang et al. (2015). For the present, 10 elements are used along the axis (mesh convergence will be investigated later), which results in about $4.29 \cdot 10^2$ DOFs. It is a half less than the minimum DOFs 10^3 by the 1D microscopic model in Yang et al. (2015). Besides, the 1D microscopic model's DOFs increase rapidly as the wavelength becomes shorter, whereas the mesh size of the 1D macroscopic model is independent on the wavelength change, which makes the 1D macroscopic model even more attractive considering that accurate results are obtained.

Table 4.2: Half-wave number q_0 and critical load parameter λ_c . The 1D macroscopic solution via a $n_c = 7$, $n_b = 3$ and $n_j = 1$ model with 10 axial elements. "2D" is short for the 2D full model by ABAQUS. Problem I.

h_s/h_f	10		10^2		10^3				
	q_0	$10^{-4}\lambda_c$	q_0	$10^{-4}\lambda_c$	q_0	$10^{-4}\lambda_c$			
E_s/E_f	1D		2D		1D		2D		
10^{-3}	13	133	133	10	109	107	10	111	107
10^{-4}	8	36.3	37.8	5	22.6	22.4	5	22.7	22.4
10^{-5}	5	11.9	12.6	3	5.46	5.42	3	5.45	5.42

4.4.2 Mesh convergence

In this section, the loading and boundary conditions of the film/substrate remain the same as shown in Fig. 4.3, and the material properties and the geometrical data are presented in Table 4.3, which has been studied by the 1D microscopic model in Yang et al. (2015). This case is referred to as "problem II".

Here, the thickness of core layer $h_c = 2\ell_w$ (ℓ_w is the wrinkling wavelength defined as $\ell_w = L/q_0$) proposed in Yang et al. (2015) is adopted in the 1D macroscopic model. The expansion orders for the core layer and bottom layer of the substrate are $n_c = 5$, $n_b = 3$ and $n_j = 1$. In ABAQUS, convergence has been carefully examined, and 50 elements along both the axial and transversal directions are enough to simulate the considered instability phenomenon. The DOFs of this corresponding mesh is about $1.57 \cdot 10^4$. The instability pattern for the problem II is presented in Fig. 4.4, where the 1D macroscopic model can correctly predict the wrinkling pattern compared with the 2D full model. Besides, an analysis of mesh convergence is carried out to ensure the accuracy of the proposed 1D macroscopic model. Fig. 4.5 presents the bifurcation curves for four mesh schemes ($ne = 2, 4, 8, 16$) of the 1D macroscopic model along the axial direction. The results converge to $\lambda_c = 0.0504$ with only 2 macroscopic elements (99 DOFs), which is very close to the critical load $\lambda_c = 0.0495$ obtained by the 2D full model (15705 DOFs). The 1D macroscopic model saves about 99% degrees of freedom and significantly decreases computation cost compared to the 2D full model.

Furthermore, the above critical load corresponds to the wrinkling pattern with the lowest critical load for the considered geometry and material configuration in problem II. The computation expenses will increase for buckling modes with more wavenumbers and smaller wavelengths for the 2D full model or the 1D microscopic model (Yang et al. (2015)), since a larger number of elements are needed to accurately simulate this phenomenon. Sometimes special imperfection should be applied to get the higher mode, which may lead to a great trouble in controlling the nonlinear solution path, see Hu et al. (2009a). However, the 1D macroscopic model easily overcomes the above shortcomings by just changing the wavenumber q_0 , and the corresponding critical load can be detected accurately and fast. Fig. 4.6 presents the higher mode of problem II with 33 wavenumbers. The 2D full model needs 200 elements along axis direction (242805 DOFs) to get the convergent solution, whereas the 1D macroscopic model only uses 2 elements (99 DOFs) to describe the higher buckling mode by applying a transverse perturbation force with a value of $F/10^5$ on the center of the system. The bifurcation curve in Fig. 4.7 shows that the

critical load of the macroscopic model is quite accurate with such a limited degrees of freedom. Therefore, the macroscopic model easily overcomes the disadvantages of the 1D microscopic model or the 2D full model and significantly improves the computational efficiency.

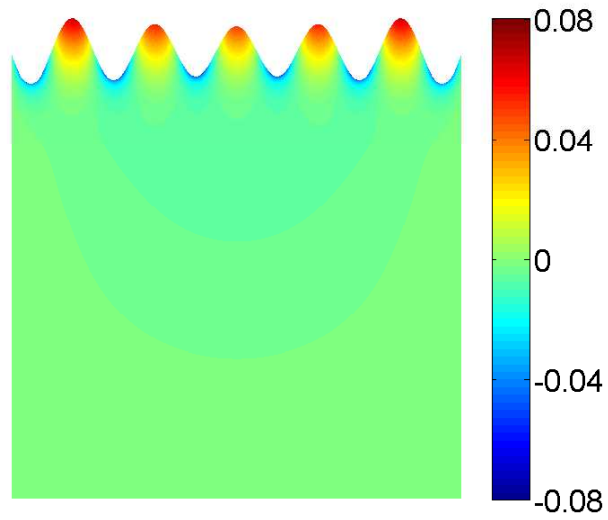
Table 4.3: Material and geometric parameters of the film/substrate. Problem II.

$E_f(10^5\text{MPa})$	E_s/E_f	ν_s	$L(10^{-3}\text{m})$	$b(10^{-3}\text{m})$	h_f/L	h_s/h_f
1.8	10^{-5}	0.3	1.0	1.0	10^{-3}	10^3

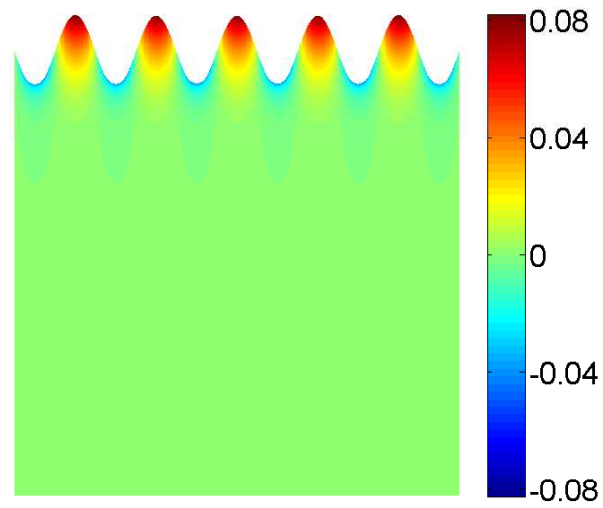
4.4.3 Fourier coefficient study

In this section, several Fourier coefficients $U_j(x, y)$ (referred specially to the Fourier coefficients of transverse displacement \mathcal{W} in the paper) are used to simulate the instability phenomenon. Usually, only the zero harmonic U_0 (mean field) and the first harmonic U_1 (envelop of the oscillation) are adopted, see Damil and Potier-Ferry (2010); Liu et al. (2012); Mhada et al. (2012); Hu et al. (2011); Yu et al. (2013). To determine the lowest critical load for a given structure, one should simulate several wrinkling patterns corresponding to different wavenumbers q_0 , and then choose the lowest one among them. Here, we introduce a new strategy to avoid the intensive simulation efforts by accounting several Fourier harmonics with different wavenumbers simultaneously in a single simulation. In this way, we can easily distinguish the harmonic that contributes the most to the bifurcation curves and conveniently predict the lowest wrinkling pattern with a random preset wavenumber. For simplicity, we take a shorter film/substrate system with $L = 0.8 \cdot 10^{-3}\text{m}$, and the other parameters remain the same as problem II. This case is referred to as 'problem III'.

For this considered case, the lowest wrinkling pattern has 8 wavenumbers as depicted in Fig. 4.8. The Fourier coefficients U_1, U_2, U_3, U_4 and U_5 are used in the 1D macroscopic model. These coefficients are assumed to be real, that is to say, the amplitude modulation is taken into account and the evolution of the phase is disregarded. The mean field U_0 is quite small and negligible in the considered film/substrate instability phenomenon. Small transverse perturbation forces $F/10^5$ are applied at the center of the structure. Results have been computed via a model with $n_c = 5$ and $n_b = 3$ and 2 elements along the x axis. First, the wavenumber q_0 is chosen as $q_0 = 2$. Fig. 4.9 presents the bifurcation curves obtained by the specified 1D macroscopic model. The notation U represents the microscopic transverse displacement, whereas U_j is the Fourier coefficient describing the j th



(a)



(b)

Figure 4.4: Transverse displacement $40 \cdot w$ (10^{-3} m) color map: (a) the 2D full model and (b) the 1D macroscopic model $n_c = 5$, $n_b = 3$ and $n_j = 1$. Problem II.

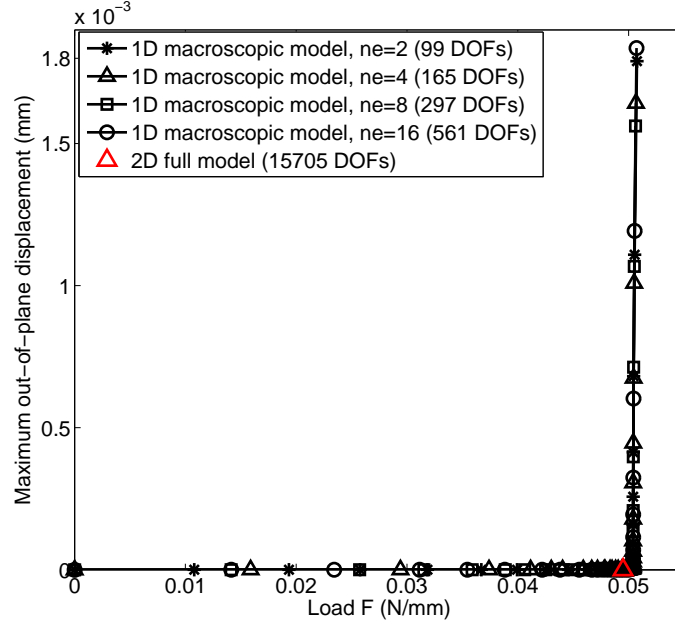
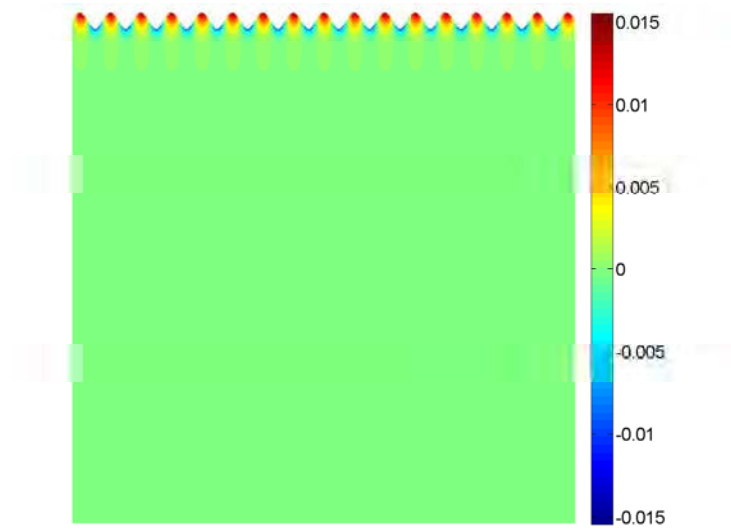


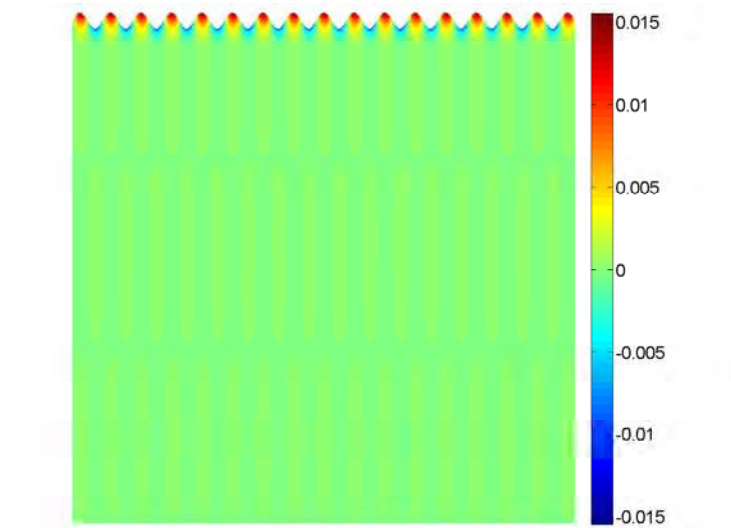
Figure 4.5: Bifurcation curves for four mesh schemes (“ne” is short for the number of element) of the 1D macroscopic model ($n_c = 5$, $n_b = 3$, $n_j = 1$, $h_c = 2\ell_w$). Problem II.

envelop of the transverse displacement. One can see that the coefficient of the 4th harmonic dominates the bifurcation path and leads to almost the same critical load predicted by the 2D full model. It seems that the 1D macroscopic model could automatically choose the proper Fourier coefficient to ensure the system in a state with minimum energy. Then the wavenumber q is changed to $q_0 = 4$, and Fig. 4.10 shows that the 1D macroscopic model choose the 2th harmonic as the main fluctuation mode. Besides, the out-of-plane deformation of the film near bifurcation point for the cases $q_0 = 2$ and $q_0 = 4$ has been plotted as shown in Fig. 4.11, which indicates that the corresponding main fluctuation mode describes the instability pattern correctly. There in fact exists fluctuation in the transversal displacement for other Fourier coefficients, but they are too small and makes little contribution to the buckling of the system.

The 1D macroscopic model accounting for several Fourier coefficients could conveniently and correctly predict the lowest critical load in the film/substrate instability phenomenon. Compared with the Landau-Ginzburg equation deduced from the asymptotic approach, the proposed model has an advantage to couple the evolution of several harmonics or envelops of the microscopic displacement field.



(a)



(b)

Figure 4.6: Transverse displacement $2 \cdot w$ (10^{-3} m) color map with 33 wavenumbers: (a) 2D full model and (b) 1D macroscopic model $n_c = 5$, $n_b = 3$ and $n_j = 1$. Problem II.

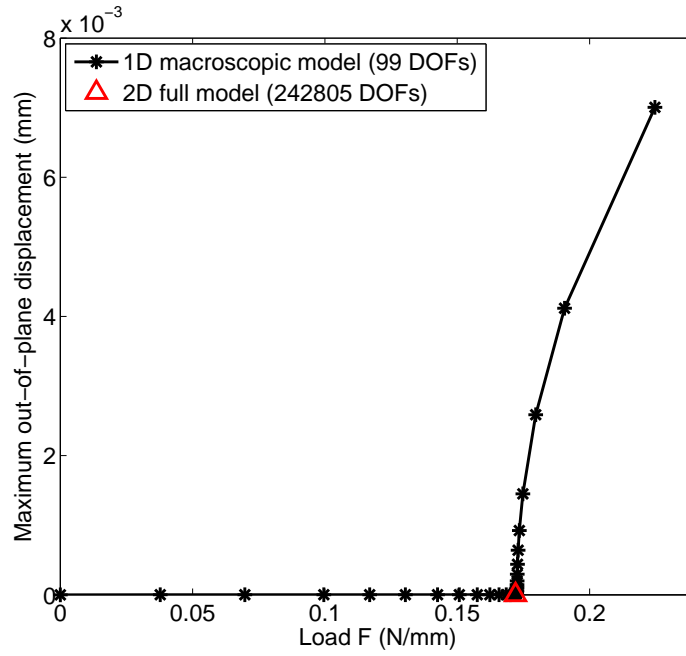


Figure 4.7: Bifurcation curves by the 1D macroscopic model with 33 wavenumbers ($n_c = 5$, $n_b = 3$, $h_c = 2\ell_w$). Problem II.

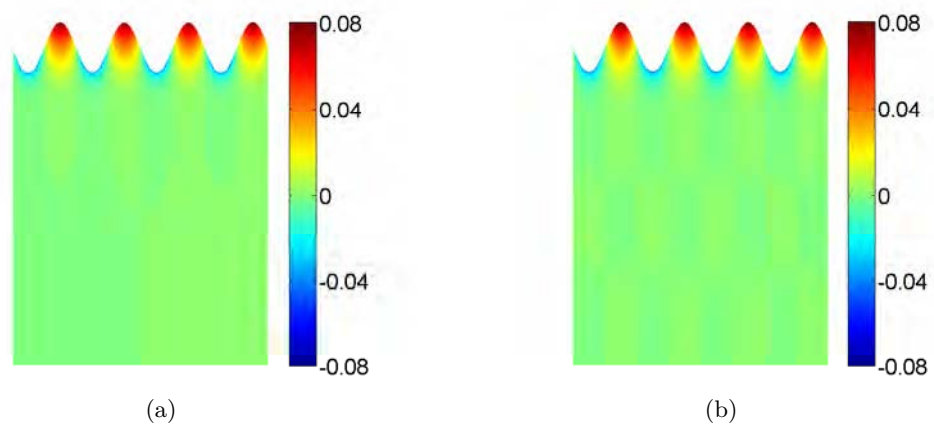


Figure 4.8: Transverse displacement $40 \cdot w$ (10^{-3} m) color map: (a) 2D full model and (b) 1D macroscopic model $n_c = 5$, $n_b = 3$ and $n_j = 5$. Problem III.

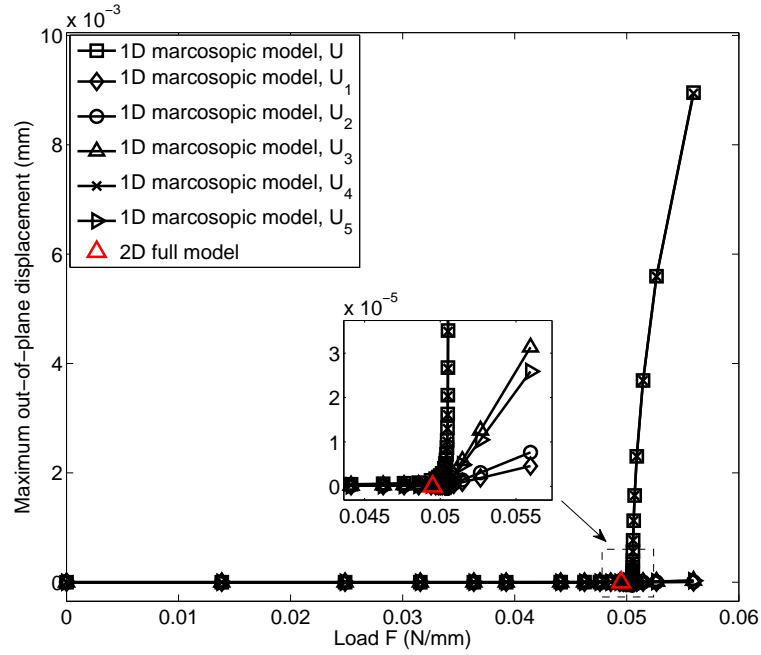


Figure 4.9: Bifurcation curves by the 1D macroscopic model with $q_0 = 2$. Problem III.

4.5 Conclusion

Based on a high order reduced-dimension model proposed by Yang et al. (2015), where the Euler-Bernoulli's beam was used for the thin film and the Carrera's Unified Formulation(CUF) for the substrate, a new macroscopic model is developed by the technique of slowly varying Fourier coefficient. The computational efficiency is significantly improved compared with the former model, especially when dealing with wrinkling instability phenomena with vast wavenumbers. Besides, several harmonics in Fourier series have been taken into account, and numerical experiments show that the proposed macroscopic model automatically predicts the lowest buckling mode. The present model is based on the method of Fourier series with variable coefficients that has been widely used for several structural models, such as the beam on Winkler foundation (Damil and Potier-Ferry (2010); Hu et al. (2011)), the sandwich models (Liu et al. (2012); Yu et al. (2013)) and the membrane model (Damil et al. (2014), Huang et al. (2015)). However, sometimes the results near the boundary show poor accuracy, which can be overcome by introducing the Arlequin method (Ben Dhia (2006), Hu et al. (2011, 2010), Yu et al. (2013)) coupling the microscopic model on the boundary and macroscopic model in the bulk.

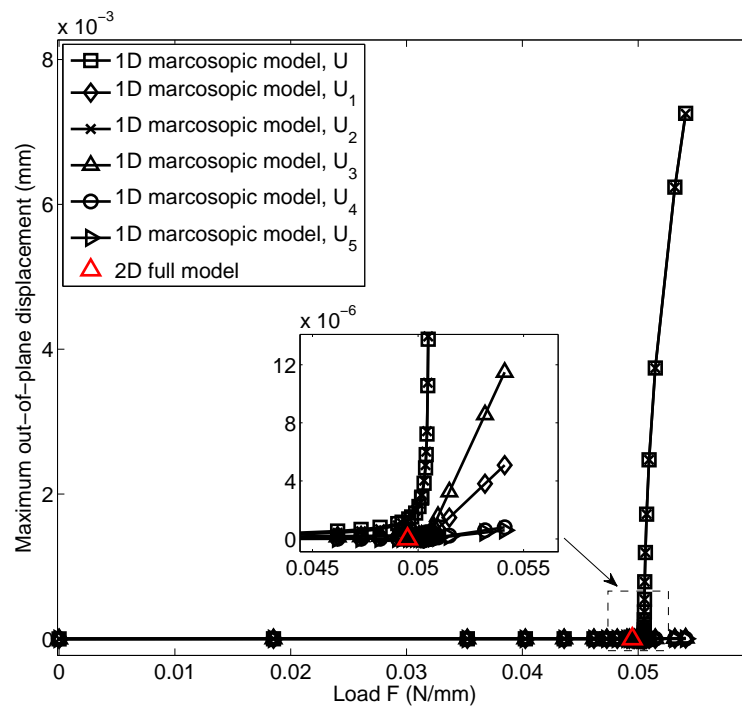
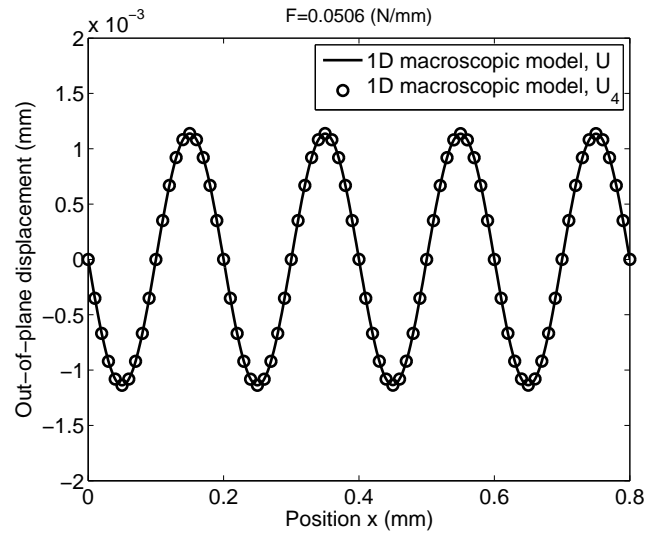
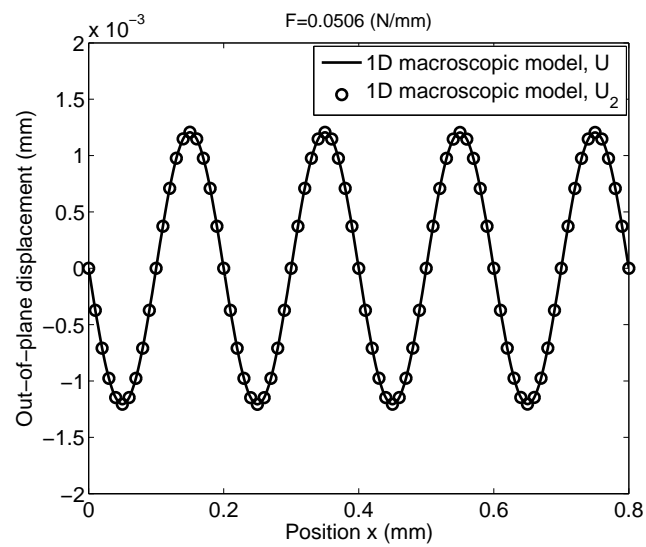


Figure 4.10: Bifurcation curves by the 1D macroscopic model with $q_0 = 4$. Problem III.



(a)



(b)

Figure 4.11: Transverse displacement of film by the 1D macroscopic model near bifurcation point: (a) $q_0 = 2$ and (b) $q_0 = 4$. Problem III.

Appendix A. Asymptotic numerical method

The solution to many physics problems can be achieved through resolution of nonlinear problems depending on real parameter Θ . The corresponding nonlinear system of equations can be written as follow:

$$\mathbf{R}(\Theta; \vartheta) = 0 \quad (4.63)$$

Assuming that a solution of Eq. 4.63 at point j is known, the solution $(\Theta; \vartheta)^{j+1}$ at point $j + 1$ is obtained from this latter following a perturbation technique. An approached solution path at step $j + 1$ is represented by a n -order Taylor series expansion of Θ and ϑ :

$$\begin{aligned} \Theta &= \Theta^j + a\Theta_1 + a^2\Theta_2 + \dots + a^n\Theta_n = \Theta^j + a^p\Theta_p \\ \vartheta &= \vartheta^j + a\vartheta_1 + a^2\vartheta_2 + \dots + a^n\vartheta_n = \vartheta^j + a^p\vartheta_p \end{aligned} \quad (4.64)$$

where $a \in \mathbb{R}$ is a solution path parameter for the non-linear problem. According to Einstein's notation, p is a dummy index that implicitly stands for summation over the range $[1, n]$. By replacing Eqs. 4.64 within the non-linear problem, Eq. 4.63 reads:

$$\mathbf{R}(\Theta^j + a^p\Theta_p; \vartheta^j + a^p\vartheta_p) = 0 \quad (4.65)$$

Its n -order Taylor series expansion about the point $(\Theta; \vartheta)^j$ is, then:

$$\begin{aligned} &\mathbf{R}(\Theta^j; \vartheta^j) + \frac{\partial \mathbf{R}}{\partial \Theta} \Big|_j a^p \Theta_p + \frac{\partial \mathbf{R}}{\partial \vartheta} \Big|_j a^p \vartheta_p + \\ &+ \frac{1}{2} \left[\frac{\partial^2 \mathbf{R}}{\partial \Theta^2} \Big|_j a^p \Theta_p a^s \Theta_s + \frac{\partial^2 \mathbf{R}}{\partial \vartheta^2} \Big|_j a^p \vartheta_p a^s \vartheta_s + \frac{\partial^2 \mathbf{R}}{\partial \Theta \partial \vartheta} \Big|_j a^p \Theta_p a^s \vartheta_s \right] + \\ &+ \frac{1}{3!} \left[\frac{\partial^3 \mathbf{R}}{\partial \Theta^3} \Big|_j a^p \Theta_p a^s \Theta_s a^q \Theta_q + \frac{\partial^3 \mathbf{R}}{\partial \vartheta^3} \Big|_j a^p \vartheta_p a^s \vartheta_s a^q \vartheta_q + \right. \\ &\left. + \frac{\partial^3 \mathbf{R}}{\partial \Theta^2 \partial \vartheta} \Big|_j a^p \Theta_p a^s \Theta_s a^q \vartheta_q + \frac{\partial^3 \mathbf{R}}{\partial \Theta \partial \vartheta^2} \Big|_j a^p \Theta_p a^s \vartheta_s a^q \vartheta_q \right] + \dots = 0 \end{aligned} \quad (4.66)$$

where $\mathbf{R}(\Theta^j; \vartheta^j) = 0$ since $(\Theta; \vartheta)^j$ belongs to the solution domain. Eq. 4.66 can be re-arranged in the following manner:

$$\begin{aligned}
\mathbf{R}(\Theta; \vartheta) &= a \left[\frac{\partial \mathbf{R}}{\partial \Theta} \Big|_j \Theta_1 + \frac{\partial \mathbf{R}}{\partial \vartheta} \Big|_j \vartheta_1 \right] + \\
&a^2 \left\{ \frac{\partial \mathbf{R}}{\partial \Theta} \Big|_j \Theta_2 + \frac{\partial \mathbf{R}}{\partial \vartheta} \Big|_j \vartheta_2 + \frac{1}{2} \left[\frac{\partial^2 \mathbf{R}}{\partial \Theta^2} \Big|_j \Theta_1^2 + \frac{\partial^2 \mathbf{R}}{\partial \vartheta^2} \Big|_j \vartheta_1^2 + \frac{\partial^2 \mathbf{R}}{\partial \Theta \partial \vartheta} \Big|_j \Theta_1 \vartheta_1 \right] \right\} + \\
&a^3 \left[\frac{\partial \mathbf{R}}{\partial \Theta} \Big|_j \Theta_3 + \frac{\partial \mathbf{R}}{\partial \vartheta} \Big|_j \vartheta_3 - \mathcal{F}_3(\Theta_1, \Theta_2; \vartheta_1, \vartheta_2) \right] + \dots + \\
&+ a^n \left[\frac{\partial \mathbf{R}}{\partial \Theta} \Big|_j \Theta_n + \frac{\partial \mathbf{R}}{\partial \vartheta} \Big|_j \vartheta_n - \mathcal{F}_n(\Theta_1, \Theta_2, \dots, \Theta_{n-1}; \vartheta_1, \vartheta_2, \dots, \vartheta_{n-1}) \right] = 0
\end{aligned} \tag{4.67}$$

where, for a give order p of a , \mathcal{F}_p is a function of the unknowns Θ_k and ϑ_k up to the order $p - 1$. Eq. 4.67 must be valid for a generic value of a , therefore, the following linear system of N equations in $N + 1$ unknowns:

$$\frac{\partial \mathbf{R}}{\partial \Theta} \Big|_j \Theta_p + \frac{\partial \mathbf{R}}{\partial \vartheta} \Big|_j \vartheta_p = \mathcal{F}_p(\Theta_1, \Theta_2, \dots, \Theta_{p-1}; \vartheta_1, \vartheta_2, \dots, \vartheta_{p-1}) \tag{4.68}$$

is obtained from each term a^p . \mathcal{F}_p is known once the linear system derived from the orders lower than the p -th one have been solved. The problem in Eq. 4.68 is not well posed and a complementary condition for each expansion term p should be provided. This complementary condition is obtained from the definition of the path parameter a as a pseudo-arc-length by projecting the solution increment $(\Theta; \vartheta)^{j+1} = (\Theta - \Theta^j; \vartheta - \vartheta^j)$ over the tangent direction $(\Theta_1; \vartheta_1)$:

$$a = (\Theta - \Theta^j)^T \Theta_1 + (\vartheta - \vartheta^j) \vartheta_1 \tag{4.69}$$

The following equations are, then, obtained by replacing Eqs. 4.64 within Eq. 4.69:

$$\begin{aligned}
\|\Theta_1\|^2 + \vartheta_1^2 &= 1 \\
\Theta_p^T \Theta_1 + \vartheta_p \vartheta_1 &= 0 \quad p \geq 2
\end{aligned} \tag{4.70}$$

being $\|\square\|$ the Euclidean norm. As a concluding remark, it should be noted that at each step j , the matrix $\frac{\partial \mathbf{R}}{\partial \Theta} \Big|_j$ is the same for each expansion term p which allows to save a relevant amount of calculation time. Once the values Θ_p and ϑ_p have been all computed, the path solution at step $j + 1$ is obtained by Eq. 4.64. Finally, the maximum value of path parameter a is adopted with the same principle as in

Cochelin et al. Cochelin et al. (2007):

$$a = \left(\epsilon \frac{\|\Theta_1\|}{\|\Theta_p\|} \right)^{\frac{1}{p-1}}, \quad (4.71)$$

where ϵ is a precision parameter, which is determined by the user.

Fourier model for sandwich instability

Contents

5.1	Introduction	96
5.2	The microscopical model	99
5.2.1	Kinematics	99
5.2.2	Strain-displacement relation and constitutive laws	102
5.2.3	Weak form of the microscopical model	103
5.2.4	Governing equations of microscopical model	108
5.3	The macroscopical model	108
5.3.1	The general methodology	108
5.3.2	Internal work of the core	110
5.3.3	Internal work of the skins	113
5.3.4	Governing equations of macroscopical model	115
5.4	Discretization	115
5.5	Numerical results	117
5.5.1	Validation and mesh convergence study	118
5.5.2	Antisymmetrical wrinkling	120
5.5.3	Symmetrical wrinkling	123
5.6	Conclusion	128

Abstract

This Chapter presents a Fourier-related double scale analysis to study the instability phenomena of sandwich plates. By expanding the displacement field into Fourier series, the sandwich plate model proposed by Yu et al. (2015), using the classical plate theory in the skins and high-order kinematics in the core, is transformed into a new Fourier-based reduced two-dimensional sandwich plate model with the slowly varying Fourier coefficients as macroscopic unknowns. The resulting nonlinear equations are solved by the Asymptotic Numerical Method (ANM), which is very efficient and reliable to capture the bifurcation point and the post-buckling

path in wrinkling analyses. Both antisymmetrical and symmetrical wrinkling for sandwich plates under uni-axial and equi-biaxial compressive loads are studied and the numerical results demonstrate that the Fourier-based finite element model can accurately yet efficiently predict wrinkling patterns and critical loads, especially when dealing with wrinkling phenomena with extremely large wavenumbers.

Present Chapter corresponds to the published research paper (Huang et al., 2017) [Computer Methods in Applied Mechanics and Engineering, 318: 270-295, 2017.]. A self-consistent notation is adopted.

Keywords: Sandwich plate, Fourier series, Instability, Wrinkling, Asymptotic Numerical Method.

5.1 Introduction

During recent decades, sandwich structures are widely used in aerospace, automotive and civil engineering fields. For the typical sandwich structures, the skins are usually made of high-strength materials such as lightweight metal alloys so that the skins can carry almost all the axial loads, whereas the core can be made of low-density materials such as carbon, balsa or plastic materials to transmit the transverse normal and shear loads. Thus very attractive properties in terms of light weight and high flexural stiffness can be obtained within this principle of construction. When designing this kind of structures, one of the major concerns belongs to the buckling phenomena (global and local instabilities). Hence, this Chapter aims to accurately and efficiently predict the critical load and describe the structural responses in these phenomena.

Instability phenomena in sandwich structures can be generally divided into three main classes: global buckling, antisymmetrical wrinkling and symmetrical wrinkling, see Allen (1969). Over the last years, many works have been devoted to investigate and characterise the global and local instabilities of sandwich structures Léotoing et al. (2002a); Aiello and Ombres (1997); Ji and Waas (2007, 2010); Douville and Le Grogneq (2013); Sad Saoud and Le Grogneq (2014); Noor et al. (1996); Reddy (2004b); Dawe and Yuan (2001); Yuan and Dawe (2001); Léotoing et al. (2002b). Generally, the skins are modelled by nonlinear beams or plates due to their thinness. For the core, there are many different ways to model it depending on the type of the core material and its deformability. The simplest model is the so-called one-parameter foundation that only considers the transversal core stiffness.

Then improvement is made in the two-parameter model by accounting for both the compressibility of the core and the shear effect between the skin and the core Aiello and Ombres (1997). These models can be only practical on the condition that the core thickness is relatively thick compared to the skins thickness, i.e., the interaction between the two skins is negligible. To adequately describe the kinematic behavior in the core, the core can be modeled as a three-dimensional (3D) continuous solid. On the basis of the elastic bifurcation theory in the 3D framework, the closed-form analytical expressions of the critical loads and the related buckling modes (global and local buckling) are recently presented for sandwich plates and beams, see Duville and Le Grogneq (2013); Sad Saoud and Le Grogneq (2014). However, from the numerical aspects, when the 3D solid is discretized by hexahedral elements Madenci and Guven (2006), very fine meshes are needed to capture the response due to the small-scale wrinkles and the relatively large thickness, which leads to large computational cost. Thus, to accurately characterise sandwich structures' mechanical behavior, including buckling phenomena, in a computation-cost-effective way, many works are resorted to the two-dimensional (2D) modelling framework, where the 3D problem reduces to the 2D problem by making suitable assumptions with respect to the displacement or stress field in the thickness direction. Generally these works can be classified into two main approaches: the equivalent single layer (ESL) approach and the layer-wise (LW) one, see Reddy (2004b). For both approaches, various additional functions are usually introduced (such as linear function (Kreja et al. (1997); Zhang et al. (2016a,b)), cubic function (Reddy (1984); Ferreira (2005)), sinusoidal function (Touratier (1991); Vidal and Polit (2009)), exponential function (Karama et al. (2003)) and Legendre's polynomials (D'Ottavio and Polit (2015)) etc.) to cooperate for multilayer structures with different geometrical, material properties under various loading cases over the years. Comprehensive assessments and comparisons on various approaches and models used for modelling multilayered plates as well as sandwich plates can be found in Reddy (2004b) and Carrera (2003b). From the aspect of numerical simulation, it is necessary to balance accuracy and computation cost for a certain model when handling buckling problems in multilayered plates or sandwich plates.

Based on the Carrera Unified Formulation (CUF), Carrera and Miglioretti (2012) proposed the so-called Best Theory Diagram to select the appropriate unknown variables upon application of genetic algorithms. Recently, D'Ottavio et al. (2016) proposed an equally clever high order LW model named sublaminated generalized unified formulation (S-GUF), in framework of which several kinematic models, e.g. high order models in Léotoing et al. (2002a); Dawe and Yuan (2001); Yuan and

Dawe (2001); Léotoing et al. (2002b), were systematically investigated and assessed and benchmark solutions were also presented for global and local buckling in sandwich structures. They showed that the quadratic approximation as in Léotoing et al. (2002a,b) for the transverse displacement in the core is the minimum requirement to well characterise the local buckling instability and thus leads to few variables. As an extension work of Léotoing et al. (2002a,b), Hu et al. (2009a) proposed a novel one-dimensional finite element considering the axial stiffness of the core, which yielded accurate results with a considerable reduction of computational cost for the global and local buckling of sandwich beams. In a following paper, Hu et al. (2008) also reviewed several theories for sandwich beams. As an extension work of Hu et al. (2009a), Yu et al. (2015) adopted the similar assumptions in Léotoing et al. (2002a,b) to develop a novel 2D finite element for instability analyses of sandwich plates, which has only nine variables and leads to fairly accurate and efficient solutions compared with the numerical results via the 3D finite element method (FEM). However, even for this 2D finite element, intensive computation efforts are still needed to accurately characterise the buckling responses of sandwich plates when the wrinkling wavelength is very small and the wavenumber is extremely large. Furthermore, the nonlinear calculation path is difficult to be controlled because too many solution paths exist around the useful one and the nonlinear system may be sensitive to the perturbation. Thus, it is necessary to develop highly efficient models to accurately and quickly describe instability phenomena in sandwich plates.

Recently, an effective double scale approach has been proposed based on the Fourier series with slowly varying coefficients (Damil and Potier-Ferry (2010, 2008)). In this approach, exploiting the periodic nature of the instability pattern, the kinematic unknowns (addressed as “microscopic model”) are expanded into the form of the Fourier series, which leads to a new problem with Fourier coefficients as new unknowns (addressed as “macroscopic model”) that vary much more slowly than the original unknowns. This approach is similar to the Landau-Ginzburg technique but more robust than it, see Damil and Potier-Ferry (2010). So far, the Fourier-related approach has been successfully applied for instability phenomena in different kinds of structures such as the elastic beams on nonlinear Winkler foundation (Damil and Potier-Ferry (2010); Mhada et al. (2012)), sandwich beams (Liu et al. (2012); Mhada et al. (2013); Liu et al. (2016)), thin metal sheets (Damil et al. (2013, 2014); Huang et al. (2015); Attipou et al. (2015)) and film-substrate systems (Huang et al. (2017b)). Numerical results verified that the approach has great advantages in reducing computational source and simplifying nonlinear calculation. As a reduced

order model, the Fourier-based model becomes inaccurate near the boundary. It can be overcome by using the Arlequin method (Ben Dhia (1998); Ben Dhia and Rateau (2005)), which couples the full model used in the region of boundary conditions and the macroscopic model in the bulk, see Hu et al. (2011); Yu et al. (2013). In this Chapter, based on the Fourier-related approach and the 2D microscopic finite element proposed by Yu et al. (2015), an effective 2D Fourier-based finite element is developed to study the symmetrical and antisymmetrical wrinkling phenomena in sandwich plates. The proposed 2D finite element model permits to capture the wrinkling evolution with much less degrees of freedom (DOFs) compared with the 2D microscopic model of Yu et al. (2015) and the 3D FEM solutions by commercial code ABAQUS. The obtained nonlinear system is solved by the Asymptotic Numerical Method (ANM), see Damil and Potier-Ferry (1990) and Cochelin et al. (1994). The ANM is an efficient and robust path following technique in the presence of bifurcation compared to the classical nonlinear solution methods such as the Newton-Raphson or the arc-length (Riks) method. Numerical examples are performed to assess the 2D Fourier-based finite element model and very accurate results are obtained with significant reduction in computational cost.

The Chapter is structured as follows. In Section 5.2, the same kinematic assumptions as Yu et al. (2015) are used to derive a 2D microscopic model for sandwich plates. Then, on the basis of the 2D microscopic model and using the Fourier-related approach, the weak form of governing equations of the Fourier-based 2D macroscopic model is derived in Section 5.3. In Section 5.4, the finite element method is used to discretize the proposed 2D Fourier-based model. In Section 5.5, numerical examples relating to the symmetrical and antisymmetrical wrinkling are performed to examine and assess the validation and efficiency of the 2D Fourier-based finite element model.

5.2 The microscopical model

5.2.1 Kinematics

In this Chapter, a sandwich plate is considered as a three-layered panel with a soft core and two stiff skins, as shown in Fig. 5.1: x and y are the in-plane coordinates, z the transverse coordinate, L_x the in-plane length and L_y the in-plane width. The thickness of the top and bottom skin h_s is assumed to be the same for simplicity. The core and total thickness are h_c and h_t , respectively.

The same kinematics proposed by Yu et al. (2015) are used for the considered

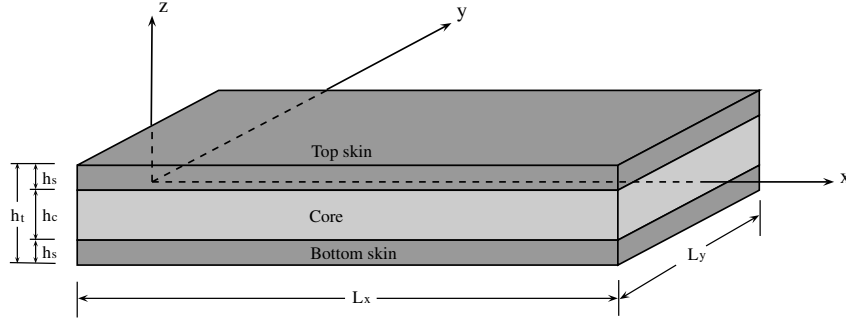


Figure 5.1: Sketch of the sandwich plate.

sandwich plate, where a high-order kinematic is used in the core and the classical plate theory (CPT) for the skins:

$$\text{Top skin} \begin{cases} \mathcal{U}^t(x, y, z) = u^t(x, y) - \left(z - \frac{h_s + h_c}{2}\right) \frac{\partial \mathcal{W}^t(x, y, z)}{\partial x}, \\ \mathcal{V}^t(x, y, z) = v^t(x, y) - \left(z - \frac{h_s + h_c}{2}\right) \frac{\partial \mathcal{W}^t(x, y, z)}{\partial y}, \\ \mathcal{W}^t(x, y, z) = w^t(x, y). \end{cases} \quad \frac{h_c}{2} < z \leq \frac{h_t}{2} \quad (5.1)$$

$$\text{Core} \begin{cases} \mathcal{U}^c(x, y, z) = u^c(x, y) + z\alpha(x, y) + z^2 u^*(x, y) + z^3 \alpha^*(x, y), \\ \mathcal{V}^c(x, y, z) = v^c(x, y) + z\beta(x, y) + z^2 v^*(x, y) + z^3 \beta^*(x, y), \\ \mathcal{W}^c(x, y, z) = w^c(x, y) + z\varphi(x, y) + z^2 \psi(x, y). \end{cases} \quad -\frac{h_c}{2} < z \leq \frac{h_c}{2} \quad (5.2)$$

$$\text{Bottom skin} \begin{cases} \mathcal{U}^b(x, y, z) = u^b(x, y) - \left(z + \frac{h_s + h_c}{2}\right) \frac{\partial \mathcal{W}^b(x, y, z)}{\partial x}, \\ \mathcal{V}^b(x, y, z) = v^b(x, y) - \left(z + \frac{h_s + h_c}{2}\right) \frac{\partial \mathcal{W}^b(x, y, z)}{\partial y}, \\ \mathcal{W}^b(x, y, z) = w^b(x, y), \end{cases} \quad -\frac{h_t}{2} < z \leq -\frac{h_c}{2} \quad (5.3)$$

in which, the superscripts t , b and c represent the top, bottom and core layers, respectively. The symbols \mathcal{U} and \mathcal{V} denote the in-plane displacements in the x and y directions and \mathcal{W} denotes the transverse displacement in the z direction, and u , v and w , respectively, refer to the in-plane and transversal displacements of the neutral plane in each layer. The unknown functions α , u^* , α^* , β , v^* , β^* , φ and ψ are enrichment functions with respect to the classical zig-zag theory. One notes that both symmetrical and antisymmetrical instability modes can be described by this kinematic assumption, because the displacement field is separately assumed for

each layer and a quadratic through-the-thickness function is used for the transverse displacement of the core layer. For the present, there are seventeen unknowns in this kinematic assumption.

As the same assumption in Hu et al. (2009a); Liu et al. (2012); Yu et al. (2015); Léotoing et al. (2002b), a linear shear stress in the thickness direction is considered in the core layer, which can well approximate the actual shear stress distribution in both antisymmetrical and symmetrical instability modes. Thus the total number of unknowns can firstly be reduced with the following relations:

$$\begin{cases} \alpha^* = -\frac{1}{3}\psi_{,x}, \\ \beta^* = -\frac{1}{3}\psi_{,y}, \end{cases} \quad (5.4)$$

where the “ $,x$ ” stands for $\frac{\partial}{\partial x}$. As the skins and the core are assumed to be perfectly bounded to each other, the displacements at the interface between the skins (top or bottom) and the core should satisfy the continuity conditions

$$\begin{cases} \mathcal{W}^t(x, y, \frac{h_c}{2}) = \mathcal{W}^c(x, y, \frac{h_c}{2}), \\ \mathcal{W}^b(x, y, -\frac{h_c}{2}) = \mathcal{W}^c(x, y, -\frac{h_c}{2}), \\ \mathcal{V}^t(x, y, \frac{h_c}{2}) = \mathcal{V}^c(x, y, \frac{h_c}{2}), \\ \mathcal{V}^b(x, y, -\frac{h_c}{2}) = \mathcal{V}^c(x, y, -\frac{h_c}{2}), \\ \mathcal{W}^t(x, y, \frac{h_c}{2}) = \mathcal{W}^c(x, y, \frac{h_c}{2}), \\ \mathcal{W}^b(x, y, -\frac{h_c}{2}) = \mathcal{W}^c(x, y, -\frac{h_c}{2}). \end{cases} \quad (5.5)$$

By substituting Eqs. (5.4) and (5.5) into Eqs. (5.1)-(5.3), one gets the following relations:

$$\begin{cases} w^c = \frac{1}{2}(w^t + w^b) - \frac{h_c^2}{4}\psi, \\ \varphi = \frac{1}{h_c}(w^t - w^b), \\ \alpha = \frac{h_s}{2h_c}(w^t_{,x} + w^b_{,x}) + \frac{1}{h_c}(u^t - u^b) + \frac{h_c^2}{12}\psi_{,x}, \\ \beta = \frac{h_s}{2h_c}(w^t_{,y} + w^b_{,y}) + \frac{1}{h_c}(v^t - v^b) + \frac{h_c^2}{12}\psi_{,y}, \\ u^c = \frac{h_s}{4}(w^t_{,x} - w^b_{,x}) + \frac{1}{2}(u^t + u^b) - \frac{h_c^2}{4}u^*, \\ v^c = \frac{h_s}{4}(w^t_{,y} - w^b_{,y}) + \frac{1}{2}(v^t + v^b) - \frac{h_c^2}{4}v^*. \end{cases} \quad (5.6)$$

Finally, the unknowns are reduced from seventeen to nine: $u^t, u^b, v^t, v^b, u^*, v^*, w^t, w^b, \psi$.

5.2.2 Strain-displacement relation and constitutive laws

The constitutive and geometric equations are determined by the following hypotheses:

- the material behavior is isotropic in each layer and meets the Hooke's law;
- the geometrical non-linearity is considered in the skins only with moderate rotation and the strain-displacement relationship is described by the Von Karman strain;
- the core undergoes small displacements.

Thus, the strain-displacement relations for the skins and the core can be expressed as:

$$\left\{ \begin{array}{l} \epsilon_{xx}^s = \mathcal{U}_{,x}^s + \frac{1}{2}(\mathcal{W}_{,x}^s)^2, \\ \epsilon_{yy}^s = \mathcal{V}_{,y}^s + \frac{1}{2}(\mathcal{W}_{,y}^s)^2, \\ 2\epsilon_{xy}^s = \mathcal{U}_{,y}^s + \mathcal{V}_{,x}^s + \mathcal{W}_{,x}^s \mathcal{W}_{,y}^s, \\ \epsilon_{xx}^c = \mathcal{U}_{,x}^c, \\ \epsilon_{yy}^c = \mathcal{V}_{,y}^c, \\ \epsilon_{zz}^c = \mathcal{W}_{,z}^c, \\ 2\epsilon_{xy}^c = \mathcal{U}_{,y}^c + \mathcal{V}_{,x}^c, \\ 2\epsilon_{yz}^c = \mathcal{V}_{,z}^c + \mathcal{W}_{,y}^c, \\ 2\epsilon_{xz}^c = \mathcal{U}_{,z}^c + \mathcal{W}_{,x}^c, \end{array} \right. \quad (5.7)$$

in which the superscript s denotes either the top or bottom skin for brevity. For the skin layers, the stress-strain relationships are

$$\left\{ \begin{array}{l} \sigma_{xx}^s \\ \sigma_{yy}^s \\ \sigma_{xy}^s \end{array} \right\} = \frac{E_s}{1 - \nu_s^2} \begin{bmatrix} 1 & \nu_s & 0 \\ \nu_s & 1 & 0 \\ 0 & 0 & \frac{(1-\nu_s)}{2} \end{bmatrix} \left\{ \begin{array}{l} \epsilon_{xx}^s \\ \epsilon_{yy}^s \\ 2\epsilon_{xy}^s \end{array} \right\}, \quad (5.8)$$

while the stress-strain relations for the core can be expressed as:

$$\left\{ \begin{array}{l} \sigma_{xx}^c \\ \sigma_{yy}^c \\ \sigma_{zz}^c \\ \sigma_{xy}^c \\ \sigma_{yz}^c \\ \sigma_{xz}^c \end{array} \right\} = \begin{bmatrix} C_{11} & C_{12} & C_{13} & 0 & 0 & 0 \\ C_{12} & C_{22} & C_{23} & 0 & 0 & 0 \\ C_{13} & C_{23} & C_{33} & 0 & 0 & 0 \\ 0 & 0 & 0 & C_{44} & 0 & 0 \\ 0 & 0 & 0 & 0 & C_{55} & 0 \\ 0 & 0 & 0 & 0 & 0 & C_{66} \end{bmatrix} \left\{ \begin{array}{l} \epsilon_{xx}^c \\ \epsilon_{yy}^c \\ \epsilon_{zz}^c \\ 2\epsilon_{xy}^c \\ 2\epsilon_{yz}^c \\ 2\epsilon_{xz}^c \end{array} \right\}, \quad (5.9)$$

in which

$$\begin{aligned} C_{11} = C_{22} = C_{33} &= \lambda_c + 2G_c, \\ C_{12} = C_{13} = C_{23} &= \lambda_c, \\ C_{44} = C_{55} = C_{66} &= G_c, \end{aligned} \quad (5.10)$$

and

$$\lambda_c = \frac{E_c \nu_c}{(1 + \nu_c)(1 - 2\nu_c)}, \quad G_c = \frac{E_c}{2(1 + \nu_c)}. \quad (5.11)$$

In Eqs. (5.8–5.11), E and ν are respectively the Young's modulus and the Poisson's ratio, λ the Lamé's first parameter and G the shear modulus. Eqs. (5.8) and (5.9) can be rewritten in the following compact form:

$$\begin{aligned} \boldsymbol{\sigma}_s &= \mathbf{C}_s \boldsymbol{\epsilon}_s, \\ \boldsymbol{\sigma}_c &= \mathbf{C}_c \boldsymbol{\epsilon}_c. \end{aligned} \quad (5.12)$$

5.2.3 Weak form of the microscopical model

The weak form of the governing equations is obtained by the Principal of Virtual Work (PVW):

$$\delta P_{int} = \delta P_{ext} \quad (5.13)$$

where δ stands for a virtual variation, P_{int} is the internal work and P_{ext} the external work. The internal virtual work is expressed as:

$$\delta P_{int} = \delta P_{int}^c + \delta P_{int}^t + \delta P_{int}^b = \int_{V_c} \delta \boldsymbol{\epsilon}_c^T \boldsymbol{\sigma}_c dV_c + \int_{V_t} \delta \boldsymbol{\epsilon}_t^T \boldsymbol{\sigma}_t dV_t + \int_{V_b} \delta \boldsymbol{\epsilon}_b^T \boldsymbol{\sigma}_b dV_b, \quad (5.14)$$

where the superscript T represents transposition of a matrix. The volumes $V_t = H_t \times \Omega$, $V_c = H_c \times \Omega$ and $V_b = H_b \times \Omega$ stand for top skin, core and bottom skin integration domains where $H_t = \left\{ z : \frac{h_c}{2} \leq z \leq \frac{h_t}{2} \right\}$, $H_c = \left\{ z : -\frac{h_c}{2} \leq z \leq \frac{h_c}{2} \right\}$, $H_b = \left\{ z : -\frac{h_t}{2} \leq z \leq -\frac{h_c}{2} \right\}$ and $\Omega = [0, L_x] \times \left[-\frac{L_y}{2}, \frac{L_y}{2} \right]$. By taking into account of the strain-displacement and stress-strain relationships, one can easily get the unknown vector of the microscopic model:

$$\begin{aligned} \langle \mathbf{q}_f \rangle = \left\langle \begin{array}{cccccccccccc} u^t & u^t_{,x} & u^t_{,y} & v^t & v^t_{,x} & v^t_{,y} & u^b & u^b_{,x} & u^b_{,y} & v^b & v^b_{,x} & v^b_{,y} \\ u^* & u^*_{,x} & u^*_{,y} & v^* & v^*_{,x} & v^*_{,y} & w^t & w^t_{,x} & w^t_{,xx} & w^t_{,y} & w^t_{,yy} & w^t_{,xy} \\ w^b & w^b_{,x} & w^b_{,xx} & w^b_{,y} & w^b_{,yy} & w^b_{,xy} & \psi & \psi_{,x} & \psi_{,xx} & \psi_{,y} & \psi_{,yy} & \psi_{,xy} \end{array} \right\rangle, \end{aligned} \quad (5.15)$$

Table 5.1: Non-zero elements of the elasticity matrix $\mathbf{C}^c \in \mathbb{R}^{30 \times 30}$.

(1,1)= $h_1 E'$	(1,4)= $h_1 \lambda$	(1,12)= $h_3 E'$	(1,16)= $h_3 \lambda$	(1,25)= $h_1 \lambda$
(2,2)= $h_1 G_c$	(2,3)= $h_1 G_c$	(2,13)= $h_3 G_c$	(2,15)= $h_3 G_c$	
(3,2)= $h_1 G_c$	(3,3)= $h_1 G_c$	(3,13)= $h_3 G_c$	(3,15)= $h_3 G_c$	
(4,1)= $h_1 \lambda$	(4,4)= $h_1 E'$	(4,12)= $h_3 \lambda$	(4,16)= $h_3 \lambda$	(4,25)= $h_1 \lambda$
(5,5)= $h_1 G_c$	(5,17)= $3h_3 G_c$	(5,23)= $h_1 G_c$	(5,29)= $h_3 G_c$	
(6,6)= $h_3 E'$	(6,10)= $h_3 \lambda$	(6,18)= $h_5 E'$	(6,22)= $h_5 \lambda$	(6,28)= $2h_3 \lambda$
(7,7)= $h_3 G_c$	(7,9)= $h_3 G_c$	(7,19)= $h_5 G_c$	(7,21)= $h_5 G_c$	
(8,8)= $h_1 G_c$	(8,20)= $3h_3 G_c$	(8,24)= $h_1 G_c$	(8,30)= $h_3 G_c$	
(9,7)= $h_3 G_c$	(9,9)= $h_3 G_c$	(9,19)= $h_5 G_c$	(9,21)= $h_5 G_c$	
(10,6)= $h_3 \lambda$	(10,10)= $h_3 E'$	(10,18)= $h_5 \lambda$	(10,22)= $h_5 E'$	(10,28)= $2h_3 \lambda$
(11,11)= $4h_3 G_c$	(11,26)= $2h_3 G_c$			
(12,1)= $h_3 E'$	(12,4)= $h_3 \lambda$	(12,12)= $h_5 E'$	(12,16)= $h_5 \lambda$	(12,25)= $h_3 \lambda$
(13,2)= $h_3 G_c$	(13,3)= $h_3 G_c$	(13,13)= $h_5 G_c$	(13,15)= $h_5 G_c$	
(14,14)= $4h_3 G_c$	(14,27)= $2h_3 G_c$			
(15,2)= $h_3 G_c$	(15,3)= $h_3 G_c$	(15,13)= $h_5 G_c$	(15,15)= $h_5 G_c$	
(16,1)= $h_3 \lambda$	(16,4)= $h_3 E'$	(16,12)= $h_5 \lambda$	(16,16)= $h_5 E'$	(16,25)= $h_3 \lambda$
(17,5)= $3h_3 G_c$	(17,17)= $9h_5 G_c$	(17,23)= $3h_3 G_c$	(17,29)= $3h_5 G_c$	
(18,6)= $h_5 E'$	(18,10)= $h_5 \lambda$	(18,18)= $h_7 E'$	(18,22)= $h_7 \lambda$	(18,28)= $2h_5 \lambda$
(19,7)= $h_5 G_c$	(19,9)= $h_5 G_c$	(19,19)= $h_7 G_c$	(19,21)= $h_7 G_c$	
(20,8)= $3h_3 G_c$	(20,20)= $9h_5 G_c$	(20,24)= $3h_3 G_c$	(20,30)= $3h_5 G_c$	
(21,7)= $h_5 G_c$	(21,9)= $h_5 G_c$	(21,19)= $h_7 G_c$	(21,21)= $h_7 G_c$	
(22,6)= $h_5 \lambda$	(22,10)= $h_5 E'$	(22,18)= $h_7 \lambda$	(22,22)= $h_7 E'$	(22,28)= $2h_5 \lambda$
(23,5)= $h_1 G_c$	(23,17)= $3h_3 G_c$	(23,23)= $h_1 G_c$	(23,29)= $h_3 G_c$	
(24,8)= $h_1 G_c$	(24,20)= $3h_3 G_c$	(24,24)= $h_1 G_c$	(24,30)= $h_3 G_c$	
(25,1)= $h_1 \lambda$	(25,4)= $h_1 \lambda$	(25,12)= $h_3 \lambda$	(25,16)= $h_3 \lambda$	(25,25)= $h_1 E'$
(26,11)= $2h_3 G_c$	(26,26)= $h_3 G_c$			
(27,14)= $2h_3 G_c$	(27,27)= $h_3 G_c$			
(28,6)= $2h_3 \lambda$	(28,10)= $2h_3 \lambda$	(28,18)= $2h_5 \lambda$	(28,22)= $2h_5 \lambda$	(28,28)= $4h_3 E'$
(29,5)= $h_3 G_c$	(29,17)= $3h_5 G_c$	(29,23)= $h_3 G_c$	(29,29)= $h_5 G_c$	
(30,8)= $h_3 G_c$	(30,20)= $3h_5 G_c$	(30,24)= $h_3 G_c$	(30,30)= $h_5 G_c$	

$$E' = \lambda + 2G_c, \quad h_1 = h_c, \quad h_3 = \frac{h_c^3}{12}, \quad h_5 = \frac{h_c^5}{80}, \quad h_7 = \frac{h_c^7}{448}.$$

Table 5.2: Non-zero elements of the transformation matrix $[\mathbf{R}_f^c] \in \mathbb{R}^{30 \times 36}$.

$(1,2)=\frac{1}{2}$	$(1,8)=\frac{1}{2}$	$(1,14)=-\frac{h_c^2}{4}$	$(1,21)=\frac{h_s}{4}$	$(1,27)=-\frac{h_s}{4}$
$(2,3)=\frac{1}{2}$	$(2,9)=\frac{1}{2}$	$(2,15)=-\frac{h_c}{4}$	$(2,24)=\frac{h_s}{4}$	$(2,30)=-\frac{h_s}{4}$
$(3,5)=\frac{1}{2}$	$(3,11)=\frac{1}{2}$	$(3,17)=-\frac{h_c^2}{4}$	$(3,24)=\frac{h_s}{4}$	$(3,30)=-\frac{h_s}{4}$
$(4,6)=\frac{1}{2}$	$(4,12)=\frac{1}{2}$	$(4,18)=-\frac{h_c^2}{4}$	$(4,23)=\frac{h_s}{4}$	$(4,29)=-\frac{h_s}{4}$
$(5,1)=\frac{1}{h_c}$	$(5,7)=-\frac{1}{h_c}$	$(5,20)=\frac{h_s}{2h_c}$	$(5,26)=\frac{h_s}{2h_c}$	$(5,32)=\frac{h_c^2}{12}$
$(6,2)=\frac{1}{h_c}$	$(6,8)=-\frac{1}{h_c}$	$(6,21)=\frac{h_s}{2h_c}$	$(6,27)=\frac{h_s}{2h_c}$	$(6,33)=\frac{h_c^2}{12}$
$(7,3)=\frac{1}{h_c}$	$(7,9)=-\frac{1}{h_c}$	$(7,24)=\frac{h_s}{2h_c}$	$(7,30)=\frac{h_s}{2h_c}$	$(7,36)=\frac{h_c^2}{12}$
$(8,4)=\frac{1}{h_c}$	$(8,10)=-\frac{1}{h_c}$	$(8,22)=\frac{h_s}{2h_c}$	$(8,28)=\frac{h_s}{2h_c}$	$(8,34)=\frac{h_c^2}{12}$
$(9,5)=\frac{1}{h_c}$	$(9,11)=-\frac{1}{h_c}$	$(9,24)=\frac{h_s}{2h_c}$	$(9,30)=\frac{h_s}{2h_c}$	$(9,36)=\frac{h_c^2}{12}$
$(10,6)=\frac{1}{h_c}$	$(10,12)=-\frac{1}{h_c}$	$(10,23)=\frac{h_s}{2h_c}$	$(10,29)=\frac{h_s}{2h_c}$	$(10,35)=\frac{h_c^2}{12}$
$(11,13)=1$	$(12,14)=1$	$(13,15)=1$	$(14,16)=1$	$(15,17)=1$
$(16,18)=1$	$(17,32)=-\frac{1}{3}$	$(18,33)=-\frac{1}{3}$	$(19,36)=-\frac{1}{3}$	$(20,34)=-\frac{1}{3}$
$(21,36)=-\frac{1}{3}$	$(22,35)=-\frac{1}{3}$	$(23,20)=\frac{1}{2}$	$(23,26)=\frac{1}{2}$	$(23,32)=-\frac{1}{3}$
$(24,22)=\frac{1}{2}$	$(24,28)=\frac{1}{2}$	$(24,34)=-\frac{h_c^2}{4}$	$(25,19)=\frac{1}{h_c}$	$(25,25)=-\frac{1}{h_c}$
$(26,20)=\frac{1}{h_c}$	$(26,26)=-\frac{1}{h_c}$	$(27,22)=\frac{1}{h_c}$	$(27,28)=-\frac{1}{h_c}$	$(28,31)=1$
$(29,32)=1$	$(30,34)=1$			

kinematic field of the top skin as example) finally read

$$\begin{cases} \epsilon_{xx}^s = u_{,x}^s - (z - \frac{h_s + h_c}{2})w_{,xx}^s + \frac{1}{2}(w_{,x}^s)^2, \\ \epsilon_{yy}^s = v_{,y}^s - (z - \frac{h_s + h_c}{2})w_{,yy}^s + \frac{1}{2}(w_{,y}^s)^2, \\ 2\epsilon_{xy}^s = u_{,y}^s + v_{,x}^s - 2(z - \frac{h_s + h_c}{2})w_{,xy}^s + w_{,x}^s w_{,y}^s. \end{cases} \quad (5.20)$$

Following the derivation in Section 5.2.3.1 and using Eqs. (5.8) and (5.20), the internal virtual work of the skins is:

$$\delta P_{int}^s = \int_{\Omega} \langle \delta \gamma_f^s \rangle \{ \mathbf{S}_f^s \} d\Omega, \quad (5.21)$$

where $\{\gamma_f^s\}$ and $\{\mathbf{S}_f^s\}$ are, respectively, the generalized strain and stress vector of the skins, and $\{\gamma_f^s\}$ is expressed by the unknown vector of the skins $\{\mathbf{q}_f^s\}$:

$$\{\gamma_f^s\} = \left([\mathbf{H}_f^s] + \frac{1}{2}[\mathbf{A}_f(\mathbf{q}_f^s)] \right) \{\mathbf{q}_f^s\}, \quad (5.22)$$

in which

$$[\mathbf{H}_f^s] = \begin{bmatrix} 1 & 0 & 0 & 0 & 0 & 0 & 0 & 0 & 0 \\ 0 & 0 & 0 & 1 & 0 & 0 & 0 & 0 & 0 \\ 0 & 0 & 0 & 0 & 0 & 1 & 0 & 0 & 0 \\ 0 & 0 & 0 & 0 & 0 & 0 & 0 & 1 & 0 \\ 0 & 1 & 1 & 0 & 0 & 0 & 0 & 0 & 0 \\ 0 & 0 & 0 & 0 & 0 & 0 & 0 & 0 & 1 \end{bmatrix}, \quad [\mathbf{A}_f(\mathbf{q}_f^s)] = \begin{bmatrix} 0 & 0 & 0 & 0 & w_{,x}^s & 0 & 0 & 0 & 0 \\ 0 & 0 & 0 & 0 & 0 & 0 & w_{,y}^s & 0 & 0 \\ 0 & 0 & 0 & 0 & 0 & 0 & 0 & 0 & 0 \\ 0 & 0 & 0 & 0 & 0 & 0 & 0 & 0 & 0 \\ 0 & 0 & 0 & 0 & w_{,y}^s & 0 & w_{,x}^s & 0 & 0 \\ 0 & 0 & 0 & 0 & 0 & 0 & 0 & 0 & 0 \end{bmatrix}, \quad (5.23)$$

and

$$\langle \mathbf{q}_f^s \rangle = \langle u_{,x}^s \ u_{,y}^s \ v_{,x}^s \ v_{,y}^s \ w_{,x}^s \ w_{,xx}^s \ w_{,y}^s \ w_{,yy}^s \ w_{,xy}^s \rangle. \quad (5.24)$$

Then relating the skins' unknowns $\{\mathbf{q}_f^s\}$ to the total unknowns $\{\mathbf{q}_f\}$ by a transformation matrix $[\mathbf{R}_f^s] \in \mathbb{R}^{9 \times 36}$, one gets

$$\{\mathbf{q}_f^s\} = [\mathbf{R}_f^s] \{\mathbf{q}_f\}. \quad (5.25)$$

The details of the non-zero elements of $[\mathbf{R}_f^s]$ (referred to the top skin $[\mathbf{R}_f^t]$ and the bottom skin $[\mathbf{R}_f^b]$) are listed in Table 5.3.

Table 5.3: Relevant transformation matrices for the skins, in which the non-zero elements are listed.

Matrix	Size	Value	Location
$[\mathbf{R}_f^t]$	9×36	1	(1,2)(2,3)(3,5)(4,6)(5,20)(6,21)(7,22)(8,23)(9,24)
$[\mathbf{R}_f^b]$	9×36	1	(1,8)(2,9)(3,11)(4,12)(5,26)(6,27)(7,28)(8,29)(9,30)

The generalized stress vector $\{\mathbf{S}_f^s\}$ is expressed as:

$$\{\mathbf{S}_f^s\} = [\mathbf{D}_f^s] \{\gamma_f^s\}, \quad (5.26)$$

in which the generalized elasticity matrix in the skin $[\mathbf{D}_f^s]$ reads

$$[\mathbf{D}_f^s] = \frac{E_s}{1 - \nu_s^2} \begin{bmatrix} h_s & \nu_s h_s & 0 & 0 & 0 & 0 \\ \nu_s h_s & h_s & 0 & 0 & 0 & 0 \\ 0 & 0 & \frac{h_s^3}{12} & \nu_s \frac{h_s^3}{12} & 0 & 0 \\ 0 & 0 & \nu_s \frac{h_s^3}{12} & \frac{h_s^3}{12} & 0 & 0 \\ 0 & 0 & 0 & 0 & \frac{(1-\nu_s)h_s}{2} & 0 \\ 0 & 0 & 0 & 0 & 0 & \frac{(1-\nu_s)h_s^3}{6} \end{bmatrix}. \quad (5.27)$$

The internal virtual work of a skin layer finally reads

$$\delta P_{int}^s = \int_{\Omega} \langle \delta \mathbf{q}_f \rangle [\mathbf{R}_f^s]^T \left([\mathbf{H}_f^s]^T + [\mathbf{A}_f(\mathbf{q}_f)]^T \right) \{ \mathbf{S}_f^s \} d\Omega. \quad (5.28)$$

5.2.4 Governing equations of microscopical model

The external virtual work is expressed as:

$$\delta P_{ext} = \lambda_f \int_{\Omega} \langle \delta \mathbf{q}_f \rangle \{ \mathbf{F}_f \} d\Omega, \quad (5.29)$$

where $\{ \mathbf{F}_f \}$ denotes the external load and λ_f is the load proportional parameter.

Finally the governing equation of the microscopical model reads:

$$\left\{ \begin{array}{l} \int_{\Omega} \langle \delta \mathbf{q}_f \rangle [\mathbf{R}_f^t]^T \left([\mathbf{H}_f^t]^T + [\mathbf{A}_f(\mathbf{q}_f^t)]^T \right) \{ \mathbf{S}_f^t \} + \langle \delta \mathbf{q}_f \rangle [\mathbf{R}_f^b]^T \left([\mathbf{H}_f^b]^T + [\mathbf{A}_f(\mathbf{q}_f^b)]^T \right) \{ \mathbf{S}_f^b \} \\ + \langle \delta \mathbf{q}_f \rangle [\mathbf{D}_f^c] \{ \mathbf{q}_f \} d\Omega = \lambda_f \int_{\Omega} \langle \delta \mathbf{q}_f \rangle \{ \mathbf{F}_f \} d\Omega, \\ \{ \mathbf{S}_f^t \} = [\mathbf{D}_f^t] \left([\mathbf{H}_f^t] + \frac{1}{2} [\mathbf{A}_f(\mathbf{q}_f^t)] \right) [\mathbf{R}_f^t] \{ \mathbf{q}_f \}, \\ \{ \mathbf{S}_f^b \} = [\mathbf{D}_f^b] \left([\mathbf{H}_f^b] + \frac{1}{2} [\mathbf{A}_f(\mathbf{q}_f^b)] \right) [\mathbf{R}_f^b] \{ \mathbf{q}_f \}. \end{array} \right. \quad (5.30)$$

This model permits to accurately and efficiently describe the global and local wrinkling of sandwich plates Yu et al. (2015). It will be referred to as 'microscopical model' in this Chapter, because the displacement unknowns in this model vary rapidly compared with the unknowns (the envelopes of the displacement) of the forthcoming Fourier-based model (macroscopic model), and thus the mesh sizes of the microscopic model should be much smaller than the wavelength to accurately describe local oscillations. Based on this microscopical model, the technique of slowly varying Fourier coefficients will be used to derive the macroscopical model in the next part.

5.3 The macroscopical model

5.3.1 The general methodology

In this part, a macroscopic finite element model will be derived from the microscopical model by using the technique of the Fourier series with slowly varying Fourier coefficients. The main idea is to expand the unknowns of the microscopic model into the Fourier series, whose slowly varying coefficients are introduced as the new

unknowns, i.e., the Fourier-based macroscopic model. In this study, we limit the expansion related to the rapid oscillations only in the x direction as in Damil et al. (2013, 2014); Huang et al. (2015):

$$\mathbf{U}(x, y) = \sum_{j=-\infty}^{+\infty} \mathbf{U}_j(x, y) e^{ijqx}, \quad (5.31)$$

where $\mathbf{U}(x, y) = \{u^t \ u^b \ v^t \ v^b \ u^* \ v^* \ w^t \ w^b \ \psi\}$ represents the rapid oscillating unknowns of the microscopic model. The Fourier coefficient $\mathbf{U}_j(x, y)$, the envelope for j^{th} order, is the new macroscopical unknown. The $\mathbf{U}_j(x, y)$ varies slowly over a period $[x, x + \frac{2\pi}{q}]$ of the oscillation. The wavenumber q is defined as

$$q = \frac{\pi}{L_x} q_0, \quad (5.32)$$

in which L_x is the length of the sandwich plate and q_0 is the number of half waves: $q_0 \in \mathbb{N}$ and $q_0 \geq 2$ that is a given number. By selecting the wavenumber q_0 , the instability mode could be controlled. In this Chapter, we consider a macroscopic model with three envelopes $\mathbf{U}_0(x, y)$, $\mathbf{U}_1(x, y)$ and $\mathbf{U}_{-1}(x, y)$, as pictured in Fig. 5.2. The envelope of the zero harmonic $\mathbf{U}_0(x, y)$ can be identified to the mean value while the complex-valued $\mathbf{U}_{\pm 1}(x, y)$ represent the envelopes or the amplitudes of the spatial oscillations. The model with only three envelopes can correctly describe the wrinkling instabilities in sandwich structures, see Liu et al. (2012).

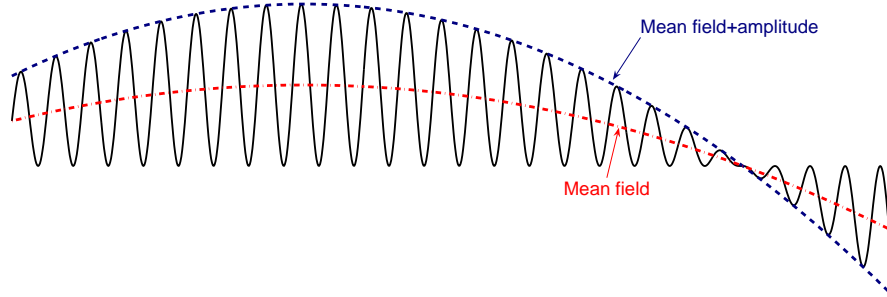


Figure 5.2: At least two macroscopical fields are necessary to describe a nearly periodic response: the mean field and the amplitude of fluctuation.

To study the local instability phenomenon of sandwich plates, some further simplified assumptions with respect to the displacement unknowns are made to get the macroscopic model within the Fourier-based approach. Firstly, as in Damil and Potier-Ferry (2010); Liu et al. (2012); Yu et al. (2013), the in-plane displacements of the neutral plane of the skins u^s , v^s and the external force F do not fluctuate,

which means that their expansion reduces into a single term: $u^t(x, y) = u_0^t(x, y)$, $u^b(x, y) = u_0^b(x, y)$, $v^t(x, y) = v_0^t(x, y)$, $v^b(x, y) = v_0^b(x, y)$, and $F(x, y) = F_0(x, y)$. As the in-plane displacements of the core in fact show fluctuation in the wrinkling direction when the sandwich plates buckle, three Fourier terms should be retained for the enrichment functions of the core's in-plane displacement kinematics:

$$\begin{aligned} u^*(x, y) &= u_0^*(x, y) + [u_{1R}^*(x, y) + iu_{1I}^*(x, y)]e^{iqx} + [u_{-1R}^*(x, y) - iu_{-1I}^*(x, y)]e^{-iqx} \\ v^*(x, y) &= v_0^*(x, y) + [v_{1R}^*(x, y) + iv_{1I}^*(x, y)]e^{iqx} + [v_{-1R}^*(x, y) - iv_{-1I}^*(x, y)]e^{-iqx}. \end{aligned} \quad (5.33)$$

Secondly, as we are interested in the local instability of the sandwich plates, the mean field of the transverse displacement $\mathscr{W}_0(x, y, z)$ for both the skins and the core is eliminated, i.e., $\mathscr{W}_0(x, y, z) = 0$. Thus, the transverse displacement $\mathscr{W}(x, y, z)$ can be:

$$\mathscr{W}(x, y, z) = 2\mathscr{W}_1(x, y, z)\cos(qx + \phi), \quad (5.34)$$

where the envelope \mathscr{W}_1 is real and equals to \mathscr{W}_{-1} . The phase ϕ could be variant so as to describe the phase modulation in the evolution of instability, see Mhada et al. (2012). To simplify our work, ϕ is assumed to be constant and equals to $\pm\frac{\pi}{2}$, which is simple yet accurate for the general cases (see Liu et al. (2012); Yu et al. (2013); Huang et al. (2015)) but may lead to a loss of accuracy near the boundary (see Mhada et al. (2012); Huang et al. (2015)). For the model exactly treating the boundary condition, one can resort to a multi-scale model similar to Hu et al. (2011).

Finally, one can get the envelopes of the displacement unknowns of the microscopic model: $\mathbf{U}_0(x, y) = \{u_0^t \ u_0^b \ v_0^t \ v_0^b \ u_0^* \ v_0^* \ 0 \ 0 \ 0\}$, $\mathbf{U}_{\pm 1}(x, y) = \{0 \ 0 \ 0 \ 0 \ u_{1R}^* \pm iu_{1I}^* \ v_{1R}^* \pm iv_{1I}^* \ \pm w_1^t \ \pm w_1^b \ \pm \psi_1\}$. One notes that if the zero harmonic of the transverse displacement is taken into account, the coupling of global and local buckling of sandwich plates (studied by a similar high order Fourier model in Liu et al. (2012) for sandwich beams) can also be characterised.

5.3.2 Internal work of the core

By using the derivation rules for Fourier series with slowly varying coefficients in Damil and Potier-Ferry (2010), the internal virtual work of the core in Eq. (5.19) is expanded into the Fourier form:

$$\delta P_{int}^c = \int_{\Omega} \sum_{j=-1}^{+1} \langle \delta \mathbf{q}_f \rangle_j [\mathbf{D}_f^c] \{ \mathbf{q}_f \}_{-j} d\Omega. \quad (5.35)$$

The unknown vector $\{\mathbf{q}_f\}_j$ is the envelope corresponding to the j^{th} harmonic of the microscopic unknowns $\{\mathbf{q}_f\}$ and their relation reads

$$\{\mathbf{q}_f\} = \sum_{j=-1}^{+1} \{\mathbf{q}_f\}_j e^{ijqx}. \quad (5.36)$$

As an example, we write $(w_{,x}^t)_1$, $(w_{,xx}^t)_1$, $(w_{,y}^t)_1$, $(w_{,yy}^t)_1$, $(w_{,xy}^t)_1$, $(u_{,x}^t)_0$ and $(u_{,y}^t)_0$ in the following form:

$$\left\{ \begin{array}{l} (w_{,x}^t)_{\pm 1} = \left(\frac{d}{dx} \pm iq \right) w_1^t = w_{1,x}^t \pm iq w_1^t, \\ (w_{,xx}^t)_{\pm 1} = \left(\frac{d}{dx} \pm iq \right)^2 w_1^t = w_{1,xx}^t - q^2 w_1^t \pm i2q w_{1,x}^t, \\ (w_{,y}^t)_{\pm 1} = w_{1,y}^t, \\ (w_{,yy}^t)_{\pm 1} = w_{1,yy}^t, \\ (w_{,xy}^t)_{\pm 1} = \left(\frac{d}{dx} \pm iq \right) w_1^t = w_{1,xy}^t \pm iq w_{1,y}^t, \\ (u_{,x}^t)_0 = u_{0,x}^t, \\ (u_{,y}^t)_0 = u_{0,y}^t. \end{array} \right. \quad (5.37)$$

According to Eq. (5.37), the envelopes $\{\mathbf{q}_f\}_{\pm 1}$ can be written as:

$$\begin{aligned} \{\mathbf{q}_f\}_{\pm 1} &= \{\mathbf{q}_f\}_{1R} \pm i \{\mathbf{q}_f\}_{1I} \\ &= [\mathbf{T}_R] \{\mathbf{q}_r\} \pm i [\mathbf{T}_I] \{\mathbf{q}_r\}, \end{aligned} \quad (5.38)$$

in which $\{\mathbf{q}_f\}_{\pm 1}$ are divided into two parts: the real one $\{\mathbf{q}_f\}_{1R}$ and the complex one $i \{\mathbf{q}_f\}_{1I}$. Then one can get the following relation: $\langle \mathbf{q}_f \rangle_1 \{\mathbf{q}_f\}_{-1} = \langle \mathbf{q}_f \rangle_{1R} \{\mathbf{q}_f\}_{1R} + \langle \mathbf{q}_f \rangle_{1I} \{\mathbf{q}_f\}_{1I}$. Besides, one can easily get $\{\mathbf{q}_f\}_0 = [\mathbf{T}_0] \{\mathbf{q}_r\}$. In the above equations, $[\mathbf{T}_0]$, $[\mathbf{T}_R]$ and $[\mathbf{T}_I] \in \mathbb{R}^{36 \times 48}$ are the transformation matrices relating the microscopic unknowns to the total unknowns of the macroscopic model $\{\mathbf{q}_r\} \in \mathbb{R}^{48 \times 1}$ and their non-zero elements are listed in Table 5.4. According to the assumptions in Section 5.3.1, the microscopic unknowns $\{\mathbf{q}_f\}$ in Eq. (5.15) is transformed into

the Fourier or macroscopic version $\{\mathbf{q}_r\}$ as

$$\langle \mathbf{q}_r \rangle = \left\langle \begin{array}{cccccccccccccccc} u_0^t & u_{0,x}^t & u_{0,y}^t & v_0^t & v_{0,x}^t & v_{0,y}^t & u_0^b & u_{0,x}^b & u_{0,y}^b & v_0^b & v_{0,x}^b & v_{0,y}^b & \\ u_0^* & u_{0,x}^* & u_{0,y}^* & v_0^* & v_{0,x}^* & v_{0,y}^* & u_{1R}^* & u_{1R,x}^* & u_{1R,y}^* & u_{1I}^* & u_{1I,x}^* & u_{1I,y}^* & \\ v_{1R}^* & v_{1R,x}^* & v_{1R,y}^* & v_{1I}^* & v_{1I,x}^* & v_{1I,y}^* & w_1^t & w_{1,x}^t & w_{1,xx}^t & w_{1,y}^t & w_{1,yy}^t & w_{1,xy}^t & \\ w_1^b & w_{1,x}^b & w_{1,xx}^b & w_{1,y}^b & w_{1,yy}^b & w_{1,xy}^b & \psi_1 & \psi_{1,x} & \psi_{1,xx} & \psi_{1,y} & \psi_{1,yy} & \psi_{1,xy} \end{array} \right\rangle. \quad (5.39)$$

Then, the internal virtual work of the core in Eq. (5.35) can be rewritten as

$$\begin{aligned} \delta P_{int}^c &= \int_{\Omega} \langle \delta \mathbf{q}_f \rangle_0 [\mathbf{D}_f^c] \{\mathbf{q}_f\}_0 + \langle \delta \mathbf{q}_f \rangle_1 [\mathbf{D}_f^c] \{\mathbf{q}_f\}_{-1} + \langle \delta \mathbf{q}_f \rangle_{-1} [\mathbf{D}_f^c] \{\mathbf{q}_f\}_1 \, d\Omega \\ &= \int_{\Omega} \langle \delta \mathbf{q}_f \rangle_0 [\mathbf{D}_f^c] \{\mathbf{q}_f\}_0 + 2 \langle \delta \mathbf{q}_f \rangle_{1R} [\mathbf{D}_f^c] \{\mathbf{q}_f\}_{1R} + 2 \langle \delta \mathbf{q}_f \rangle_{1I} [\mathbf{D}_f^c] \{\mathbf{q}_f\}_{1I} \, d\Omega \\ &= \int_{\Omega} \langle \delta \mathbf{q}_r \rangle [\mathbf{D}_r^c] \{\mathbf{q}_r\} \, d\Omega, \end{aligned} \quad (5.40)$$

in which the generalized macroscopic elastic matrix $[\mathbf{D}_r^c] \in \mathbb{R}^{48 \times 48}$ is

$$[\mathbf{D}_r^c] = [\mathbf{T}_0]^T [\mathbf{D}_f^c] [\mathbf{T}_0] + 2[\mathbf{T}_R]^T [\mathbf{D}_f^c] [\mathbf{T}_R] + 2[\mathbf{T}_I]^T [\mathbf{D}_f^c] [\mathbf{T}_I]. \quad (5.41)$$

Table 5.4: Relevant transformation matrices for the core layer, in which the non-zero elements are listed.

Matrix	Size	
$[\mathbf{T}_R]$	36×48	(13,19)=1, (14,20)=1, (14,22)=-q, (15,21)=1, (16,25)=1, (17,26)=1, (17,28)=-q, (18,27)=1, (19,31)=1, (20,32)=1, (21,33)=1, (21,31)=-q ² , (22,34)=1, (23,35)=1, (24,36)=1, (25,37)=1, (26,38)=1, (27,39)=1, (27,37)=-q ² , (28,40)=1, (29,41)=1, (30,42)=1, (31,43)=1, (32,44)=1, (33,45)=1, (33,43)=-q ² , (34,46)=1, (35,47)=1, (36,48)=1.
$[\mathbf{T}_I]$	36×48	(13,22)=1, (14,19)=q, (14,23)=1, (15,24)=1, (16,28)=1, (17,25)=q, (17,29)=1, (18,30)=1, (20,31)=q, (21,32)=2q, (24,34)=q, (26,37)=q, (27,38)=2q, (30,40)=q, (32,43)=q, (33,44)=2q, (36,46)=q.
$[\mathbf{T}_0]$	36×48	(1,1)=1, (2,2)=1, (3,3)=1, (4,4)=1, (5,5)=1, (6,6)=1, (7,7)=1, (8,8)=1, (9,9)=1, (10,10)=1, (11,11)=1, (12,12)=1, (13,13)=1, (14,14)=1, (15,15)=1, (16,16)=1, (17,17)=1, (18,18)=1.

5.3.3 Internal work of the skins

Similar to Section 5.3.2, the internal virtual work of the skins in Eq. (5.21) is also expressed in the following Fourier form:

$$\delta P_{int}^s = \int_{\Omega} \sum_{j=-1}^{+1} \langle \delta \gamma_f^s \rangle_{-j} \{\mathbf{S}_f^s\}_j \, d\Omega = \int_{\Omega} \langle \delta \gamma_f^s \rangle_0 \{\mathbf{S}_f^s\}_0 + 2 \langle \delta \gamma_f^s \rangle_{1R} \{\mathbf{S}_f^s\}_{1R} + 2 \langle \delta \gamma_f^s \rangle_{1I} \{\mathbf{S}_f^s\}_{1I} \, d\Omega, \quad (5.42)$$

in which the envelopes of the generalized stress vector $\{\mathbf{S}_f^s\}$ in Eq. (5.26) are

$$\begin{aligned} \{\mathbf{S}_f^s\}_0 &= [\mathbf{D}_f^s] \{\gamma_f^s\}_0 \\ \{\mathbf{S}_f^s\}_{1R} &= [\mathbf{D}_f^s] \{\gamma_f^s\}_{1R} \\ \{\mathbf{S}_f^s\}_{1I} &= [\mathbf{D}_f^s] \{\gamma_f^s\}_{1I}, \end{aligned} \quad (5.43)$$

and the envelopes of the generalized strain vector $\{\gamma_f^s\}$ in Eq. (5.22) are written as

$$\begin{aligned} \{\gamma_f^s\}_0 &= [\mathbf{H}_f^s] \{\mathbf{q}_f^s\}_0 + \frac{1}{2} [\mathbf{A}_f (\{\mathbf{q}_f^s\}_0)] \{\mathbf{q}_f^s\}_0 + [\mathbf{A}_f (\{\mathbf{q}_f^s\}_{1R})] \{\mathbf{q}_f^s\}_{1R} + [\mathbf{A}_f (\{\mathbf{q}_f^s\}_{1I})] \{\mathbf{q}_f^s\}_{1I} \\ \{\gamma_f^s\}_{1R} &= [\mathbf{H}_f^s] \{\mathbf{q}_f^s\}_{1R} + [\mathbf{A}_f (\{\mathbf{q}_f^s\}_0)] \{\mathbf{q}_f^s\}_{1R} \\ \{\gamma_f^s\}_{1I} &= [\mathbf{H}_f^s] \{\mathbf{q}_f^s\}_{1I} + [\mathbf{A}_f (\{\mathbf{q}_f^s\}_0)] \{\mathbf{q}_f^s\}_{1I}. \end{aligned} \quad (5.44)$$

By introducing the following generalized macroscopic stress $\{\mathbf{S}_r^s\}$, strain $\{\gamma_r^s\} \in \mathbb{R}^{18 \times 1}$ and displacement gradient $\{\mathbf{q}_r^s\} \in \mathbb{R}^{27 \times 1}$ in skins:

$$\{\mathbf{S}_r^s\} = \begin{Bmatrix} \{\mathbf{S}_f^s\}_0 \\ \{\mathbf{S}_f^s\}_{1R} \\ \{\mathbf{S}_f^s\}_{1I} \end{Bmatrix}, \quad \{\gamma_r^s\} = \begin{Bmatrix} \{\gamma_f^s\}_0 \\ 2\{\gamma_f^s\}_{1R} \\ 2\{\gamma_f^s\}_{1I} \end{Bmatrix}, \quad \{\mathbf{q}_r^s\} = \begin{Bmatrix} \{\mathbf{q}_f^s\}_0 \\ \{\mathbf{q}_f^s\}_{1R} \\ \{\mathbf{q}_f^s\}_{1I} \end{Bmatrix}, \quad (5.45)$$

the generalized macroscopic stress-strain and strain-displacement relations of the skins can be consequently rewritten into the similar form as that in the microscopic model (see Eqs. (5.22) and (5.26)):

$$\begin{aligned} \{\mathbf{S}_r^s\} &= [\mathbf{D}_r^s] \{\gamma_r^s\} \\ \{\gamma_r^s\} &= \left([\mathbf{H}_r^s] + \frac{1}{2} [\mathbf{A} (\{\mathbf{q}_r^s\})] \right) \{\mathbf{q}_r^s\}, \end{aligned} \quad (5.46)$$

in which, the matrices $[\mathbf{D}_r^s]$, $[\mathbf{H}_r^s]$, $[\mathbf{A}_r(\mathbf{q}_r^s)]$ can be easily assembled by the corresponding terms of Eqs. (5.23) and (5.27) in the microscopic model

$$\begin{aligned}
 [\mathbf{D}_r^s] &= \begin{bmatrix} \mathbf{D}_f^s & \mathbf{0} & \mathbf{0} \\ \mathbf{0} & \frac{1}{2}\mathbf{D}_f^s & \mathbf{0} \\ \mathbf{0} & \mathbf{0} & \frac{1}{2}\mathbf{D}_f^s \end{bmatrix} \\
 [\mathbf{H}_r^s] &= \begin{bmatrix} \mathbf{H}_f^s & \mathbf{0} & \mathbf{0} \\ \mathbf{0} & 2\mathbf{H}_f^s & \mathbf{0} \\ \mathbf{0} & \mathbf{0} & 2\mathbf{H}_f^s \end{bmatrix} \\
 [\mathbf{A}_r(\mathbf{q}_r^s)] &= 2 \begin{bmatrix} \frac{1}{2}\mathbf{A}_f(\{\mathbf{q}_f^s\}_0) & \mathbf{A}_f(\{\mathbf{q}_f^s\}_{1R}) & \mathbf{A}_f(\{\mathbf{q}_f^s\}_{1I}) \\ \mathbf{A}_f(\{\mathbf{q}_f^s\}_{1R}) & \mathbf{A}_f(\{\mathbf{q}_f^s\}_0) & \mathbf{0} \\ \mathbf{A}_f(\{\mathbf{q}_f^s\}_{1I}) & \mathbf{0} & \mathbf{A}_f(\{\mathbf{q}_f^s\}_0) \end{bmatrix}.
 \end{aligned} \tag{5.47}$$

The internal virtual work of the skins in Eq. (5.42) then reads:

$$\delta P_{int}^s = \int_{\Omega} \langle \delta \gamma_r^s \rangle \{\mathbf{S}_r^s\} d\Omega = \int_{\Omega} \langle \delta \mathbf{q}_r^s \rangle ([\mathbf{H}_r^s]^T + [\mathbf{A}_r(\mathbf{q}_r^s)]^T) \{\mathbf{S}_r^s\} d\Omega. \tag{5.48}$$

The skins macroscopic unknown vector $\{\mathbf{q}_r^s\}$ can be related to the total unknown vector of the macroscopic model $\{\mathbf{q}_r\}$ by

$$\{\mathbf{q}_r^s\} = [\mathbf{R}_r^s] \{\mathbf{q}_r\} \tag{5.49}$$

where the transformation matrix $[\mathbf{R}_r^s] \in \mathbb{R}^{27 \times 48}$ is

$$[\mathbf{R}_r^s] = \begin{bmatrix} \mathbf{R}_f^s \mathbf{T}_0 \\ \mathbf{R}_f^s \mathbf{T}_R \\ \mathbf{R}_f^s \mathbf{T}_I \end{bmatrix}. \tag{5.50}$$

Finally, the macroscopic version of the virtual internal work of the skins can be

$$\delta P_{int}^s = \int_{\Omega} \langle \delta \mathbf{q}_r \rangle [\mathbf{R}_r^s]^T ([\mathbf{H}_r^s]^T + [\mathbf{A}_r(\mathbf{q}_r)]^T) \{\mathbf{S}_r^s\} d\Omega. \tag{5.51}$$

5.3.4 Governing equations of macroscopical model

Considering the load proportional to a parameter λ_r and neglecting the body forces, the external virtual work is defined as

$$\delta P_{ext} = \lambda_r \int_{\Omega} \langle \delta \mathbf{q}_r \rangle \{ \mathbf{F}_r \} d\Omega. \quad (5.52)$$

Similar to the parameters in the microscopical model, $\{ \mathbf{F}_r \} \in \mathbb{R}^{48 \times 1}$ denotes the external load and λ_r is the load proportional parameter. Finally the governing equation of the macroscopical model reads

$$\begin{cases} \int_{\Omega} \langle \delta \mathbf{q}_r \rangle [\mathbf{R}_r^t]^T \left([\mathbf{H}_r^t]^T + [\mathbf{A}_r(\mathbf{q}_r^t)]^T \right) \{ \mathbf{S}_r^t \} + \langle \delta \mathbf{q}_r \rangle [\mathbf{R}_r^b]^T \left([\mathbf{H}_r^b]^T + [\mathbf{A}_r(\mathbf{q}_r^b)]^T \right) \{ \mathbf{S}_r^b \} d\Omega \\ + \int_{\Omega} \langle \delta \mathbf{q}_r \rangle [\mathbf{D}_r^c] \{ \mathbf{q}_r \} d\Omega = \lambda_r \int_{\Omega} \langle \delta \mathbf{q}_r \rangle \{ \mathbf{F}_r \} d\Omega, \\ \{ \mathbf{S}_r^t \} = [\mathbf{D}_r^s] \left([\mathbf{H}_r^t] + \frac{1}{2} [\mathbf{A}_r(\mathbf{q}_r^t)] \right) [\mathbf{R}_r^t] \{ \mathbf{q}_r \}, \\ \{ \mathbf{S}_r^b \} = [\mathbf{D}_r^s] \left([\mathbf{H}_r^b] + \frac{1}{2} [\mathbf{A}_r(\mathbf{q}_r^b)] \right) [\mathbf{R}_r^b] \{ \mathbf{q}_r \}. \end{cases} \quad (5.53)$$

The unknowns in Eq. (5.53) denote to the slowly varying envelopes of the displacement field, which are completely different from those rapidly fluctuating displacement field in Eq. (5.30) or in Yu et al. (2015). However, one can notice that the governing equations for the microscopic and macroscopic models are almost the same in the form, which brings a lot of conveniences to implement the new macroscopic model based on our previous work (Yu et al. (2015)).

5.4 Discretization

In this part, the Finite Element Method (FEM) is used to solve Eq. (5.53). The in-plane displacements related to u, v, u^*, v^* are discretized by the 4-node Lagrange bi-linear shape functions while the transversal displacements w, ψ by the 4-node non-conforming rectangular functions, see Reddy (2004a); Zienkiewicz and Cheung (1964); Melosh (1963). The non-conforming element can lead to accurate results with less degrees of freedom compared to the conforming element, and the membrane locking and shear locking effect is not obvious in this element, see Yu et al. (2015); Reddy (2004a). The node numbering is shown in Fig. 5.3. The standard

bi-linear isotropic shape functions read as

$$N_{\mathcal{L}} = \left\{ \frac{(1-\xi)(1-\eta)}{4}, \frac{(1+\xi)(1-\eta)}{4}, \frac{(1+\xi)(1+\eta)}{4}, \frac{(1-\xi)(1+\eta)}{4} \right\} \quad (5.54)$$

where the parameters ξ and η are the elementary local coordinates.

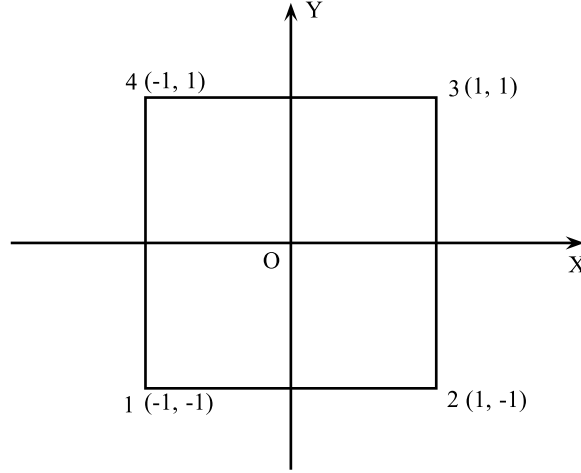


Figure 5.3: The element natural reference system and nodes coordinates.

The non-conforming element consists of three degrees of freedom ($w, \frac{\partial w}{\partial x}, \frac{\partial w}{\partial y}$) at each vertex node. The interpolation functions are

$$N_{\mathcal{H}} = \{ \mathcal{H}_1, \mathcal{H}_{1x}, \mathcal{H}_{1y}, \mathcal{H}_2, \mathcal{H}_{2x}, \mathcal{H}_{2y}, \dots, \mathcal{H}_4, \mathcal{H}_{4x}, \mathcal{H}_{4y} \} \quad (5.55)$$

where

$$\begin{aligned} \mathcal{H}_i &= \frac{1}{8}(1+\xi_0)(1+\eta_0)(2+\xi_0+\eta_0-\xi^2-\eta^2) \\ \mathcal{H}_{ix} &= \frac{1}{8}\xi_i(\xi_0-1)(1+\eta_0)(1+\xi_0)^2 \\ \mathcal{H}_{iy} &= \frac{1}{8}\eta_i(\eta_0-1)(1+\xi_0)(1+\eta_0)^2, \end{aligned} \quad (5.56)$$

in which $i = 1, 2, 3, 4$, $\xi_0 = \xi_i\xi$, $\eta_0 = \eta_i\eta$, ξ_i and η_i are the corresponding node coordinates in the natural reference system. Then, the macroscopical discretized unknowns could be written as

$$\{\mathbf{q}_r\} = [\mathbf{G}_r] \{\boldsymbol{\theta}_r\}^e, \quad (5.57)$$

where $[\mathbf{G}_r]$ is the interpolation matrix that is assembled by $N_{\mathcal{L}}$, $N_{\mathcal{H}}$ and their derivation in terms of the local coordinates. The vector $\{\boldsymbol{\theta}_r\}^e = \{ \{\boldsymbol{\theta}_r\}_1^e \mid \{\boldsymbol{\theta}_r\}_2^e \mid \{\boldsymbol{\theta}_r\}_3^e \mid \{\boldsymbol{\theta}_r\}_4^e \}$

is the nodal unknowns of an element with 19 degrees of freedom per node:

$$\{\boldsymbol{\theta}_r\}_i^e = \left\{ u_0^t \ v_0^t \ u_0^b \ v_0^b \ u_0^* \ u_{1R}^* \ u_{1I}^* \ v_0^* \ v_{1R}^* \ v_{1I}^* \ w_1^t \ w_{1,x}^t \ w_{1,y}^t \ w_1^b \ w_{1,x}^b \ w_{1,y}^b \ \psi_1 \ \psi_{1,x} \ \psi_{1,y} \right\}_i^e. \quad (5.58)$$

Finally, by substituting Eq. (5.57) into Eq. (5.53) the discretized form of the governing equation for the macroscopical model is expressed as:

$$\left\{ \begin{aligned} & \int_{\Omega} \langle \delta \boldsymbol{\theta}_r \rangle [\mathbf{G}_r]^T [\mathbf{R}_r^t]^T \left([\mathbf{H}_r]^T + [\mathbf{A}_r(\boldsymbol{\theta}_r^t)]^T \right) \{ \mathbf{S}_r^t \} \\ & + \langle \delta \boldsymbol{\theta}_r \rangle [\mathbf{G}_r]^T [\mathbf{R}_r^b]^T \left([\mathbf{H}_r]^T + [\mathbf{A}_r(\boldsymbol{\theta}_r^b)]^T \right) \{ \mathbf{S}_r^b \} d\Omega \\ & + \int_{\Omega} \langle \delta \boldsymbol{\theta}_r \rangle [\mathbf{G}_r]^T [\mathbf{D}_r^c] [\mathbf{G}_r] \{ \boldsymbol{\theta}_r \} d\Omega = \lambda_r \int_{\Omega} \langle \delta \boldsymbol{\theta}_r \rangle [\mathbf{G}_r]^T \{ \mathbf{F}_r \} d\Omega, \quad (5.59) \\ & \{ \mathbf{S}_r^t \} = [\mathbf{D}_r^s] \left([\mathbf{H}_r] + \frac{1}{2} [\mathbf{A}_r(\boldsymbol{\theta}_r^t)] \right) [\mathbf{R}_r^t] [\mathbf{G}_r] \{ \boldsymbol{\theta}_r \}, \\ & \{ \mathbf{S}_r^b \} = [\mathbf{D}_r^s] \left([\mathbf{H}_f] + \frac{1}{2} [\mathbf{A}_r(\boldsymbol{\theta}_r^b)] \right) [\mathbf{R}_r^b] [\mathbf{G}_r] \{ \boldsymbol{\theta}_r \}. \end{aligned} \right.$$

The resulting non-linear problem Eq. (5.59) is solved by the Asymptotic Numerical Method (ANM) Cochelin et al. (1994). For each element, the macroscopic unknowns are determined at the nodes and the stress at the Gauss points. A short brief introduction on the use of the ANM for the resolution of non-linear problems is given in Appendix A.

5.5 Numerical results

In this part, we firstly investigate the accuracy and convergence of the proposed macroscopic or Fourier-based model for the instability phenomena in sandwich plates by comparing its results with those of other models, and then extend the model to simulate the antisymmetrical and symmetrical local wrinkling with larger wavenumbers. To verify the macroscopic model, reference results are obtained by constructing a 3D finite element model in ABAQUS, which are referred to as "Shell/Volume/Shell" or "3D FEM model". In this model, the 8-node shell element S8R is used for the skins and 20-node brick element C3D20R for the core layer, see Yu et al. (2015). The skins are bonded to the core layer using "tie" constraints. For the 3D FEM solution, the nonlinear post-buckling analysis is performed by a load-displacement algorithm (RIKS) in ABAQUS. To trigger the interested buckling instability during simulation, the eigenmodes obtained from the linear perturbation analysis (BUCKLE) is introduced as the initial geometric imperfection, which

is small enough to ensure the accuracy of the results. Unless other statements, the following 3D FEM solution procedure is the same as mentioned above.

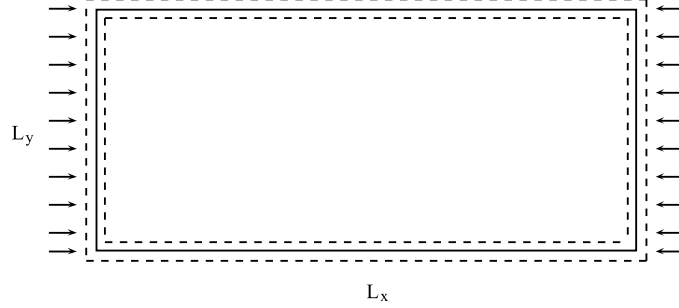


Figure 5.4: The configuration of the rectangular sandwich plate. Its four edges are simply supported and uni-axial loads are applied.

Table 5.5: Geometric and material parameters of the sandwich plate.

L_x [m]	L_y [m]	E_s [Pa]	$\nu_{c(s)}$	E_c/E_s	h_c/h_s	L_x/h_t
0.5	0.25	6.9×10^{10}	0.3	10^{-4}	10	50

5.5.1 Validation and mesh convergence study

To validate the proposed 2D macroscopic model, numerical test with the same rectangular sandwich plate under uni-axial compression in Yu et al. (2015) is conducted. Meanwhile, the convergence with respect to the mesh is studied for the 2D macroscopic model. The obtained wrinkling pattern and critical load are mainly compared with the 3D FEM solution. As shown in Fig. 5.4, the rectangular sandwich plate is simply supported around four edges, which is realised by constraining the derivative of the envelope of the transversal displacement $w_{1,x}^s$ for the two edges of length L_y and w_1^s for the other two edges in the 2D macroscopic model (similar way to apply boundary conditions can be found in the works (Liu et al. (2012); Mhada et al. (2012))), and the x -directional in-plane compressive loads are applied at the two ends of the skins that are perpendicular to the x axis. The geometric and material parameters presented in Table 5.5 are applied to all the numerical examples in this Chapter.

Fig. 5.5 qualitatively presents the color map of the transversal displacement obtained by the 2D macroscopic model and the 3D FEM model, which is the lowest buckling mode for the considered sandwich configuration. We can see that the two models display the same instability pattern with five half waves in the x direction and one half wave in the y direction, which demonstrates that the 2D macroscopic

model is capable to well characterise the wrinkling pattern. Table 5.6 presents

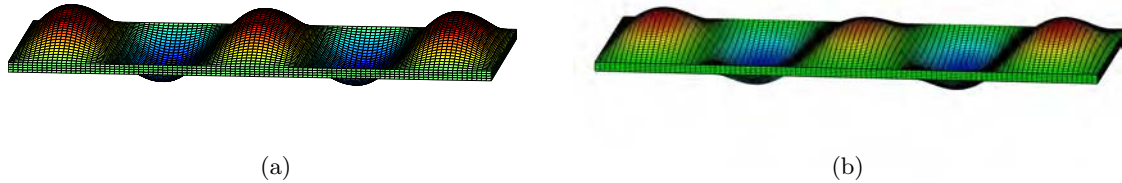


Figure 5.5: The wrinkling patterns obtained by (a) the 2D macroscopic sandwich plate model and (b) the 3D FEM model.

the mesh details on the number of elements along the in-plane and through-the-thickness directions, the total number of elements and DOFs for the 3D FEM model, the 2D microscopic and macroscopic sandwich plate models. For the 3D FEM model, four elements are used along the thickness of the core to avoid over-stiffening solution, and the in-plane element aspect ratio is equal to one (see Yu et al. (2015); Léotoing et al. (2004)), which thus leads to about $4.7 \cdot 10^5$ DOFs. For the 2D macroscopic model, three mesh schemes with the x -directional element number N_{ex} varying from 2 to 8 are considered and perturbation forces of value $F \cdot 10^{-5}$ are applied on both the top and bottom skins along the center line $x = \frac{L_x}{2}$ to trigger the post-buckling. The wavenumber is set to $q_0 = 5$ to produce the interested wrinkling pattern. Fig. 5.6 shows the bifurcation path of the maximal transverse displacement versus the applied compressive load. The presented critical loads by the 2D macroscopic model with three mesh schemes converge to $2.02 \cdot 10^4$ N/m (see also Table 5.6) and are all in good agreement with that obtained by the 3D FEM model and the 2D microscopic model in Yu et al. (2015). One notes that for the proposed 2D macroscopic model only 2 elements in the wrinkling direction can be sufficient to accurately predict the local wrinkling phenomenon. It leads to just 285 DOFs, which corresponds to only about 0.06% DOFs of the 3D FEM model and even saves about 82% DOFs compared with the 2D microscopic model of Yu et al. (2015). This numerical test indicates the accuracy and efficiency of the 2D macroscopic sandwich model in describing the instability phenomenon of the sandwich plate. Besides, we would like to mention that the mesh size of the proposed model is independent on the wrinkling wavelength, which makes this model even more attractive in efficiency than the other two models when considering instability phenomena with very small wavelength or extremely large wavenumbers (see details in Section 5.5.3).

	N_{ex}	N_{ey}	N_{ez}	Total elements	DOFs	Critical load (10^4 N/m)
Shell/Volume/Shell	100	50	6	30000	474939	2.02
2D Microscopic Model	20	4	-	80	1575	2.00
2D Macroscopic Model	2	4	-	8	285	2.02
2D Macroscopic Model	4	4	-	16	475	2.02
2D Macroscopic Model	8	4	-	32	855	2.02

Table 5.6: The mesh scheme for the 3D FEM model, the 2D microscopic model and the 2D macroscopic model under the uni-axial compressive load.

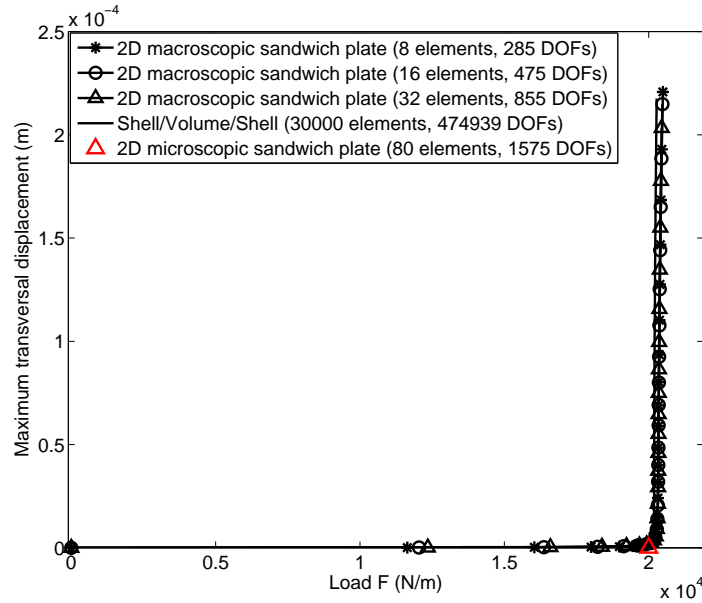


Figure 5.6: Bifurcation analysis for validation and mesh convergence of the 2D macroscopic sandwich model.

5.5.2 Antisymmetrical wrinkling

In this section, the antisymmetrical wrinkling with larger wavenumbers for the same sandwich plate ($L_x/L_y = 2$) in Fig. 5.4 will be investigated based on the proposed 2D macroscopic model. The material properties, geometrical data and boundary conditions remain the same as in Section 5.5.1.

Fig. 5.7 shows the antisymmetrical wrinkling patterns with seven half waves in the x direction and two half waves in the y direction, which are obtained by the 2D macroscopic model and the 3D FEM model. The two wrinkling morphologies match fairly well. For the 3D FEM model, the mesh density is the same as in Section 5.5.1. Generally, at least 4 elements should be used in a period of the wrinkle to get reasonable results, and thus 100 elements in the wrinkling direction is accurate enough to characterise seven or more half waves in the high modes

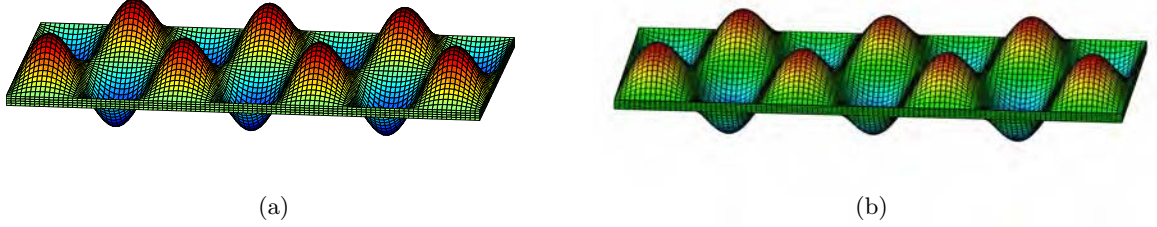


Figure 5.7: The antisymmetrical wrinkling patterns obtained by (a) the 2D macroscopic sandwich plate model and (b) the 3D FEM model.

considered below. In the macroscopic model, since the mesh size is not related to the wrinkling wavelength but to the variation of the envelope, only 2 elements in the x direction is used. As the displacement variables are not expanded in the y direction by the Fourier series, 4 elements are needed to describe the two half waves in this direction. Therefore, for the macroscopic model the mesh scheme with $N_{ex} \times N_{ey} = 2 \times 4$ will be used for all the numerical examples below. On both the top and bottom skins, the vertical perturbation forces $F \cdot 10^{-5}$ are applied along the line $x = \frac{L_x}{2}$, $-\frac{L_y}{2} \leq y \leq 0$ and the negative forces along the line $x = \frac{L_x}{2}$, $0 \leq y \leq \frac{L_y}{2}$ to trigger the wrinkling with two half waves in the y direction. Fig. 5.8 illustrates the bifurcation curves for the antisymmetrical wrinkling pattern with the high mode. Both models predict almost the same critical buckling load with about $3.00 \cdot 10^4$ N/m and the post bifurcation responses also match fairly well. The proposed 2D macroscopic model only uses 8 elements (285 DOFs), which saves about 99.94% computational resource compared with the 3D FEM solution.

Fig. 5.9 also presents the critical loads obtained by the two models for different high antisymmetrical modes, in which the half wave numbers are respectively 1 and 2 in the y direction and changing from 5 to 13 in the x direction. All the critical loads agree very well with each other, in which the maximum difference is only 1.9%. Here, we should emphasize that the total element number remains the same as 8 for all the considered buckling modes and only the wavenumber q_0 is changed in the 2D macroscopic model. This is a great advantage compared to the general microscopic models (such as the 3D FEM model or the 2D microscopic sandwich plate model of Yu et al. (2015)), especially when dealing with instability phenomena with very small wavelength. For microscopic models, the number of the elements is related to the wavenumber or the wavelength, and thus the increase in wavenumber or the decrease in wavelength will lead to a larger computational

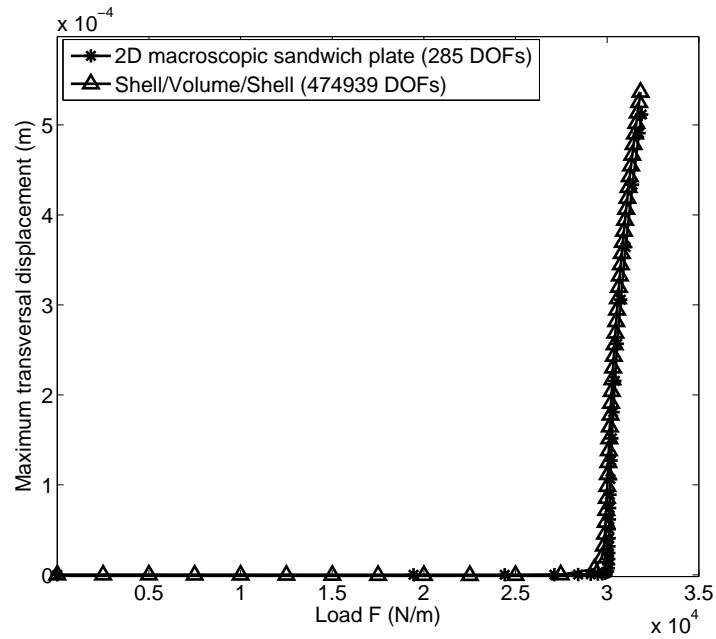


Figure 5.8: Bifurcation path for the antisymmetric wrinkling with 7 half waves in the x direction and 2 half waves in the y direction.

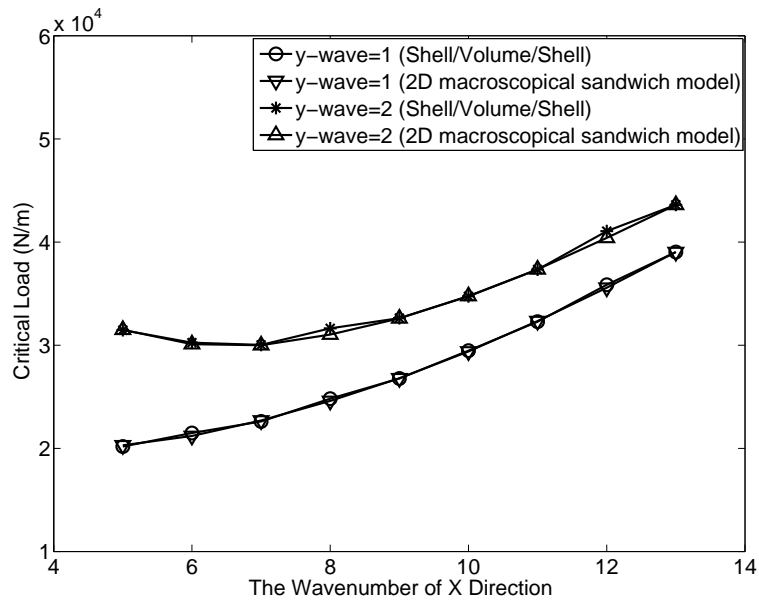


Figure 5.9: Critical loads for different antisymmetric modes with the 3D FEM model and the 2D macroscopic sandwich model. “ y -wave” is short for half-wave numbers in the y direction.

cost. Besides, special perturbation forces should be carefully introduced in the microscopic models in order to obtain a certain buckling mode, which causes difficulties in controlling the nonlinear calculation. The perturbation sensitivity of the buckling mode was observed in Liu et al. (2012) and Léotoing et al. (2004) where very tiny perturbations can shift global buckling into local wrinkling for a certain sandwich beam. Therefore, the proposed 2D macroscopic sandwich finite element model has high efficiency, robustness and accuracy to describe the antisymmetrical wrinkling in sandwich plates. Furthermore, these features provide a different way, from the numerical aspect, to determine the lowest buckling mode and the corresponding critical load of sandwich plates by calculating the critical load with different wavenumber q_0 and then choosing the lowest one.

5.5.3 Symmetrical wrinkling

The symmetrical wrinkling patterns are investigated for the same sandwich plate as in Fig. 5.4. Two different kinds of loading cases are considered in this part: the uni-axial compressive load (the same as Section 5.5.1) and the equi-biaxial compressive load. For the latter, the compressive loads are applied on both the bottom and top skins in the x and y directions, and the four edges of the sandwich plate are still simply supported. Due to the symmetry of this kind of wrinkling, the transversal displacements of the mid-plane of the core layer could be constrained to zero. This is realised by setting the enrichment function of the transversal displacement ψ equal to 0 in the 2D macroscopic model.

5.5.3.1 Symmetrical wrinkling for uni-axial compressive load case

The sandwich plate is subjected to the uni-axial compressive load in the x direction. Here, the one-dimensional wrinkling pattern is investigated (see Fig. 5.10). For the 2D macroscopic model and the 3D FEM model, the mesh schemes keep the same as above (see Section 5.5.1). To trigger the post-buckling, the vertical perturbation forces $F \cdot 10^{-5}$ are applied on the top skin along the middle line $x = \frac{L_x}{2}$ and the opposite ones with equal value are applied on the bottom skin. Fig. 5.10 presents the transversal displacement contour obtained by the two models, which has 25 half waves in the x direction. The wrinkling morphologies are quite similar. The transversal displacement near the bifurcation point for the middle line $y = 0$ of the sandwich plate is further depicted in Fig. 5.11, which is quite similar to the symmetrical wrinkling in sandwich beams analysed with efficient one-dimensional finite elements (see Hu et al. (2009a) and Liu et al. (2012)). The symmetrical

wrinkling in the sandwich plate with the thickness ratio $h_c/h_s = 10$ can be treated as a thin film resting on a thin substrate. According to Huang et al. (2005), the analytical wavelength for the one-dimensional wrinkling is about 0.047 m in this kind of structure, which is close to the wavelength 0.04 m numerically predicted by the 2D macroscopic model. Fig. 5.12 presents the curve of the transversal

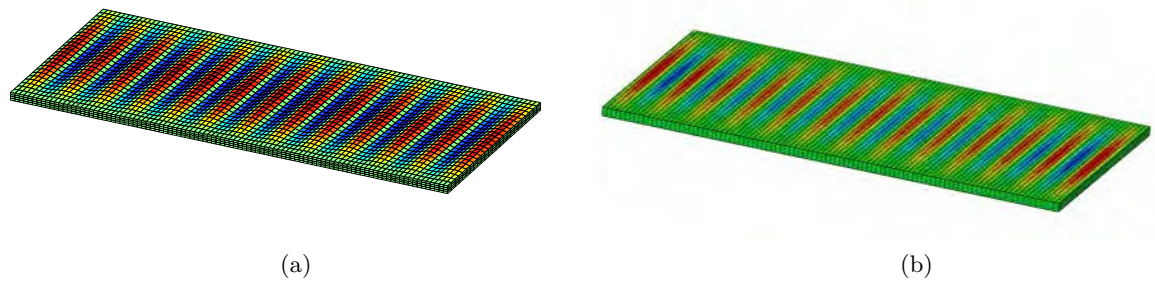


Figure 5.10: The symmetrical wrinkling patterns obtained by (a) the 2D macroscopic sandwich plate model and (b) the 3D FEM model. The sandwich plate (see Table 5.5 for geometric and material details) is under uni-axial load.

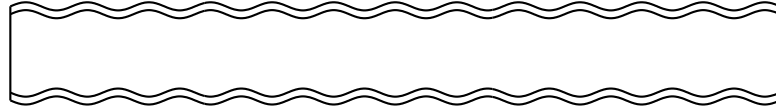


Figure 5.11: The transversal displacement along the line $y = 0$ for the symmetrical wrinkling by the 2D macroscopic model. The sandwich plate is under uni-axial load.

displacement of the top skin at the point $x = L_x/2$, $y = 0$ versus the external load, in which the critical load predicted by the 2D macroscopic model matches fairly well with that of the 3D FEM model with about $1.69 \cdot 10^5$ N/m. This critical load is a little larger than the analytical Léotoing et al. (2002b) and numerical Hu et al. (2009a); Liu et al. (2012) results for the symmetrical wrinkling with about $1.53 \cdot 10^5$ N/m. The little discrepancy may arise from the stiffening effect caused by boundary condition, where the edges $y = -L_y/2$ and $L_y/2$ of the sandwich plate are simply supported in this Chapter and, however, free in Hu et al. (2009a); Liu et al. (2012); Léotoing et al. (2002b).

Fig. 5.13 displays the bifurcation curves for the symmetrical wrinkling with different half waves in the x direction. One notices that the difference of the critical loads for the five cases is quite small, where the maximum discrepancy is less than

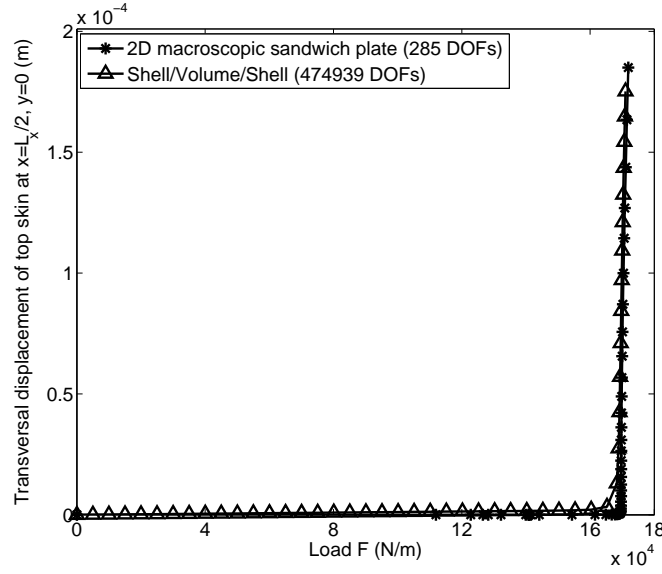


Figure 5.12: The bifurcation path for the symmetrical wrinkling of the sandwich plate under the uni-axial load.

2%. Thus, if such wrinkling patterns are simulated using the microscopic model of Yu et al. (2015), the value and location of perturbation forces should be carefully applied to detect the useful buckling mode, which leads to significant difficulties in nonlinear calculation. Nevertheless, it can be quite easy for the 2D macroscopic model to distinguish and detect the useful buckling mode by just changing the wavenumber q_0 .

5.5.3.2 Symmetrical wrinkling for equi-biaxial compressive load case

In this part, the skins of the sandwich plate are subjected to the equi-biaxial compressive load in the x and y directions. The symmetrical wrinkling with checkerboard patterns occurs, which alleviates the in-plane compressive stresses in all directions and leads to lower energy than that of the one-dimensional wrinkling, see Chen and Hutchinson (2004). Fig. 5.14 presents the color map of the transversal displacement for the sandwich plate (one quarter of the plate near the upper left boundary is zoomed for more clarity), which has 17 half waves in the x direction and 9 half waves in the y direction. For the 2D macroscopic model, the mesh scheme $N_{ex} \times N_{ey} = 2 \times 18$ (1083 DOFs) is used. One notes that as the displacement field is expanded in the x direction, only 2 elements are used in this direction. The mesh scheme for the 3D FEM model remains unchanged (474939 DOFs). Fig. 5.15 shows the curve of the transversal displacement at the middle point $x = L_x/2$, $y = 0$

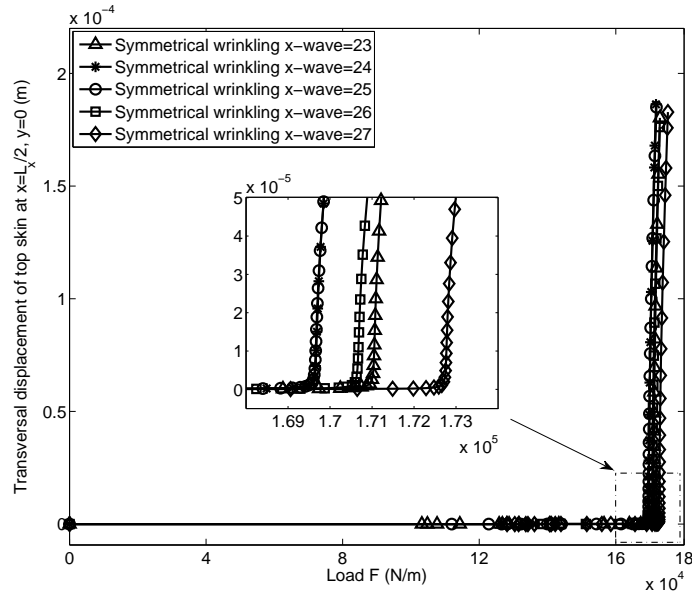


Figure 5.13: The bifurcation curves for the symmetrical wrinkling of the sandwich plate under the uni-axial load with different half waves in the x direction, and the wave number in the y direction is one. The results are obtained by the 2D macroscopic model.

of the top skin versus the external load. The critical load predicted by the 2D macroscopic model matches fairly well with that of the 3D FEM solution obtained by the eigenmode analysis. However, the 2D macroscopic model just uses 0.02% computational source (in terms of DOFs) of the 3D FEM model.

As a final example, the checkerboard pattern with vast wavenumbers, thus very small wavelength, for the symmetrical wrinkling is presented in Fig. 5.16. This wrinkling pattern can be easily captured by the 2D macroscopic model with only 2 elements in the x direction. However, it would be a great trouble for the microscopic model (Yu et al. (2015)) or the 3D FEM model due to the tremendous computational cost and the difficulties in applying the perturbation forces to obtain such complicated wrinkling patterns. Thus, the proposed Fourier-based sandwich plate model provides a very attractive and efficient tool to investigate the periodic instability phenomena with extremely large wavenumbers. Note that similar wavy patterns have been obtained by the same Fourier approach Xu and Potier-Ferry (2016) for film/substrate systems, but with a different starting model (shell/volume) consuming more computational resources compared to the present 2D macroscopic model.

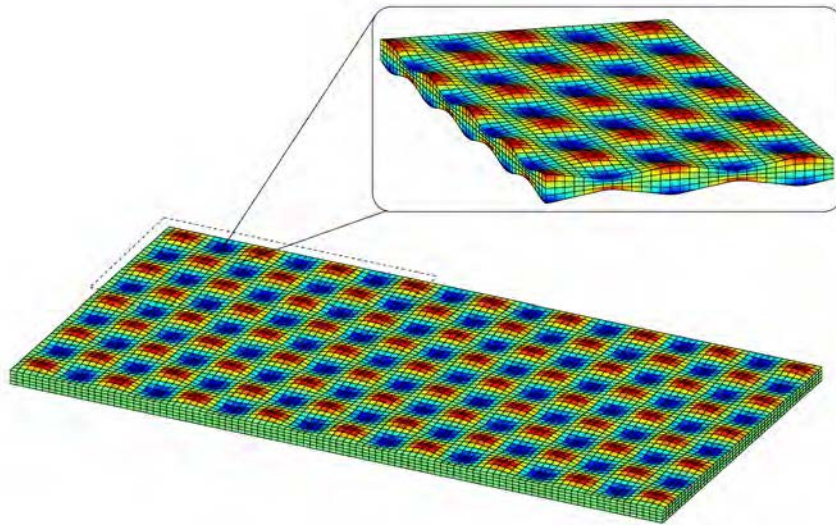


Figure 5.14: The symmetrical checkerboard wrinkling pattern for the sandwich plate of Table 5.5 under equi-biaxial compressive load by the 2D macroscopic model. One quarter of the plate near the upper left boundary is zoomed.

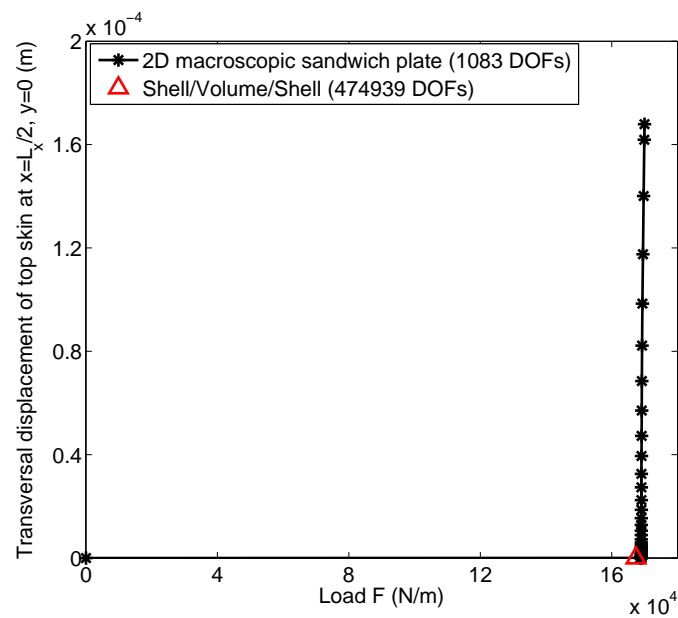


Figure 5.15: The bifurcation path for the symmetrical checkerboard wrinkling pattern of the sandwich plate under equi-biaxial compressive load.

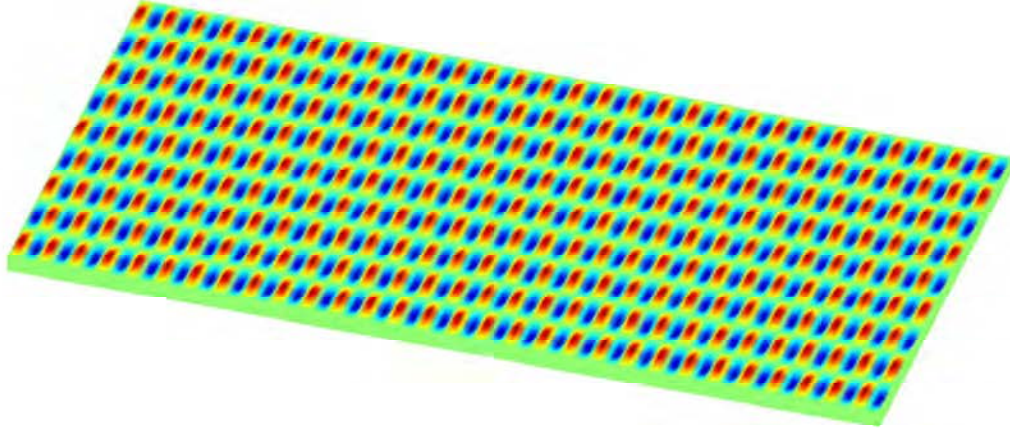


Figure 5.16: The symmetrical checkerboard wrinkling pattern for the sandwich plate of Table 5.5 under equi-biaxial compressive load with vast wavenumbers by the 2D macroscopic model.

5.6 Conclusion

In this Chapter, a Fourier-related double-scale analysis for the instability phenomena of sandwich plates was performed. Based on the 2D sandwich model proposed by Yu et al. (2015), in which the classical plate theory is used in the skins and high-order kinematics in the core, an effective 2D sandwich plate finite element model has been developed by using the technique of slowly variable Fourier coefficients. Compared to the former model, it reduces dramatically the number of degrees of freedom, thus saving significant computational cost, and makes nonlinear solution path controllable, especially when dealing with the wrinkling instability phenomena with vast wavenumbers. Antisymmetrical and symmetrical wrinkling in sandwich plates exposed to uni-axial and equi-biaxial compressive loads with four edges simply supported have been investigated. The results have been verified by the 3D FEM solution as well as the 2D microscopic results of Yu et al. (2015), which demonstrates that the proposed Fourier-related sandwich plate could accurately and fast predict the critical load and describe the post-bifurcation response for the considered instability phenomena.

The proposed model can be improved from the following aspects. One of the promising direction is to adopt the microscopic model on the boundaries and couple the proposed Fourier-based model and the microscopic model by the Arlequin

method (Ben Dhia (1998, 2006)). This will improve the accuracy of the proposed model (especially for more complicated boundary conditions) without significantly enhancing the computation cost, see Hu et al. (2011); Yu et al. (2013); Hu et al. (2010). In addition, though we need to prescribe the wavenumber as an input, we could introduce several Fourier harmonics to develop a multi-harmonic model that is able to capture the most suitable buckling mode, which has been validated in our recent work (Huang et al. (2017b)). Finally, we propose to extend our model by taking account the mean field of the transversal displacement to model the coupled global and local buckling of sandwich plates, similar to the work of Liu et al. (2012) for modeling the coupled instability in sandwich beams.

Conclusion and future perspectives

In this thesis, the instability phenomena in three common engineering structures, i.e., membrane, film/substrate and sandwich structures are investigated, in which several kinds of accurate yet efficient multi-scale models are developed by using the Technique of Slowly Variable Fourier Coefficients (TSVFC). The established non-linear systems are mainly solved by the Asymptotic Numerical Method (ANM) that is an efficient and robust path following technique in the presence of bifurcations. So far, some specific results are achieved as follows:

- Based on the Von Karman thin plate equations, the two-dimensional double-scale macroscopic model for the membrane structure has been constructed in Chapter 2 by expanding the displacement of the Von Karman equations into Fourier series and taking the Fourier coefficients as the new unknowns of the macroscopic model. Due to the property of the slow variation of the new unknowns, the needed spatial meshes can be very coarse and are not related with the wrinkling length. The established model has also been implemented into the commercial package ABAQUS as user element, which believes to lay a foundation for the future study of the instability phenomena in complex membrane structures. Numerical examples have been performed to demonstrate that the macroscopic model is able to accurately and quickly describe the details of membrane wrinkling, even if the number of the wrinkling is small. By especially analyzing the classical problem of a rectangular membrane under uniaxial load, we found that 1) the membrane instability is very sensitive to boundary conditions, for instance, the difference in the critical values due to uniaxial tensile stress and uniaxial displacement stretch is as much as 6 times; 2) there exists a dimensionless parameter that is almost constant at the presence of the wrinkles independent of the boundary condition, the loading case and the geometry size and shape of the membrane, of which the establishment has important guiding significance for rational design of membrane structure, rapid prediction and effective prevention of membrane instability.
- The two-dimensional Fourier double-scale macroscopic model has been developed in Chapter 3, which has been proved having high computational effi-

ciency and good numerical stability by studying the instability of a stiff film bounded to a soft substrate system that is under uniaxial compressive stress. By virtue of the deformation property of the film/substrate (see Yang et al. (2015)), we further combine the Carrera's Unified Formulation (CUF) with the TSVFC to deduce a one-dimensional Fourier double-scale macroscopic model in Chapter 4. This numerical model demonstrates impressive computational efficiency under the condition of ensuring accuracy, which makes it an admirable tool for large-scale instability problems such as in Mei et al. (2010).

- In the framework of the TSVFC, different Fourier coefficients have been used to deduce the Fourier model for film/substrate structures. It is pointed out that the in-plane displacement should be approximated by at least the zero-order and first-order Fourier coefficients, otherwise the oscillation locking phenomenon will occur. In addition, the Fourier double-scale model, which simultaneously accounts for a number of higher order Fourier coefficients, quickly predicts the minimum critical load of the structure, and the result is independent of the set wavelength. This could be an alternative option to trace the lowest critical buckling load in the framework of the TSVFC.
- Based on the high-order laminate theory, the two-dimensional Fourier double-scale macroscopic model of sandwich plate has been constructed in Chapter 5. Antisymmetric and symmetric wrinkling in sandwich plates exposed to uni-axial and equi-biaxial compressive loads with four edges simply supported have been investigated. The results demonstrate the Fourier-related sandwich model could accurately and fast predict the critical load and describe the post-bifurcation response for the instability phenomena in sandwich structures.

The present thesis leaves some topics that would be the possible research directions to address in the future:

- The Technique of Slowly Variable Fourier Coefficients is computationally efficient and stable. Subsequent work could be done to further study instabilities in the polar coordinate systems such as circular membranes, cylindrical shells, curved film/substrate structures.
- When the local boundary solution is concerned, the Fourier model, similar to all other reduced models, may lack enough accuracy near these areas due to the difficulty for accurately imposing the boundary conditions. To overcome

this shortcoming, the multi-scale model will be a remedy that could deal well with balancing the local accuracy and the global computational efficiency, in which the enriched model such as the shell element is adopted near the boundary conditions to capture the boundary effects and the macroscopic model such as the Fourier model is used in the rest to reduce computational cost, the two models are bridged by the bridging domain method (Arlequin method).

- In this thesis, the dimensionless parameter is observed from the numerical aspects. Follow-up work could be further carried out by conducting experiments of thin film to determine the existence of this dimensionless parameter.
- The occurrence of wrinkles in the film/substrate is due to the compressive stress. With the increasing of the stress, the instability morphology may evolve from sinusoidal wrinkles into period-doubling (Brau et al. (2011); Hutchinson (2013)), which would be of interest using the TSVFC to study a film/substrate system with a non-linear substrate that is responsible for the occurrence of the period-doubling phenomenon.

Bibliography

- N. Jacques, A. Elias, M. Potier-Ferry, H. Zahrouni, Buckling and wrinkling during strip conveying in processing lines, *Journal of Materials Processing Technology* 190 (2007) 33–40.
- N. Damil, M. Potier-Ferry, Influence of local wrinkling on membrane behaviour: a new approach by the technique of slowly variable Fourier coefficients, *Journal of the Mechanics and Physics of Solids* 58 (2010) 1139–1153.
- H. Hu, S. Belouettar, M. Potier-Ferry, A. Makradi, A novel finite element for global and local buckling analysis of sandwich beams, *Composite Structures* 90 (2009a) 270–278.
- Y. Liu, K. Yu, H. Hu, S. Belouettar, M. Potier-Ferry, N. Damil, A new Fourier-related double scale analysis for instability phenomena in sandwich structures, *International Journal of Solids and Structures* 49 (2012) 3077–3088.
- S. Drapier, J. C. Grandidier, M. Potier-Ferry, A structural approach of plastic microbuckling in long fibre composites: comparison with theoretical and experimental results, *International Journal of Solids and Structures* 38 (2001) 3877–3904.
- H. Mei, R. Huang, J. Y. Chung, C. M. Stafford, H. H. Yu, Buckling modes of elastic thin films on elastic substrates, *Applied Physics Letters* 90 (2007) 151902.
- C. M. Stafford, C. Harrison, K. L. Beers, A. Karim, E. J. Amis, M. R. Vanlandingham, H. C. Kim, W. Volksen, R. D. Miller, E. E. Simonyi, A buckling-based metrology for measuring the elastic moduli of polymeric thin films, *Nature Materials* 3 (2004) 545–550.
- J. Y. Chung, A. J. Nolte, C. M. Stafford, Surface wrinkling: A versatile platform for measuring thin-film properties, *Advanced Materials* 23 (2011) 349–368.
- D. H. Kim, J. A. Rogers, *Stretchable Electronics: Materials Strategies and Devices*, *Advanced Materials* 20 (2008) 4887–4892.
- N. Bowden, S. Brittain, A. G. Evans, J. W. Hutchinson, G. M. Whitesides, Spontaneous formation of ordered structures in thin films of metals supported on an elastomeric polymer, *Nature* 393 (1998) 146–149.

- Y. W. Wong, S. Pellegrino, Wrinkled membranes part I: Experiments, *Journal of Mechanics of Materials and Structures* 1 (2006a) 1–23.
- C. G. Wang, X. W. Du, H. F. Tan, X. D. He, A new computational method for wrinkling analysis of gossamer space structures, *International Journal of Solids and Structures* 46 (2009) 1516–1526.
- Y. Lecieux, R. Bouzidi, Experimental analysis on membrane wrinkling under biaxial load-Comparison with bifurcation analysis, *International Journal of Solids and Structures* 47 (2010) 2459–2475.
- V. Nayyar, K. Ravi-Chandar, R. Huang, Stretch-induced wrinkling of polyethylene thin sheets: Experiments and modeling, *International Journal of Solids and Structures* 51 (2014) 1847–1858.
- Y. W. Wong, S. Pellegrino, Wrinkled membranes part III: Numerical simulations, *Journal of Mechanics of Materials and Structures* 1 (2006b) 63–95.
- Y. Lecieux, R. Bouzidi, Numerical wrinkling prediction of thin hyperelastic structures by direct energy minimization, *Advances in Engineering Software* 50 (2012) 57–68.
- T. J. Healey, Q. Li, R. B. Cheng, Wrinkling Behavior of Highly Stretched Rectangular Elastic Films via Parametric Global Bifurcation, *Journal of Nonlinear Science* 23 (2013) 777–805.
- J. E. Wesfreid, S. Zaleski, Cellular Structures in instabilities, *Lecture Notes in Physics*, 210, Springer–Verlag, Heidelberg, 1984.
- N. Damil, M. Potier-Ferry, A generalized continuum approach to describe instability pattern formation by a multiple scale analysis, *Comptes Rendus Mecanique* 334 (2006) 674–678.
- N. Damil, M. Potier-Ferry, A generalized continuum approach to predict local buckling patterns of thin structures, *European Journal of Computational Mechanics* 17 (2008) 945–956.
- S. Forest, K. Sab, Cosserat overall modeling of heterogeneous materials, *Mechanics Research Communications* 25 (1998) 449–454.
- V. Kouznetsova, M. G. D. Geers, W. A. M. Brekelmans, Multi-scale second-order computational homogenization of multi-phase materials: a nested finite element

- solution strategy, *Computers Methods in Applied Mechanics and Engineering* 193 (2004) 5525–5550.
- A. Newell, J. Whitehead, Finite band width, finite amplitude convection, *Journal of Fluid Mechanics* 38 (1969) 279–303.
- L. Segel, Distant side walls cause slow amplitude modulation of cellular convection, *Journal of Fluid Mechanics* 38 (1969) 203–224.
- M. C. Cross, P. C. Hohenberg, Pattern formation out of equilibrium, *Reviews of Modern Physics* 65 (1993) 851–1112.
- J. C. Amazigo, B. Budiansky, G. Carrier, Asymptotic analyses of the buckling of imperfect columns on non-linear elastic foundations, *International Journal of Solids and Structures* 6 (1970) 1341–1356.
- Y. Pomeau, S. Zaleski, Wavelength selection in one-dimensional cellular structures, *Journal de Physique* 42 (1981) 515–528.
- M. Potier-Ferry, Amplitude modulation, phase modulation and localization of buckling patterns. In: J.M.T. Thompson, G.W. Hunt (Eds.), *Collapse: the Buckling of Structure in Theory and Practice*, 148-159, Cambridge University Press, Cambridge, 1983.
- N. Damil, M. Potier-Ferry, Wavelength selection in the postbuckling of a long rectangular plate, *International Journal of Solids and Structures* 22 (1986) 511–526.
- J. C. Amazigo, W. B. Fraser, Buckling under external pressure of cylindrical shells with dimple shaped initial imperfection, *International Journal of Solids and Structures* 7 (1971) 883–900.
- R. Abdelmoula, N. Damil, M. Potier-Ferry, Influence of distributed and localized imperfections on the buckling of cylindrical shells, *International Journal of Solids and Structures* 29 (1992) 1–25.
- X. Chen, J. W. Hutchinson, Herringbone buckling patterns of compressed thin films on compliant substrates, *Journal of Applied Mechanics* 71 (2004) 597–603.
- S. Wang, J. Song, D. H. Kim, Y. Huang, J. A. Rogers, Local versus global buckling of thin films on elastomeric substrates, *Applied Physics Letters* 93 (2008) 023126.
- B. Audoly, A. Boudaoud, Buckling of a stiff film bound to a compliant substrate—Part II: A global scenario for the formation of herringbone pattern, *Journal of the Mechanics and Physics of Solids* 56 (2008) 2422–2443.

- S. Sridharan, M. Zeggane, Stiffened plates and cylindrical shells under interactive buckling, *Finite Elements in Analysis and Design* 38 (2001) 155–178.
- L. Léotoing, S. Drapier, A. Vautrin, Nonlinear interaction of geometrical and material properties in sandwich beam instabilities, *International Journal of Solids and Structures* 39 (2002a) 3717–3739.
- Y. W. Wong, S. Pellegrino, Wrinkled membranes part II: Analytical models, *Journal of Mechanics of Materials and Structures* 1 (2006c) 25–59.
- N. Damil, M. Potier-Ferry, A new method to compute perturbed bifurcations: Application to the buckling of imperfect elastic structures, *International Journal of Engineering Science* 28 (1990) 943–957.
- H. Zahrouni, B. Cochelin, M. Potier-Ferry, Computing finite rotations of shells by an asymptotic-numerical method, *Computer Methods in Applied Mechanics and Engineering* 175 (1999) 71–85.
- J. M. Cadou, B. Cochelin, N. Damil, M. Potier-Ferry, ANM for stationary Navier-Stokes equations ans with Petrov-Galerkin formulation, *Int. J. Numer. Meth. Engn* 50 (2001) 825–845.
- B. Cochelin, N. Damil, M. Potier-Ferry, *Méthode asymptotique numérique*, Hermès-Lavoisier, 2007.
- K. Yu, H. Hu, H. Y. Tang, G. Giunta, M. Potier-Ferry, S. Belouettar, A novel two-dimensional finite element to study the instability phenomena of sandwich plates, *Computer Methods in Applied Mechanics and Engineering* 283 (2015) 1117–1137.
- H. Wagner, Flat sheet metal girders with very thin metal web, *Zeitschrift fur Flugtechnik Motorluftschiffahrt* 20 (1929) 200–314.
- M. Stein, J. M. Hedgepeth, Analysis of partly wrinkled membranes, Technical Representative NASA TN D-813.
- X. Liu, C. H. Jenkins, W. W. Schur, Large deflection analysis of pneumatic envelopes using a penalty parameter modified material model, *Finite Elements in Analysis and Design* 37 (2001) 233–251.
- R. Rossi, M. Lazzari, R. Vitaliani, E. Oñate, Simulation of light-weight membrane structures by wrinkling model, *International Journal for Numerical Methods in Engineering* 62 (2005) 2127–2153.

- A. Jarasjarungkiat, R. Wüchner, K. U. Bletzinger, A wrinkling model based on material modification for isotropic and orthotropic membranes, *Computer Methods in Applied Mechanics and Engineering* 197 (2008) 773–788.
- D. G. Roddeman, C. W. J. Oomens, J. D. Janssen, J. Drukker, The wrinkling of thin membranes: Part I—theory, *Journal of Applied Mechanics* 54 (1987a) 884–887.
- D. G. Roddeman, C. W. J. Oomens, J. D. Janssen, J. Drukker, The wrinkling of thin membranes: Part II—numerical analysis, *Journal of Applied Mechanics* 54 (1987b) 888–892.
- Y. Miyazaki, Wrinkle/slack model and finite element dynamics of membrane, *International Journal for Numerical Methods in Engineering* 66 (2006) 1179–1209.
- T. Akita, K. Nakashino, M. C. Natori, K. C. Park, A simple computer implementation of membrane wrinkle behaviour via a projection technique, *International Journal for Numerical Methods in Engineering* 71 (2007) 1231–1259.
- A. Shaw, D. Roy, Analyses of wrinkled and slack membranes through an error reproducing mesh-free method, *International Journal of Solids and Structures* 44 (2007) 3939–3972.
- N. A. Pimprikar, B. Banerjee, D. Roy, R. M. Vasu, S. R. Reid, New computational approaches for wrinkled and slack membranes, *International Journal of Solids and Structures* 47 (2010) 2476–2486.
- B. Banerjee, A. Shaw, D. Roy, The theory of Cosserat points applied to the analyses of wrinkled and slack membranes, *Computational Mechanics* 43 (2009) 415–429.
- F. G. Flores, E. Oñate, Wrinkling and folding analysis of elastic membranes using an enhanced rotation-free thin shell triangular element, *Finite Elements in Analysis and Design* 47 (2011) 982–990.
- N. Damil, M. Potier-Ferry, H. Hu, New nonlinear multi-scale models for wrinkled membranes, *Comptes Rendus Mecanique* 341 (2013) 616–624.
- N. Damil, M. Potier-Ferry, H. Hu, Membrane wrinkling revisited from a multi-scale point of view, *Advanced Modeling and Simulation in Engineering Sciences* 1 (2014) 6.
- N. Friedl, F. G. Rammerstorfer, F. D. Fischer, Buckling of stretched strips, *Computers & Structures* 78 (2000) 185–190.

- N. Jacques, M. Potier-Ferry, On mode localisation in tensile plate buckling, *Comptes Rendus Mecanique* 333 (2005) 804–809.
- K. Mhada, B. Braikat, H. Hu, N. Damil, M. Potier-Ferry, About macroscopic models of instability pattern formation, *International Journal of Solids and Structures* 49 (2012) 2978–2989.
- B. Cochelin, N. Damil, M. Potier-Ferry, Asymptotic-numerical methods and Padé approximants for non-linear elastic structures, *International Journal for Numerical Methods in Engineering* 37 (1994) 1187–1213.
- E. Cerda, L. Mahadevan, Geometry and Physics of Wrinkling, *Physical Review Letters* 90 (2003) 1–4.
- H. Hu, N. Damil, M. Potier-Ferry, A bridging technique to analyze the influence of boundary conditions on instability patterns, *Journal of Computational Physics* 230 (2011) 3753–3764.
- K. Yu, H. Hu, S. Y. Chen, S. Belouettar, M. Potier-Ferry, Multi-scale techniques to analyze instabilities in sandwich structures, *Composite Structures* 96 (2013) 751–762.
- H. Ben Dhia, Multiscale mechanical problems: the Arlequin method, *Comptes Rendus de l’Académie des Sciences IIb* (1998) 899–904.
- H. Ben Dhia, Global-local approaches: the Arlequin framework, *European Journal of Computational Mechanics* 15 (2006) 67–80.
- H. Hu, S. Belouettar, M. Potier-Ferry, E. M. Daya, A. Makradi, Multi-scale non-linear modelling of sandwich structures using the Arlequin method, *Composite Structures* 92 (2010) 515–522.
- Z. Y. Huang, W. Hong, Z. Suo, Nonlinear analyses of wrinkles in a film bonded to a compliant substrate, *Journal of the Mechanics and Physics of Solids* 53 (2005) 2101–2118.
- C. Harrison, C. M. Stafford, W. Zhang, A. Karim, Sinusoidal phase grating created by a tunably buckled surface, *Applied Physics Letters* 85 (2004) 4016–4018.
- J. A. Rogers, T. Someya, Y. Huang, Materials and Mechanics for Stretchable Electronics, *Science* 327 (2010) 1603–1607.

- H. G. Allen, *Analysis and Design of Structural Sandwich Panels*, Pergamon Press, Oxford, 1969.
- K. Niu, R. Talreja, Modeling of wrinkling in sandwich panels under compression, *Journal of Engineering Mechanics* 128 (1999) 875–883.
- J. Song, H. Jiang, Z. J. Liu, D. Y. Khang, Y. Huang, J. A. Rogers, C. Lu, C. G. Koh, Buckling of a stiff thin film on a compliant substrate in large deformation, *International Journal of Solids and Structures* 45 (2008) 3107–3121.
- H. Mei, C. M. Landis, R. Huang, Concomitant wrinkling and buckle-delamination of elastic thin films on compliant substrates, *Mechanics of Materials* 43 (2011) 627–642.
- F. Brau, H. Vandeparre, A. Sabbah, C. Poulard, A. Boudaoud, P. Damman, Multiple-length-scale elastic instability mimics parametric resonance of nonlinear oscillators, *Nature Physics* 7 (2011) 56–60.
- J. W. Hutchinson, The role of nonlinear substrate elasticity in the wrinkling of thin films, *Philosophical Transactions of the Royal Society of London A: Mathematical, Physical and Engineering Sciences* 371 (2013) 20120422.
- M. Shariyat, K. Asemi, 3D energy-based finite element elasticity approach for shear postbuckling analysis of functionally graded plates on elastic foundations, *Composite Structures* 152 (2016) 579–591.
- J. N. Reddy, A simple higher-order theory of laminated composite plate, *Journal of Applied Mechanics* 51 (1984) 745–752.
- P. Vidal, O. Polit, A family of sinus finite elements for the analysis of rectangular laminated beams, *Composite Structures* 84 (2008) 56–72.
- A. J. M. Ferreira, E. Carrera, M. Cinefra, E. Viola, F. Tornabene, N. Fantuzzi, A. M. Zenkour, Analysis of thick isotropic and cross-ply laminated plates by Generalized Differential Quadrature Method and a unified formulation, *Composites Part B: Engineering* 58 (2014) 544–552.
- F. Tornabene, N. Fantuzzi, E. Viola, A. J. M. Ferreira, Radial basis function method applied to doubly-curved laminated composite shells and panels with a general higher-order equivalent single layer theory, *Composites Part B: Engineering* 55 (2013) 642–659.

- F. Tornabene, N. Fantuzzi, M. Baccocchi, Higher-order structural theories for the static analysis of doubly-curved laminated composite panels reinforced by curvilinear fibers, *Thin-Walled Structures* 102 (2016) 222–245.
- J. Yang, Q. Huang, H. Hu, G. Giunta, S. Belouettar, M. Potier-Ferry, A new family of finite elements for wrinkling analysis of thin films on compliant substrates, *Composite Structures* 119 (2015) 568–577.
- E. Carrera, Theories and finite elements for multilayered, anisotropic, composite plates and shells: a unified compact formulation with numerical assessment and benchmarking, *Archives of Computational Methods in Engineering* 10 (2003a) 216–296.
- Q. Z. He, H. Hu, S. Belouettar, G. Giunta, K. Yu, Y. Liu, F. Biscani, E. Carrera, M. Potier-Ferry, Multi-scale modelling of sandwich structures using hierarchical kinematics, *Composite Structures* 93 (2011) 2375–2383.
- M. Cinefra, E. Carrera, L. D. Croce, C. Chinosi, Refined shell elements for the analysis of functionally graded structures, *Composite Structures* 94 (2012) 415–422.
- K. Mhada, B. Braikat, N. Damil, A 2D Fourier double scale analysis of global-local instability interaction in sandwich structures, in: *Proceedings of 21ème Congrès Français de Mécanique*, Bordeaux, France, 2013.
- Q. Huang, H. Hu, K. Yu, M. Potier-Ferry, S. Belouettar, N. Damil, Macroscopic simulation of membrane wrinkling for various loading cases, *International Journal of Solids and Structures* 64-65 (2015) 246–258.
- K. Attipou, H. Hu, F. Mohri, M. Potier-Ferry, S. Belouettar, Thermal wrinkling of thin membranes using a Fourier-related double scale approach, *Thin-Walled Structures* 94 (2015) 532–544.
- K.-J. Bathe, *Finite element procedures*, Prentice Hall, New Jersey, USA, 2006.
- M. A. Crisfield, *Non-Linear Finite Element Analysis of Solids and Structures*, John Wiley & Sons, 1996.
- Y. P. Cao, F. Jia, Y. Zhao, X. Q. Feng, S. W. Yu, Buckling and post-buckling of a stiff film resting on an elastic graded substrate, *International Journal of Solids and Structures* 49 (2012) 1656–1664.

- J. N. Reddy, *An Introduction to Nonlinear Finite Element Analysis*, Oxford, UK, 2004a.
- E. Carrera, S. Brischetto, Analysis of thickness locking in classical, refined and mixed multilayered plate theories, *Composite Structures* 82 (2008a) 549–562.
- E. Carrera, S. Brischetto, Analysis of thickness locking in classical, refined and mixed theories for layered shells, *Composite Structures* 85 (2008b) 83–90.
- H. Ben Dhia, G. Rateau, The Arlequin method as a flexible engineering design tool, *International Journal for Numerical Methods in Engineering* 62 (2005) 1442–1462.
- H. Hu, S. Belouettar, M. Potier-Ferry, E. M. Daya, Multi-scale modeling of sandwich structure using the Arlequin method, Part I: linear modelling, *Finite Element in Analysis and Design* 45 (2009b) 37–51.
- B. Li, Y. P. Cao, X. Q. Feng, H. Gao, Surface wrinkling of mucosa induced by volumetric growth: Theory, simulation and experiment, *Journal of the Mechanics and Physics of Solids* 59 (2011) 758–774.
- B. Li, Y. P. Cao, X. Q. Feng, H. Gao, Mechanics of morphological instabilities and surface wrinkling in soft materials: a review, *Journal of the Mechanics and Physics of Solids* 8 (2012) 5728.
- Z. Y. Huang, W. Hong, Z. Suo, Evolution of wrinkles in hard films on soft substrates, *Physical Review E* 70 (2004) 030601(R).
- H. Q. Jiang, D. Y. Khang, H. Y. Fei, H. Kim, Y. G. Huang, J. L. Xiao, J. A. Rogers, Finite width effect of thin-films buckling on compliant substrate: Experimental and theoretical studies, *Journal of the Mechanics and Physics of Solids* 56 (2008) 2585–2598.
- O. Polit, M. Touratier, High-order triangular sandwich plate finite element for linear and non-linear analyses, *Computer Methods in Applied Mechanics and Engineering* 185 (2000) 305–324.
- A. J. M. Ferreira, C. M. C. Roque, E. Carrera, M. Cinefra, O. Polit, Radial basis functions collocation and a unified formulation for bending, vibration and buckling analysis of laminated plates, according to a variation of Murakami's zig-zag theory, *European Journal of Mechanics-A/Solids* 30 (2011) 559–570.

- H. S. Shen, *A Two-Step Perturbation Method in Nonlinear Analysis of Beams, Plates and Shells*, John Wiley & Sons Inc., Singapore, 2013.
- Q. Huang, R. Xu, Y. Liu, H. Hu, G. Giunta, S. Belouettar, M. Potier-Ferry, A two-dimensional Fourier-series finite element for wrinkling analysis of thin films on compliant substrates, *Thin-Walled Structures* 114 (2017a) 144–153.
- M. A. Aiello, L. Ombres, Local buckling loads of sandwich panels made with laminated faces, *Composite Structures* 38 (1997) 191–201.
- W. Ji, A. M. Waas, Global and local buckling of a sandwich beam, *Journal of Engineering Mechanics* 133 (2007) 230–237.
- W. Ji, A. M. Waas, 2D elastic analysis of the sandwich panel buckling problem: benchmark solutions and accurate finite element formulations, *Zeitschrift für Angewandte Mathematik und Physik* 61 (2010) 897–917.
- M. Douverelle, P. Le Grogneq, Exact analytical solutions for the local and global buckling of sandwich beam-columns under various loadings, *International Journal of Solids and Structures* 50 (2013) 2597–2609.
- K. Sad Saoud, P. Le Grogneq, A unified formulation for the biaxial local and global buckling analysis of sandwich panels, *Thin-Walled Structures* 82 (2014) 13–23.
- A. K. Noor, W. S. Burton, C. W. Bert, *Computational Models for Sandwich Panels and Shells*, *Applied Mechanics Reviews* 49 (1996) 155–199.
- J. N. Reddy, *Mechanics of Laminated Plates and Composite Shells: Theory and Analysis*, 2nd ed., CRC, New York, 2004b.
- D. J. Dawe, W. X. Yuan, Overall and local buckling of sandwich plates with laminated faceplates, Part I: Analysis, *Computer Methods in Applied Mechanics and Engineering* 190 (2001) 5197–5213.
- W. X. Yuan, D. J. Dawe, Overall and local buckling of sandwich plates with laminated faceplates, part II: Applications, *Computer Methods in Applied Mechanics and Engineering* 190 (2001) 5215–5231.
- L. Léotoing, S. Drapier, A. Vautrin, First applications of a novel unified model for global and local buckling of sandwich columns, *European Journal of Mechanics-A/Solids* 21 (2002b) 683–701.

- E. Madenci, I. Guven, *The finite element method and applications in engineering using ANSYS®*, chap. 11, Springer, USA, 654, 2006.
- I. Kreja, R. Schmidt, J. N. Reddy, Finite elements based on a first-order shear deformation moderate rotation shell theory with applications to the analysis of composite structures, *International Journal of Non-Linear Mechanics* 32 (1997) 1123–1142.
- L. W. Zhang, K. M. Liew, J. N. Reddy, Postbuckling of carbon nanotube reinforced functionally graded plates with edges elastically restrained against translation and rotation under axial compression, *Computer Methods in Applied Mechanics and Engineering* 298 (2016a) 1–28.
- L. W. Zhang, K. M. Liew, J. N. Reddy, Postbuckling analysis of bi-axially compressed laminated nanocomposite plates using the first-order shear deformation theory, *Composite Structures* 152 (2016b) 418–431.
- A. J. M. Ferreira, Analysis of composite plates using a layerwise theory and multiquadrics discretization, *Mechanics of Advanced Materials and Structures* 12 (2005) 99–112.
- M. Touratier, An efficient standard plate theory, *International Journal of Engineering Science* 29 (1991) 901–916.
- P. Vidal, O. Polit, Assessment of the refined sinus model for the non-linear analysis of composite beams, *Composite Structures* 87 (2009) 370–381.
- M. Karama, K. S. Afaq, S. Mistou, Mechanical behaviour of laminated composite beam by the new multi-layered laminated composite structures model with transverse shear stress continuity, *International Journal of Solids and Structures* 40 (2003) 1525–1546.
- M. D’Ottavio, O. Polit, Linearized global and local buckling analysis of sandwich struts with a refined quasi-3D model, *Acta Mechanica* 226 (2015) 81–101.
- E. Carrera, Historical review of Zig-Zag theories for multilayered plates and shells, *Applied Mechanics Reviews* 56 (2003b) 287–308.
- E. Carrera, F. Miglioretti, Selection of appropriate multilayered plate theories by using a genetic like algorithm, *Composite Structures* 94 (2012) 1175–1186.

- M. D'Ottavio, O. Polit, W. Ji, A. M. Waas, Benchmark solutions and assessment of variable kinematics models for global and local buckling of sandwich struts, *Composite Structures* 156 (2016) 125–134.
- H. Hu, S. Belouettar, M. Potier-Ferry, E. M. Daya, Review and assessment of various theories for modelling sandwich composites, *Composite Structures* 84 (2008) 282–292.
- Y. P. Liu, C. G. Wang, H. F. Tan, M. K. Wadee, The interactive bending wrinkling behaviour of inflated beams, *Proceedings of the Royal Society of London A: Mathematical, Physical and Engineering Sciences* 472 (2016) 20160504.
- Q. Huang, J. Yang, W. Huang, Y. Liu, H. Hu, G. Giunta, S. Belouettar, A new Fourier-related double scale analysis for wrinkling analysis of thin films on compliant substrates, *Composite Structures* 160 (2017b) 613–624.
- O. C. Zienkiewicz, Y. K. Cheung, The finite element method for analysis of elastic isotropic and orthotropic slabs, *Proceedings of the Institution of Civil Engineers* 28 (1964) 471–488.
- R. J. Melosh, Basis of derivation of matrices for the direct stiffness method, *AIAA Journal* 1 (1963) 1631–1637.
- L. Léotoing, S. Drapier, A. Vautrin, Using new closed-form solutions to set up design rules and numerical investigations for global and local buckling of sandwich beams, *Journal of Sandwich Structures and Materials* 6 (2004) 263–289.
- F. Xu, M. Potier-Ferry, A multi-scale modeling framework for instabilities of film/substrate systems, *Journal of the Mechanics and Physics of Solids* 86 (2016) 150–172.
- Y. Mei, S. Kiravittaya, S. Harazim, O. G. Schmidt, Principles and applications of micro and nanoscale wrinkles, *Materials Science and Engineering R* 70 (2010) 209–224.